Structural and Optoelectronic Properties, Phase Transitions, and Degradation of Semiconducting CsPbI₃-Perovskite Thin-Films for Photovoltaics

by **Pascal Becker**

A theses in partial fulfillment
of the requirements for the
degree of doctor in the
faculty of mathematics and natural science

submitted to the

Department of Physics

of the

Bergische Universtität Wuppertal

Wuppertal, 2019

Contents

Contents

List of Abbreviations

BCP	bathocuproine
C$_{60}$	fullerene C$_{60}$
CCD	charge-coupled device
EQE	external quantum efficiency
FF	fill factor
FFT	fast Fourier transformation
IR	infrared
ITO	indium tin oxide
J$_{SC}$	short circuit current density
JV	current-density–voltage
OPTP	optical-pump THz-probe
PCE	power conversion efficiency
PL	photoluminescence
PTAA	poly(triarylamine)
SEM	scanning electron microscopy
TRPL	time-resolved photoluminescence
T$_{sub}$	substrate temperature during evaporation
UV-Vis	ultraviolet visible spectroscopy
V$_{OC}$	open circuit voltage
WLR	white light optical reflection
XRD	X-ray diffraction
XRF	X-ray fluorescence spectroscopy

1

Introduction

The worlds consumption of electrical energy is still increasing, while at the same time affords are made to reduce the emission of CO_2.[1] These reductions are inevitable to mitigate global warming and maintain a stable climate on earth.[2] For this, power generation from renewable energy sources serves as a suitable replacement for fossil fuels. Aside from hydropower, wind and geothermal energy, solar power conversion with solar cells plays an important role. While the majority of the currently installed generation capacity is based on silicon,[3] new technologies are being developed to reduce material input, weight and the energy used for the production. These goals are achieved by thin-film solar cells, which in addition increase the flexibility in application since they can be produced on different substrates including flexible foils.[4]

A variety of materials was discovered for application in thin-film photovoltaics including cadmium tellurite (CdTe),[5, 6] copper indium gallium sulfide (CIGS),[4, 7] copper zinc tin sulfide (CZTS)[8, 9] and dye-sensitized TiO_2-based solar cells.[10, 11] While these materials tackle different disadvantages of the common silicon cells, they yet cannot compete in terms of power conversion efficiency (PCE). In 2009 lead halide perovskite materials were found as a promising new class of absorber materials for application in thin-film solar cells.[12]

The term perovskite originally referred to the mineral calcium titanate, which was found in 1839 and named after the Russian mineralogist Lew Alexejewitsch Perowski.[13] Much later, in 1926, Victor Goldschmidt discovered the crystallographic structure of this material, naming it the perovskite structure.[14] It was found, that many other minerals exhibit the perovskite structure as well. All perovskite materials can be described by the general chemical formula of ABX_3, with A and B being different cations and X being an anion.[15]

On the search for improved dye materials for application in dye-sensitized solar cells, the mixed organic-inorganic perovskite materials $CH_3NH_3PbBr_3$ and $CH_3NH_3PbI_3$ were employed in a solar for the first time.[12] While these cells achieved PCEs of above 3 %, they were still fabricated in the typical architecture of dye-sensitized solar cells, employing a mesoporous scaffold of TiO_2 and a liquid electrolyte. Unfortunately, this electrolyte caused a degradation of the perovskite material, leading to very poor device stabilities of only several minutes. Two years later, the PCE could be improved to above 6 % by slight modifications of the fabrication procedure, while the cells were still suffering from rapid degradation.[16] Half a year later, two groups independently demonstrated, that the electrolyte is not necessary for the fabrication of perovskite based solar cells, achieving PCEs of above 9 % and significantly improved stability.[17, 18]

Over the past years, the record PCE could be improved to currently 23.7 %,[19] surpassing most of the established thin-film technologies. On the way of the improvement, many parameters of the perovskite fabrication were investigated. The material was prepared by various techniques, resulting in powders, quantum dots and thin-films. These techniques include solid solutions, ball milling,[20, 21] solution processing in numerous variations[22–27] and different evaporation techniques[28–32]. While the architecture of the first cell was defined by its decent from dye-sensitized cells, thus employing the mesoporous TiO_2 scaffold, later cells employed compact, flat contact layers.[32] New materials for the contact layers were studied, resulting in various combinations in both, p-i-n and n-i-p structures.[33–36] Even cells with only one selective contact layer were demonstrated to work.[37–39] Another important factor for the improvement of the cells is the chemical composition of the perovskite absorber material. The first cells used the organic molecule methylamonium (MA, CH_3NH_3) as A-cation. However, different other organic molecules like formamidinium (FA, $HC(NH_2)_2$)[40, 41] and guanidinium (GUA, $HNC(NH_2)_2$),[42, 43] as well as inorganic atoms like cesium[44–46] and rubidium[47, 48] can be and were used later. For the B-cation not only lead, but tin and bismuth can be used as well,[45, 49, 50] while the C-anion is usually chosen to be the halides iodide, bromide or chloride.[39, 51, 52] These possibilities result in various combinations and mixtures of constituents, opening an enormous field of parameters. Recent high performance cells employ such mixtures, leading to complicated systems of triple or quadruple A-cations, mixed B-cations and mixed halides.[47, 53–55]

These mixtures not only improve the PCE but also the stability of the cells against moisture, oxygen and UV-light.[56–58] However, the significant amount of organic material in most of the perovskite based solar cells still limits the thermal stability, leading to a degradation of the cells at elevated temperatures.[53, 59] To overcome this impediment, fully inorganic perovskite solar cells were investigated. The first cells employed $CsSnI_3$,[45,

60] as photoabsorber, for which the chemical stability is limited by the thermodynamically unfavored oxidation state of Sn^{2+} compared to Sn^{4+}.[61] The substitution of tin by lead, resulting in $CsPbI_3$, overcomes this limitation.[44]

Although this material was discovered as early as 1893 [62] and crystallographically characterized in 1950, [63] its photovoltaic potential was only discovered recently.[44] With its large band of $1.75\,eV$ it is especially suitable for tandem applications with low band gap bottom cells such as silicon or kesterite.[64–68] However, one of the major drawbacks of this material is, that in the bulk material at room temperature, the non-perovskite orthorhombic δ-phase is favored over the (distorted) perovskite α, β, and γ-phases.[69, 70] Details about these phases will be discussed in Section 2.1. Various efforts were made to stabilize the perovskite structures at room temperature. These include introduction of hydroiodic acid (HI), small amounts of water, PEA and EDA.[44, 71–74] Also chemical alteration of the material by partial substitution of lead with bismuth or iodide by bromide were made.[75–77] While these efforts lead to decent PCEs of above $17\,\%$ the fundamental properties of the material are poorly studied.[78]

This work contributes to an improved understanding of the pure $CsPbI_3$ material as a base for the aforementioned modifications, by giving an overview over the optoelectronic as well as morphological and structural properties. To universalize these findings the investigations were performed on samples with a lateral gradient in $[CsI]/[PbI_2]$ ratio. Despite the comparably small field of parameters, the compositional dependent investigation of the materials properties requires high-throughput techniques. Owing to the lateral gradient, these techniques can be realized by spatially resolved measurements. For the far more complicated mixed perovskites, these high throughput techniques become inevitable to be able to screen the various combinations of constituents. The methods developed and described in this work can therefore be seen as pathbreaking for further investigations on different materials.

For the fabrication of such samples a dedicated vacuum evaporation system was designed, installed and taken in operation. This setup additionally allows in-situ studies of the formation of the films. The chemical composition, crystallographic structure and morphology of the as-deposited films were investigated dependent on the composition as well as on the substrate temperature during evaporation (T_{sub}). In addition, the optoelectronic properties of these films were investigated, yielding the band gap, charge carrier recombination kinetics and dynamics, and photoluminescence quantum yield. Solar cells were fabricated, employing the evaporated $CsPbI_3$ thin-films as photoabsorber and yielding power conversion efficiencies of $12\,\%$.

For a comparison with films reported in the literature, the as-deposited films were subjected to a high temperature annealing step, which led to a series of phase transitions. The kinetics of these phase transitions were studied and the annealed films were characterized as described above to allow a comparison of the properties of the as-deposited and the annealed films.

Finally, the degradation of the films was investigated with a focus to the nature and origins of the degradation process. Therefore, the crystal structure was monitored in-situ by continuous X-ray diffraction measurements. In addition a series of degradation experiments in different atmospheric conditions was conducted and monitored by spatially resolved monitoring of the optical reflection.

The results of the measurements mentioned above were combined to contribute to an improved understanding of the material. For the first time, the influence of the composition on the formation of the different crystallographic phases is investigated. These insights allow to formulate conditions for the formation of secondary phases. The resulting model underlines the importance of the grain size on the thermodynamic stability of the perovskite phase, as described in recent literature.[71, 79]

The phase transition temperature to the perovskite phase is determined precisely and with respect to the chemical composition as well as T_{sub}. Differences in the optoelectronic properties of the annealed films in comparison to the as-deposited films are related to the structural and morphological changes.

The results from the degradation experiments are correlated to formulate a model of the degradation process. Causes for the degradation are found and related to the morphology and crystal structure of the samples. The role of composition, grain size and T_{sub} on the stability is described.

These models collaborate to give an arching overview about the formation, the properties, the phase transitions and the degradation of $CsPbI_3$ thin-films from co-evaporation.

2

Material Background, Sample Preparation and Characterization Techniques

In this section general information is given about the material system, which is reported in this work, as well as the sample preparation and the characterization techniques. It aims to give the necessary background on these techniques, which is required for the understanding of the results presented in this work, and is not meant as an exhaustive treatment of these topics.

2.1 Fully Inorganic CsPbI$_3$-Perovskite

In this work CsPbI$_3$-perovskites are investigated, which employ cesium and lead as anions and iodide as the cation, thus forming a fully inorganic perovskite material, which has the advantage of improved thermal stability as compared to mixed organic-inorganic perovskites. [44, 64, 80]

Crystal Structures

Despite the different terminologies in literature,[72, 81] one of the most recent reports clarifies the temperature dependent crystal structure of CsPbI$_3$ by in-situ XRD measurements during annealing of powder samples.[69] The following remarks are based on this report, which presents four known crystal structures of CsPbI$_3$ depending on the temperature as a cubic perovskite structure, a tetragonal distorted perovskite structure, an orthorhombic distorted perovskite structure and a non-perovskite orthorhombic structure.

The cubic structure is referred to as α-phase. It has a black appearance and was shown to be only stable above $260\,°C$ in the powder sample. Figure 2-1(a) and (b) show the crystal structure of the black α-phase. The typical perovskite structure is clearly visible, consisting of octahedra with iodine on its corners and a lead atom in its center. The octahedra are organized in a cubic lattice and share each corner with another octahedron.

(a)

(b)

(c)

(d)
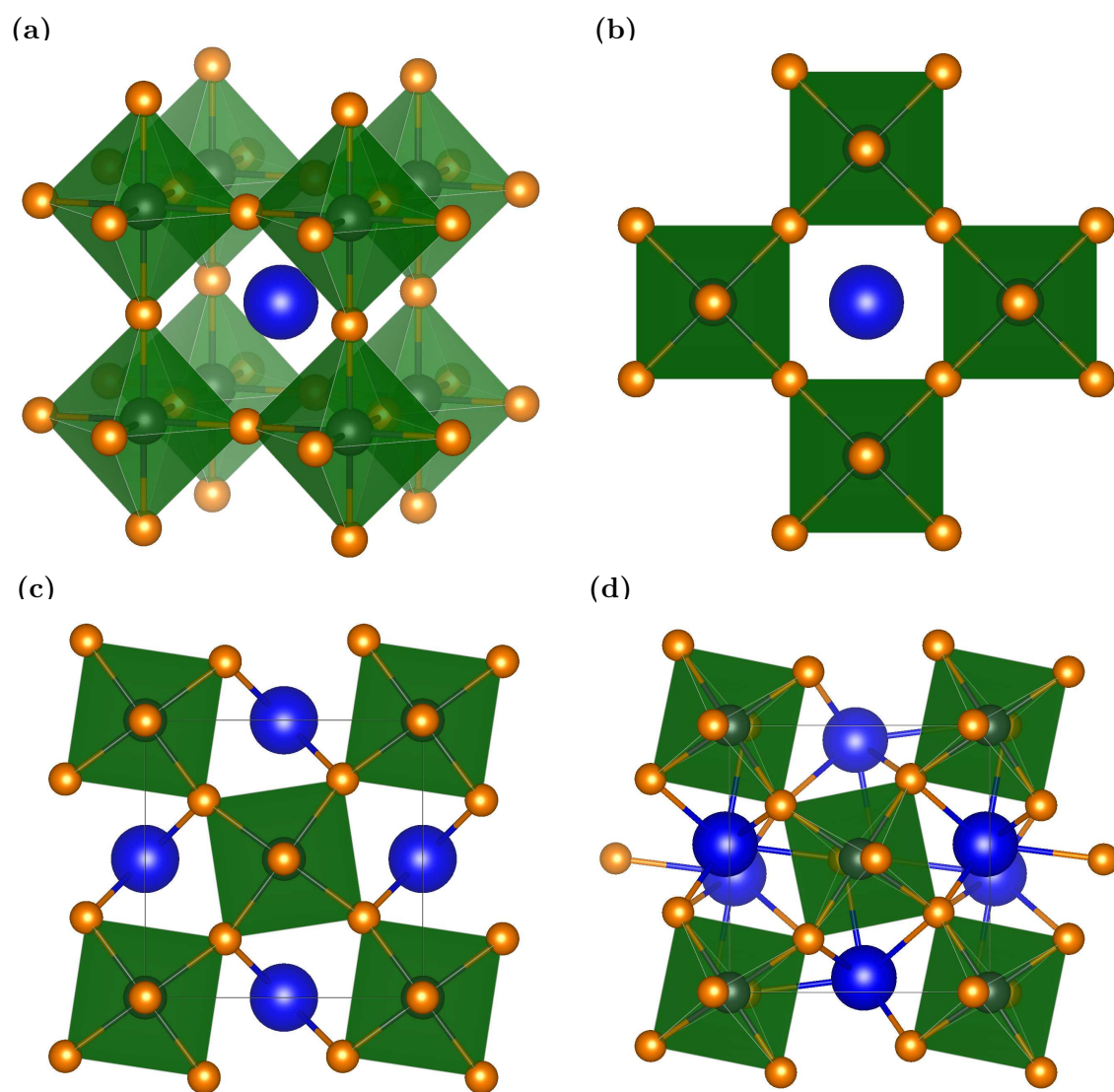
Figure 2-1: Crystal structures of the perovskite and distorted perovskite phases of CsPbI₃. (a) 3D-view of the unit cell of the α-phase with the typical octahedra with iodine (orange) on the corners, lead (black) in the center of each octahedron and cesium (blue) in between the octahedra. (b), (c) and (d) show the top view of the α, β and γ-phase unit cells, respectively. While the octahedra are well aligned in the α-phase, they are rotated within the plane in the β-phase, and in and against the plane in the γ-phase.

One cesium cation is located in each gap between the octahedra. This cubic black α-phase represents the CsPbI$_3$ structure with the highest symmetry.

Descending in symmetry, the next phase is the tetragonal β-phase, which exhibits a black color as well and is only stable above 175 °C. Figure 2-1(c) shows the crystal structure of this phase. The structure is referred to as distorted perovskite. Iodine and lead form corner sharing octahedra with cesium in between them, as already seen in the cubic structure. However, the octahedra are tilted in the plane, thus lowering the symmetry.

Below 175 °C the metastable γ-phase forms, which exhibits an orthorhombic phase as shown in Figure 2-1(d). It shows the same octahedra as the α and β-phase, which are not only tilted in plane but also against the plane, thus introducing an additional distortion of the perovskite structure. It features a dark brown color which is described as black in parts of the literature. To prevent confusion, this phase will be referred to as the brown γ-phase in this work, in contrast to the black α-phase, although they show a similar appearance.

The fourth phase is the orthorhombic δ-phase. Its crystal structure is shown in Figure 2-2(a). The δ-phase exhibits a yellow color and is a non-perovskite structure. Although it features the same octahedra as the other three phases, the octahedra are not organized corner sharing and in planes but edge sharing in double chains. Upon annealing above 310 °C the yellow δ-phase can be transformed into the black α-phase without intermediate steps, which, upon cooling, transforms into the β and, subsequently, the brown γ-phase.[69]

(a)

(b)
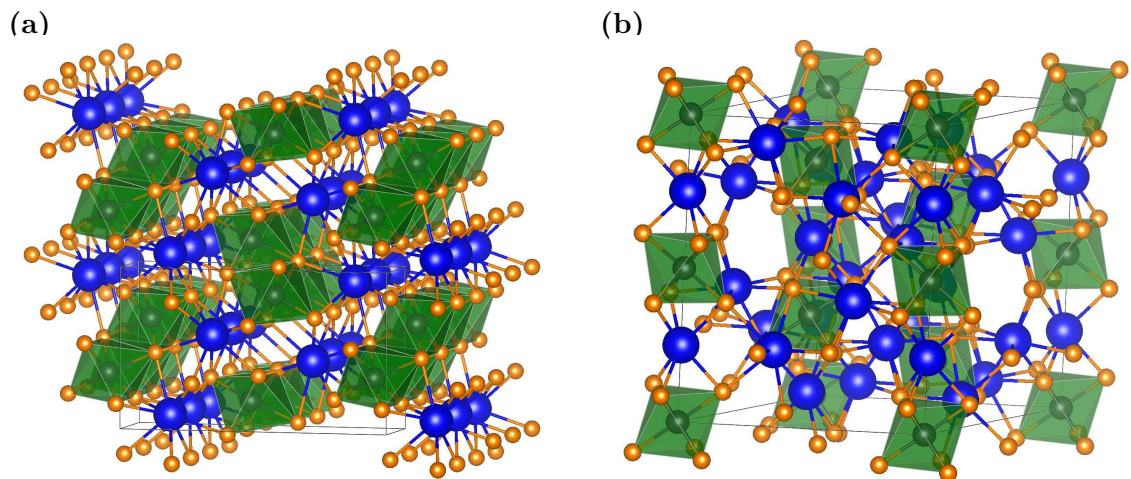
Figure 2-2: *Crystal structures of (a) the yellow δ-CsPbI$_3$ phase (multiple unit cells) and (b) the very CsI-rich Cs$_4$PbI$_6$ phase. In the δ-CsPbI$_3$ phase, the octahedra with iodine (orange) on the corners and lead (black) in the center are connected in double chains, which are separated by cesium (blue). In the CsI-rich Cs$_4$PbI$_6$-phase, the octahedra are entirely disconnected and incorporated in the hexagonal structure.*

Although both, γ and δ-phase, are orthorhombic structures, they have vastly different lattice constants. To avoid confusion, in this work the phases are referred to as brown γ-phase and yellow δ-phase, respectively. Although the yellow phase is often referred to as the only stable phase of CsPbI$_3$ at room temperature,[44, 75, 82] it was demonstrated, that a metastable perovskite structure can sustain at room temperature over the course of weeks and months.[69, 71, 83] Despite numerous discussions and false phase identification in literature, recent reports have clarified, that this metastable phase is the brown γ-phase and not the black α-phase. Section 3.3 contributes to this clarification.

Calculations reveal, that the reason for this metastable behavior is based on the different surface and bulk free energies of the brown γ-phase and the yellow δ-phase.[71] While the γ-phase exhibits a lower surface free energy, the δ-phase has a lower bulk free energy. Thus, the thermodynamically stable phase is determined by the ratio of surface and bulk of the crystallites. According to these calculations, the brown γ-phase is thermodynamically favored for particles with grain sizes below 100 nm. Different reports in literature experimentally confirmed this trend of increasing stability with decreasing grain size.[64, 69, 74] In Section 3.3 and Section 3.4 this matter will be discussed for the evaporated films reported in this work.

In addition to the cesium lead iodide in a 1-1-3 stoichiometry, other compositions of this material exist in a more cesium or lead-rich composition.[84, 85] In this work the very cesium iodide rich composition of Cs$_4$PbI$_6$ will play a role, which is organized in a hexagonal structure [85] and depicted in Figure 2-2(b). Like in the aforementioned structures of CsPbI$_3$, lead and iodide form octahedra, which, however, are entirely disconnected in this material.

In XRD measurements on very off-stoichiometric samples reported in this work (see Section 3.3), segregations of the binary compounds of CsI and PbI$_2$ are detected. While CsI forms a cubic $P\,4/m\,\bar{3}\,2/m$ structure,[86] structures with different space groups can be found for PbI$_2$ in the literature.[87–89] It was found, that the data presented in this work, were best described by the tetragonal $P\,3\,m\,1$ structure.[89]

Optical Properties

For the application as photoabsorber in a solar cell, the optical properties and especially the band gap, of the material are of utter most importance. The optical bang dap of the materials mentioned above were extracted from literature and are reported in Table 2-1. Considering the ternary compositions of the material, only the perovskite phases reveal an adequate band gap for application as an absorber for solar cell application. While the band gap of the δ-phase is still on the high energy border of the visible spectrum, the band

Table 2-1: *Optical band gap as obtained from literature for different semiconducting materials, which are reported in this work. From the three ternary phases, the γ-CsPbI₃ is the only material with a suitable band gap for application as a photoabsorber in solar cells. The two binary phases are the salts, which are co-evaporated for the fabrication of the samples described in this work. Poly(triarylamine) (PTAA) is used as a window-layer for the fabrication of solar cells.*

material	band gap / eV	band gap / nm
γ-CsPbI$_3$[90]	1.74	711
δ-CsPbI$_3$[49]	2.86	433
Cs$_4$PbI$_6$[91]	3.4	364
CsI[92]	5.4	229
PbI$_2$[93]	2.5	495
PTAA [94]	3.1	400

gap of the very CsI-rich phase of Cs$_4$PbI$_6$ is even higher and in the UV-region. These band gaps are in agreement with the optical appearance of the phases as stated above.

For considerations in the evaluation of the optical measurements reported in this work, the band gaps of the binary phases are given as well. The band gap of CsI is far in the UV-region, thus appearing transparent to the eye, while PbI$_2$ exhibits a band gap, which is still in the visible range, and appears in an intense yellow color.

Additionally the band gap of poly(triarylamine) (PTAA) is given, which is used as a hole extraction layer for the fabrication of solar cells (see Section 2.4). With a band gap at the high energy boundary of the visible spectrum it exhibits a transparent appearance as well.

2.2 Characterization Techniques

For the characterization of the materials reported in this work, different techniques were applied to gain information about the material properties on the atomic as well as macroscopic level. In this section the basics of these techniques are briefly described to an extend, which is necessary for the understanding of the results reported in this work.

Scanning Electron Microscopy (SEM)

The scanning electron microscope records microscopic images of the surface morphology of the samples. In this work a *LEO Gemini 1530* is used for the imaging, which produces images with a resolution down to a few tens of nanometers. For the generation of the images a highly focused electron beam scans across the sample surface and interacts with the

atoms of the sample material. In the setup used for this work, two different detectors are available, recording the secondary electrons and the back-scattered electrons, respectively.

Secondary electrons result from inelastic scattering of the electrons from the electron beam with the electrons of the atoms in the sample. Correlation of the intensity of the secondary electrons with the position of the electron beam on the sample yields a topographic image of the samples surface. In this work, images taken with this method are referred to as "SE2"-images.

Back-scattered electrons, in contrast, refer to electrons from the electron beam, which scatter elastically on the atoms in the sample. Due to the preferred direction of the scattering, these electrons are detected in close proximity to the incident electron beam. Therefore, the detector is often referred to as "InLens"-detector. Since atoms with higher atomic number have a higher potential for back-scattering events than atoms with lower atomic number, the contrast of the Inlens-images can also give information about elemental distribution in the sample, showing heavy atoms in higher intensity than lighter atoms. However, other factors can influence the intensity of detected electrons in the InLens-detector as well. As an example, charged particles on the surface of the sample have a high chance of reflecting electrons, thus increasing the detected intensity at this given point. Thus, intensity variations in InLens-images do not yield a conclusive evidence of elemental contrast.

Especially in soft or chemically unstable material, the electron beam can also damage the sample. Since the kinetic energy of the electrons depend on the acceleration voltage applied, the damage can often be reduced by a reduction of this acceleration voltage. Although the fully inorganic perovskite reported in this work are expected to be more stable than their mixed organic-inorganic counterparts,[95] radiation damage can be observed even at low acceleration voltages. All images reported in this work were recorded with an acceleration voltage of $2\,\text{kV}$ and with a beam current of $80\,\text{µA}$. In repeated scans it was observed, that no changes can be seen in the SE2-images, while only minor changes in the contrast of the InLens-images are visible. Since no quantitative information is extracted from this contrast, these changes are neglected for the further evaluation of the images.

Insulating samples are often coated with a few nanometer thin, conductive carbon layer, to avoid charging effects. However, since the samples reported in this work tend to degrade under the influence of ambient atmosphere (see Section 6) and no deposition machine in inert atmosphere was available, this technique could not be applied. As an alternative, two parallel stripes of conducting copper tape were attached to the sample with a gap of approximately one millimeter in between them. Recording the images between the stripes

and in close proximity to one of the stripes could sufficiently reduce the charging effect to achieve decent data quality.

X-ray Diffraction (XRD)

To determine the crystal structure X-ray diffraction is used in different variations in this work.[96] The general working principle of this method is explained in Figure 2-3. In crystalline materials, the incoming X-rays can be diffracted or transmitted on a lattice plane. The transmitted X-rays again have a probability to be diffracted or transmitted on the next lattice plane, which occurs at an inter-planar distance of d. It is worth noting, that the diffraction vector $\hat{\mathbf{s}}$ is always perpendicular to the lattice plane on which the diffraction occurs.

The X-rays, which are diffracted from the different lattice planes, subsequently superposition, which leads to interference. For constructive interference the difference L between the paths has to be an integer multiple n of the X-ray wavelength λ. At the same time, L can be calculated from the known incidence angle Θ and the inter-planar distance d by trigonometry. This results in the equation known as Bragg's law, which is given in Equation 2-1.

$$n\lambda = 2d\sin[\Theta] \tag{2-1}$$

If the Bragg-condition is fulfilled the intensity of the diffracted X-rays increases. Reversely, this means, if for a known wavelength λ and incidence angle Θ a constructive interference is observed, the presence of lattice planes with distance d can be deduced for the sample.
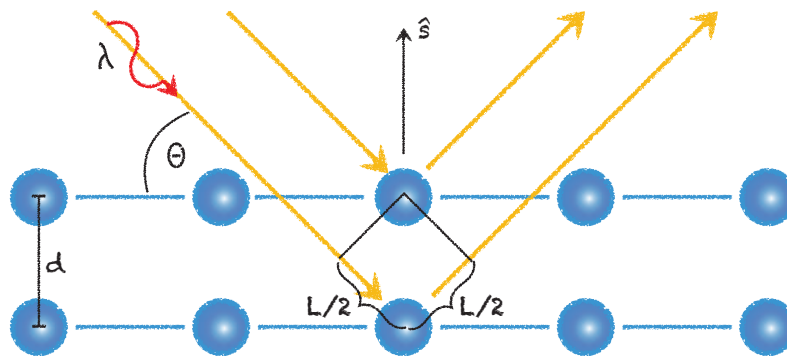
Figure 2-3: *Schematic drawing of the fundamental principle of diffraction of X-rays on a crystal lattice. The incoming X-rays under the angle Θ with wavelength λ can be either diffracted of transmitted at each plane of the lattice. X-rays, which are diffracted on two different planes with distance d interfere with each other. If the difference in the paths L is an integer manifold n of the wavelength, the interference is constructive. The diffraction vector $\hat{s}$ is plotted normalized and is always perpendicular to the lattice plane of diffraction due to conservation of inertia.*

If a large number of lattice plane distances are known, a model can be built or refined to the measurement, describing the crystallographic lattice of the sample. For this, the angular dependence of the diffracted X-rays is measured.

Sample environment

Due to the aforementioned sensitivity of the reported material to ambient atmosphere, all XRD measurements reported in this work were conducted in a custom made sample holder, which is depicted in Figure 2-4. The sample holder is made from stainless steel, sealed with a fluoroelastomer O-ring and equipped with large polyimide windows. These windows allow the transmission of X-rays, while protecting the sample from ambient atmosphere. For extended protection of the sample against oxygen and moisture, which might diffuse through the polyimide, the window is implemented as a double layer. The spacing between the layers can be purged with dry inert gas. The large size of the window allows spatially resolved measurements on all positions of a 5 cm by 5 cm sample. For X-ray measurements in different atmospheric conditions, the holder is equipped with four threaded inlets to the interior, which can be fitted with gas in and outlets. For measurements of the sample in inert atmosphere, these inlets are sealed and the holder can be transferred
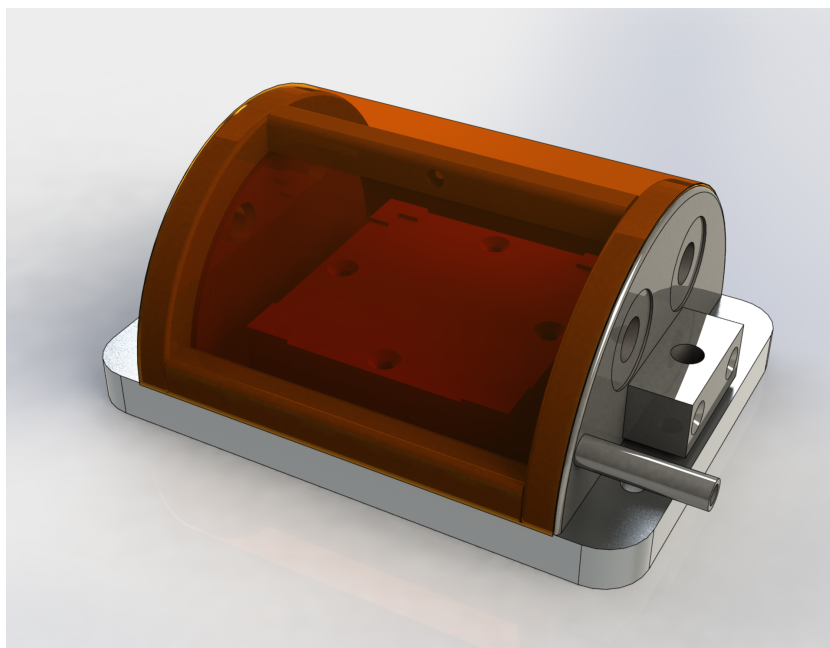
Figure 2-4: *Custom made stainless steel holder for conduction of X-ray based analysis methods such as XRD in inert atmosphere. For the transmission of the X-rays the holder features a double layer polyimide window. The spacing between the two layers of the window can be purged with dry inert gas. Four threaded inlets to the interior of the sample holder can be either capped or equipped with gas in and outlets for measurements in different atmospheres.*

into an inert gas glove box for the installation of the sample. After installation, the holder is closed and transferred out of the glove box for the measurement.

XRD measurements in the laboratory

In the laboratory, steady state, high resolution measurements were performed with a *PANalytical X'Pert Pro* diffractometer, which is equipped with a Cu X-ray-tube and a *PIXcel* line detector. The tube was operated at a voltage of $40\,\mathrm{kV}$ and a current of $40\,\mathrm{mA}$. The Cu-K$_\beta$ energy is attenuated by several orders of magnitude by a Ni-filter and the incident beam is manipulated with a $5\,\mathrm{mm}$ wide mask and a fixed divergent slit of $1/16°$.

The setup was used in the Bragg-Brentano geometry, in which the incident angle and the detection angle are scanned simultaneously and thus equal throughout the measurement. This geometry is also known as Θ-2Θ-geometry. While this methods yields high count rates and thus high signal-to-noise ratios for a given measurement time, it implicates several disadvantages. For a fixed slit in the incident X-ray path, the footprint on the sample varies with the angle of the incident beam during the measurement. This implies altering of the interaction volume including the penetration depth of the radiation. Especially for inhomogeneous samples this invokes complications, since the resulting pattern contains contributions from different areas of the film depending on the angle. For the divergence slit and mask used for the measurements presented in this work, this results in an X-ray footprint of the sample of $7\,\mathrm{mm}$ width and a variable length between $1.5\,\mathrm{mm}$ and $0.2\,\mathrm{mm}$ for the angular range of 2Θ between $10°$ and $70°$.

Since incident angle and detection angle are varied symmetrically during the scan, the diffraction vector $\vec{s}$ remains perpendicular to the surface of the sample. Thus, a measurement, which is performed in this geometry only contains contribution from lattice planes, that are perpendicular to the surface. In highly textured films, this leads to strong attenuation or even cancellation of reflexes, which originate from lattice planes, that are not parallel to the surface.

XRD measurements at the synchrotron

For high-throughput measurements, which enable spatially resolved studies such as an XRD line scan across the sample, synchrotron radiation was used, which provides a significantly higher X-ray flux as compared to a conventional X-ray tube. For the XRD experiments described in this work, the energy of the incident beam was selected with an X-ray monochromator to be $8.048\,\mathrm{keV}$. This energy was chosen, since it is the energy of the Cu-K$_\alpha$ line, which is used for the laboratory based measurements, and thus allows an easy comparison of the diffraction patterns recorded in both measurements. Using horizontal and vertical slit systems, the footprint of the X-rays on the sample was defined to

be ~3 mm by 3 mm. The diffraction was detected with a two dimensional *Dectris Pilatus 100K* detector. Images were recorded for different diffraction angles, covering an angular range between 5° and 62°. The computation of common angle-dependent diffraction patterns from these images will be described below.

In contrast to the laboratory based measurements, the geometry used for the synchrotron based measurements was chosen to be a fixed incident angle ω geometry with $\omega = 5°$. This geometry is advantageous over the aforementioned Θ-2Θ-geometry, since the diffraction vector $\vec{s}$ does not remain parallel to the surface of the sample but rotates with the altering detection angle. Thus, even in highly textured films, all lattice planes can be probed without movement of the sample.

XRD measurement at the metal-jet X-ray tube

For time resolved in-situ investigation of the crystal structure measurements at a metal-jet X-ray source were performed.[97] In common X-ray tubes the X-rays are generated by irradiation of a solid metal anode with an electron beam. The flux of the generated X-rays is limited by the heat load, the anode can compensate without deformation or melting. In the metal-jet source, this limitation is overcome by employing a jet of liquid metal as anode. Thus the actual anode material is continuously exchanged and maintains a sufficiently low temperature. As a result, a very small X-ray source spot and high flux can be achieved. The liquid anode of the source used in this work consists of 80 % gallium and 20 % indium. Since no edgepass-filter for the suppression of the Ga-K$_\beta$ lines was used, the emitted radiation is not monochromatic, which can be seen in the spectrum of the tube in Figure 2-5. The dimensions of the incident X-ray beam were tailored by vertical and horizontal slit systems to achieve a footprint of approximately 3 mm width and 10 mm length on the sample. The intensity of the diffraction was recorded with a *Dectris Pilatus3 1M* 2D-detector. Owing to the large detector area, a diffraction pattern with angular range between 1.4° and 35.4° could be acquired without moving the detector. The computation of common angle-dependent diffraction patterns from these images will be described below.

Similar to the measurements performed at the synchrotron as described above, the incident angle of the X-rays was kept constant at $\omega = 11°$ during these measurements. However, since the radiation of the tube is not parallel but divergent, the Bragg condition is only precisely fulfilled for one specific detection angle. This results in a blurring of the diffraction peaks apart from this specific angle.

For easier comparison of the diffraction patterns acquired in the regular laboratory measurements and the patterns acquired with this setup, the calculated geometric diffraction angles are translated into diffraction angles as they would occur for Cu-K$_\alpha$ radiation. For
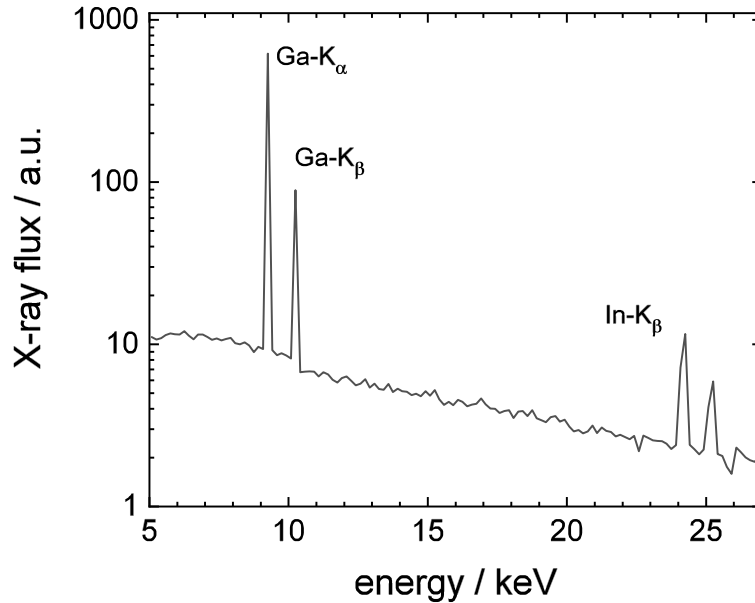
Figure 2-5: *Simulated spectrum of the liquid metal-jet X-ray tube. The emission lines of gallium and indium are labeled. Since no filter was applied for the measurement, the excitation can not be considered to be mono-energetic.*

this, Equation 2-1 is evaluated for the wavelength of the Ga-K$_\alpha$ and the Cu-K$_\alpha$ line, respectively, and combined. On this scale the angular range of this measurement translates to 10° to 40°.

Processing of two dimensional diffraction images

In most laboratory measurements the incident angle and detection angle are varied in a plane, which is perpendicular to the samples surface, as depicted in the simplified schematic drawing in Figure 2-3. However, the Bragg condition can of course be fulfilled by any angle in the three-dimensional space, regardless of the orientation of the samples surface in respect to the incident beam.[98] For samples with randomly oriented crystallites this results in diffraction rings, which are concentric circles around the incident beam. The position on this circle is described by the azimuthal angle, which is defined to be 0° for the above described laboratory geometry.

However, for highly textured samples, which are kept in a fixed position during the measurement, the Bragg condition might not be fulfilled for all azimuthal angles resulting in circle sections. Since the azimuthal range of these circle sections is determined by the degree of texturing, a mono crystalline sample shows a diffraction pattern of distinct dots in the diffraction plane.[99] Depending on the focus of the evaluation of the diffraction images collected by 2D-detectors, the information about the texturing can be gained from

evaluating the azimuthal distribution of the diffraction reflexes. In this work the focus of the evaluation is put on the identification of the crystal structure from the images. Therefore, only the intensity of the diffraction is determined by azimuthal integration over the diffraction rings.

For the evaluation of the images taken during the synchrotron measurements, a software was specifically developed. Using vector algebra, the physical location of each pixel in each image of the measurement was calculated in the 3D-space with respect to the incident beam. With a given sample-to-detector distance, this location can be translated into a diffraction angle by basic trigonometry. Since a detector with comparably small width was used, which results in a small azimuthal range, all pixels of all images were used for the integration. The intensity of all pixels was integrated with respect to the individual diffraction angle, which was binned in steps of 0.01°. The intensity of each bin was normalized by the number of contributing pixels, thus correcting for the different azimuthal range and resulting in a common angle-dependent diffraction pattern.

For the measurements at the metal-jet source, a much larger detector was used, which covers not only a large 2Θ-detection-angle range, but a larger azimuthal range as well. For the evaluation of these images a software by Roland Mainz was used, which performed the circular integration as described above. This software features the possibility, to limit the circular integration to a certain azimuthal range. For the evaluation described in this work, a narrow azimuthal range of $-20°$ to $20°$ was used to minimize the error of falsely attributing changes in texturing to trends in the respective reflex intensity. As for the evaluation of the synchrotron data, described above, the software used here outputs common diffraction patterns of X-ray intensity over diffraction angle.

Analysis of the diffraction patterns

From the analysis of XRD-patterns information about the crystal structure of the material can be determined, such as the lattice parameters and an estimation of the domain size. Therefor, a simulated pattern, which is based on a crystallographic model of the sample, is refined to fit the measured data.

For the refinements presented in this work, the software *PowderCell* was used,[100] which provides a fast option for LeBail-fitting.[101] The LeBail-method is a suitable algorithm for evaluating thin-film measurements, since the intensity of each diffraction peak is fitted individually, thus neglecting the influence of texturing. The position of the calculated reflexes, however, is fitted to the measured peak position by adjustments of the lattice parameters of the model. Thus, the lattice parameters of the measured sample can be read from the parameters of a well fitted model.

Since the broadening of the diffraction reflexes yields information about the size of the domains and the stress within the domains, the width of the peaks is refined as well. Deconvolution of the measured peak broadening and the broadening introduced by the setup, yields the broadening, which is actually caused by the size and strain effects. In *PowderCell* this estimation is performed with the Williamson-Hall method after the refinement.

For the analysis of the patterns acquired in the laboratory with the Cu-tube, the Kα_2 line was stripped by automatic deconvolution with the software *X'Pert HighScore Plus*, which was also used to remove the background before the refinement. After loading the measurements into *PowderCell* the theoretical model was refined by iterative fitting of the zero-shift, the scale factor, the lattice parameters *a*, *b* and *c*, and the peak broadening parameters *u*, *v* and *w*. The individual peaks were modeled with Pseudo-Voigt functions. For the estimation an experimental breadth of the setup of 0.06° was assumed, which is estimated from the applied fixed divergence slit of 1/16°.

X-Ray Fluorescence (XRF)

In order to determine the elemental composition of the samples, X-ray fluorescence measurements were performed. XRF is a "photon in – photon out" process, in which one of the core electrons of the sample material is exited by an X-ray photon with a higher energy than its binding energy. Upon recombination of the resulting core hole with an electron from a higher level, the difference in energy between the two involved core levels is emitted in the form of a photon. Since the energetic levels, and therefore the difference between the levels, is specific for the element, the energy of these photons can be used as a fingerprint to identify the probed material. Quantitative analysis of the intensity of each fluorescence line in a measurement yields the chemical composition of the sample.

For this, a model of the sample is generated based on an initial guess of the composition of the sample and the theoretically expected fluorescence is calculated, whilst accounting for re-absorption, attenuation and other processes. In an iterative procedure, the calculated fluorescence is compared with the measurement, the model is adjusted correspondingly and the calculation is repeated with the new parameters. If the theoretical calculation fits the measurement sufficiently well, the composition of the sample can be read from the model. While the described procedure represents a very simplified method of quantification, additional information about setup geometry, incident fluxes, detector responses and more is required for a real and reliable quantification process.

The measurements reported in this work were conducted at a *Bruker M4 tornado*. The setup is equipped with a rhodium X-ray tube with a polycapillary optic, that focuses the

X-rays on a spot of ~20 µm diameter. The tube was operated at a voltage of 50 kV and a current of 200 µA. The quantification was performed with the software *XMethod*, which is supplied by the manufacturer. While the exact fitting routine of the software is not disclosed, its calculations are based on measured fluorescence spectra of single element reference samples. To increase the precision of the quantification, reference measurements of samples with known composition can be supplied.

For the evaluations reported in this work, reference samples of the binary compounds CsI and PbI_2 were measured and used for the fitting routine. Since no sample of the ternary phase $CsPbI_3$ with reliably and precisely known composition was available, no reference measurement could be supplied with a composition close to the expected composition of the samples reported here. This significantly increases the margin of error for the quantification reported here. Therefore, the error on the absolute composition is estimated to be 10 % for all measurements reported in this work. Albeit this contemplation, the determination of a compositional range with no detectable secondary phases in XRD measurements (see Section 3.3) as well as in-situ measurements during sample fabrication (see Figure 2.3) suggest, that the true margin of error is significantly lower.

Unaffected of this large error on the absolute composition of the sample are relative changes of the composition, which can be observed within a sample and among different samples with similar composition. Therefore, the studies on the composition of the sample, which are reported in this work, are presented with the error on these relative changes. However, for the absolute number, which is given for the composition of the layer, the absolute error has to be considered.

Ultraviolet-Visible Spectroscopy (UV-Vis)

For UV-Vis spectroscopy the transmission and reflection of light in the visible and ultraviolet range of the electromagnetic spectrum is measured. Depending on the configuration of the setup, light in the infrared region can be considered for this type of measurement as well. The measurement of these two quantities yields information about various optical properties of the sample such as the band gap and absorption coefficient. They also enable to make estimations about surface roughness and layer thickness in some cases.

In this work, the transmission and reflection measurements were performed in a specifically designed setup with automated acquisition of reflection and transmission. The sample is mounted onto a motorized stage, that can move in two directions in the samples plane thus allowing a 2D-mapping. To avoid the influence of ambient air, the setup is installed in a nitrogen filled glove box. A schematic drawing of the setup can be seen in Figure 2-6. The setup employs a stabilized, fiber-coupled halogen white light source

(*Thorlabs SLS201/M*) which is located outside of the glove box and connected to the setup with optical fibers (*Thorlabs M38L02*). The light is collected with an integrating sphere (*Avantes AvaSphere-50*), which is connected to a spectrometer (*Avantes AvaSpec-2048XL*) outside of the glove box.

For the transmission mode, the light is focused onto the sample from below with a collimating mirror and a lens and the transmitted light is collected by the integrating sphere. For the reflection mode, the light is focused onto the sample from the top and through the integrating sphere. The direct reflection as well as the diffuse reflection are collected with the integrating sphere. For both geometries the spot size on the sample is ~1 mm in diameter.

It was found, that the measurement of the reflected intensity can be falsified by light, that is transmitted through the sample, then reflected on the lens for the transmission illumination and transmitted back through the sample into the integrating sphere. To attenuate this effect, a shutter of low reflecting material is placed below the sample during reflection mode.

Even though the light source is specified to emit photons at wavelengths between 300 nm and 2600 nm, the measuring chain of optical fibers, focusing lenses, integrating sphere and detector result in a narrowed usable wavelength range of 400 nm and 1100 nm as can be seen in Figure 2-7.
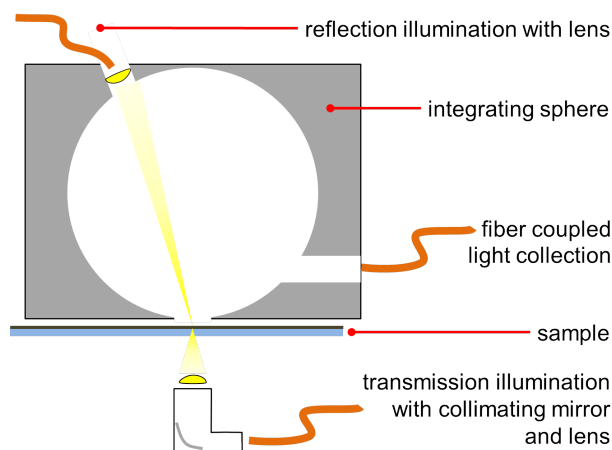
Figure 2-6: *Schematic drawing of the setup used for the UV-Vis spectroscopy. The sample is placed below an integration sphere with the thin-film facing up. For the reflection, the sample is illuminated through a fiber coupled lens. For the transmission the illumination is performed with a fiber couples collimating mirror and a lens. The intensity is measured with an integrating sphere, thus covering direct and diffuse components.*

For normalization of the measurement a reference spectrum and a dark spectrum have to be taken, for both, reflection and transmission. For the transmission, the reference can be taken either with a bare substrate or without any specimen in place. In this work the references were taken in the latter configuration to avoid complications due to multiple reflections on the surface of the substrate. For the reflection mode, the reference is taken by a reflection standard, with a known, high reflectivity. Within the limits of the precision, the reflectivity of the standard is assumed to be 100% in this work.

Using the transmission reference spectrum $S_{trans,ref}$ and the transmission dark spectrum $S_{trans,dark}$, the transmission T can be calculated from a measured spectrum $S_{measure}$ from Equation 2-2.

$$T = \frac{S_{measure} - S_{trans,dark}}{S_{trans,ref} - S_{trans,dark}} \qquad (2\text{-}2)$$

The reflection R can be calculated in the same way, using the reflection references. The absorption A of the light within the sample is defined by $A = 1 - T - R$.[102] It should be noted, that this equation is not strictly fulfilled by the setup used in this work, since transmission and reflection are measured with different directions of the incident light. The error caused by this inaccuracy has to be considered during the analysis of the data.
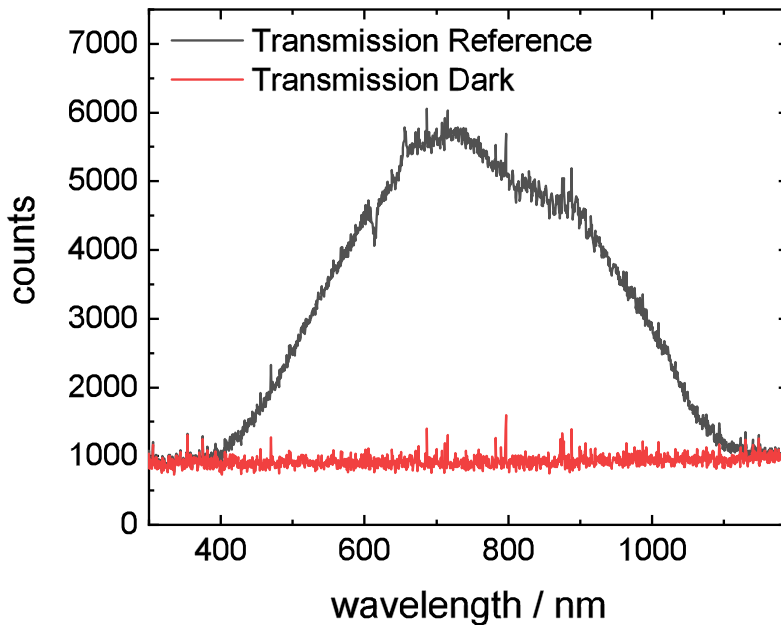
Figure 2-7: *Reference and dark spectrum for the transmission geometry, as measured by the aforementioned UV-Vis setup. Each measurement was acquired by internal average of the spectrometer over ten spectra with integration time of each $2\,\mathrm{s}$. The spikes in the remaining noise be can mostly accounted to static differences in pixel intensities of the detector. The measurement chain yields sufficiently high intensity between $400\,\mathrm{nm}$ and $1100\,\mathrm{nm}$.*

As an additional error of the measurements, a drift in the raw spectra over time was observed. This drift was corrected before performing the aforementioned calculations. Details about the drift and the correction can be found in Appendix A.

Since the absorption A of a sample strongly depends on the thickness d of the layer, the absorption coefficient α as known from Lambert-Beers law is more handy to describe the material properties.[103] The absorption coefficient can be calculated from transmission and reflection measurements by Equation 2-3.

$$\alpha = -\ln\left[\frac{T}{1-R}\right]\frac{1}{d} \tag{2-3}$$

There are different ways to extract the band gap from the absorption coefficient, which increase in complexity with increasing deviation of the modeled cell from an ideal semiconductor. In this work the focus is put on the description of relative changes of the materials properties upon changes in the composition and other preparation parameters, rather than on the absolute determination of the quantity. Therefore, as an easy measure the absorption onset is extracted, which is defined as the inflection point in the absorption coefficient and is determined from the derivative of the absorption coefficient. The resulting peak is fitted in first approximation by a Gaussian curve to determine its center position.

Photoluminescence (PL)

Photoluminescence is defined as spontaneous emission of light in a material after excitation with photons.[104] In semiconductors it usually means the excitation of an electron hole pair above the band gap, which thermalizes and subsequently recombines radiatively. Therefore, the energy of the emitted photons can be used as a measure for the band gap of the semiconductor.

In a device in open-circuit conditions the excited charge carriers have to recombine either radiatively or non-radiatively. Non-radiative recombination mainly occurs on the basis of lattice defects or defect states, which lower the quality of the material. Considering this, the quantum yield of the radiative recombination allows an estimation of the magnitude of the non-radiative recombination, thus being a measure of the quality of the semiconductor.

In the special case of time-resolved PL (TRPL) measurements, the emission of the photons after a short excitation pulse is measured over time. The decay of the emission yields information about charge carrier dynamics within the semiconductor.

In this work, PL is applied as absolute calibrated PL imaging, as well as in TRPL. For the PL imaging, two high power LEDs with emission at 455 nm illuminate the sample

with an equivalent intensity of one sun (~70 mW/cm^2). The emitted PL photons are transmitted through a tunable liquid crystal filter and acquired by a calibrated CCD-camera in order to achieve a set of hyperspectral images. The PL spectrum of each pixel can be accessed by reading the intensity of the respective pixel from all images taken at different wavelength settings of the filter. In the measurements performed for this work, the field of view of the camera is ~22 mm×16 mm. The calibration of the measurement chain allows the calculation of the absolute number of detected photons and therefore the PL quantum yield of the material. Dividing the number of photons of the photo luminescence by the absolute number of incident photons (=1.6 · 10^{21} photons/m^{2}s the external PL quantum yield (PL QY) can be calculated.

The TRPL in this work was measured in a setup equipped with a tunable laser. The laser was set to a wavelength, which is sufficiently below the band gap of the material of the sample (670 nm) in order to maximize the crossection for excitation. The emitted photons were detected with a photo-multiplier tube and time-resolved single photon counting electronics. In this setup the sample is mounted on a motorized linear stage to allow the measurement of several spots on the sample along a line. The stage has a travel range of 20 mm.

Optical-Pump THz-Probe (OPTP)

For OPTP measurements the semiconducting material is photo-excited with a femtosecond laser pulse, that has a photon energy of 3.1 eV, which is above the band gap of the material. After a variable delay time the excited charge carriers are probed with a laser pulse, which has an energy of a few meV, corresponding to a frequency in the THz region. Depending on the density and mobility of the photo-excited charge carriers, the THz pulse is attenuated and phase shifted. By measuring this attenuation and phase shift dependent on the delay of the THz beam, the recombination of the charge carriers can be observed time resolved.

Detailed modeling of the attenuation and the phase shift yields the sum mobility of the excited electrons and holes. Since the measurement and the evaluation of the OPTP data reported in this work were conducted by Hannes Hempel, no details on the measurement and evaluation will not be presented in this work. More information on the measurements and the modeling can be found in [105, 106].

Current-Density–Voltage (JV) Scan and External Quantum Efficiency (EQE)

For the characterization of the full stack solar cells JV and EQE measurements were performed in a glove box. The procedure of the measurements was already reported in [107] and thus will be discussed only briefly at this point.

In a JV-scan the voltage-dependent current density of a solar cell is measured. In this work only JV-scans on illuminated cells will be used. For these measurements the cells are placed on a sun simulator (Oriel LCS-100 class ABB), which illuminates the sample with an equivalent power of one sun. With a source measure unit (Keithley 2400) the voltage was swept in 20 mV steps. For each step, the current was integrated over 40 ms after a settling time of 40 ms and converted into a current density by dividing it by the known active area of the cell. The evaluation of the JV-scans yields the open circuit voltage (V_{OC}), the short circuit current density (J_{SC}), the power conversion efficiency (PCE) and the fill factor (FF).

The EQE denotes the wavelength dependent ratio of the number of charge carriers at the electrical contacts of the cell over the number of incident photons. For this, white light of a xenon arc lamp (Newport 300 W) was guided through a monochromator (Newport Cornerstone 260) and a chopper, and coupled into an optical fiber, which was pointing onto the cell. The electric response of the cell was monitored with a lock-in amplifier (Stanford Research SR830). EQE measurements give information about wavelength dependent deficits of solar cells, which might be caused by reflection of the light on the surface, bulk or interface recombination, or parasitic absorption of the light, for example in contacting layers.

2.3 Evaporation Chamber with In-Situ Characterization

A vacuum evaporation system was specifically designed and build for the evaporation of perovskite materials, to allow well defined and reproducible fabrication of perovskite thin-films and bring more insight into the growth mechanisms. Since the application of the machine should not be limited to the fully inorganic $CsPbI_3$ perovskites discussed in this work, a strong focus was put on the flexibility of the chamber regarding evaporation possibilities as well as in-situ measurement capabilities. As the perovskite materials are known to be sensitive to ambient atmosphere, the chamber was to be fitted into a nitrogen filled glove box, thereby protecting the sample from oxygen and moisture.

Evaporation Chamber

The chamber was designed in a compact and modular way, allowing to change flanges to meet requirements for different in-situ setups. A drawing of the basic chamber design can be seen in Figure 2-8. The chamber consists of a main cube with all six side flanges being replaceable. The flanges are sealed by FKM fluoroelastomer (FKM) O-rings allowing for a base pressure below $8.5 \cdot 10^{-8}$ hPa. For the current application, the back flange is equipped with an adapter to DN 160 CF and connected to a turbo molecular vacuum pump. The front flange accommodates a large 20 cm quartz view port for visual process control. The two side flanges are meant to be used for low angle optical reflection and X-ray diffraction measurements but are left blank at this state of the development.

To place the substrate, a custom made substrate holder is mounted onto the top flange as shown in Figure 2-9. The holder consists of a substrate carrier, a ceramic heater, and a cooling feedthrough to the outside of the chamber. The substrate carrier can be equipped with one 5 cm×5 cm substrate or four 1 inch×1 inch substrates, respectively.
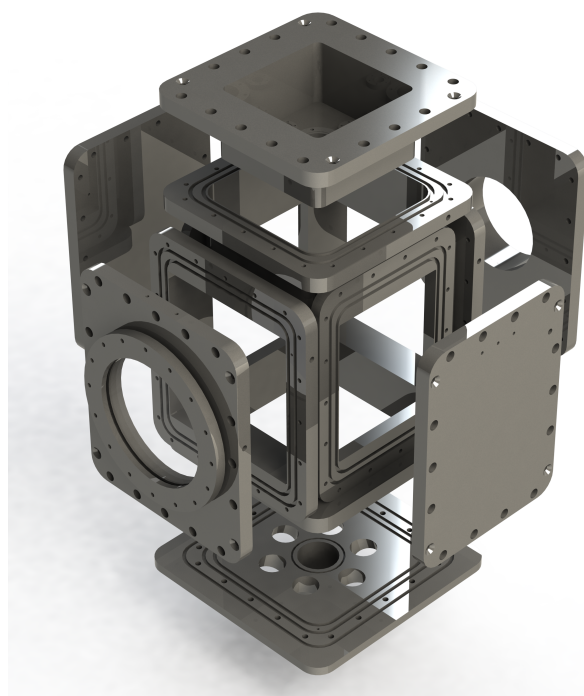
Figure 2-8: *Schematic view of the evaporation chamber consisting of the center cube with all six side flanges being exchangeable depending on the application. For this work it was equipped with blank flanges for the sides, a large viewport in the front, a CF 160 CF adapter flange for the vacuum pumps in the back, sample holder in the top and and adapter with several CF flanges for evaporation sources and optical viewports in the bottom.*
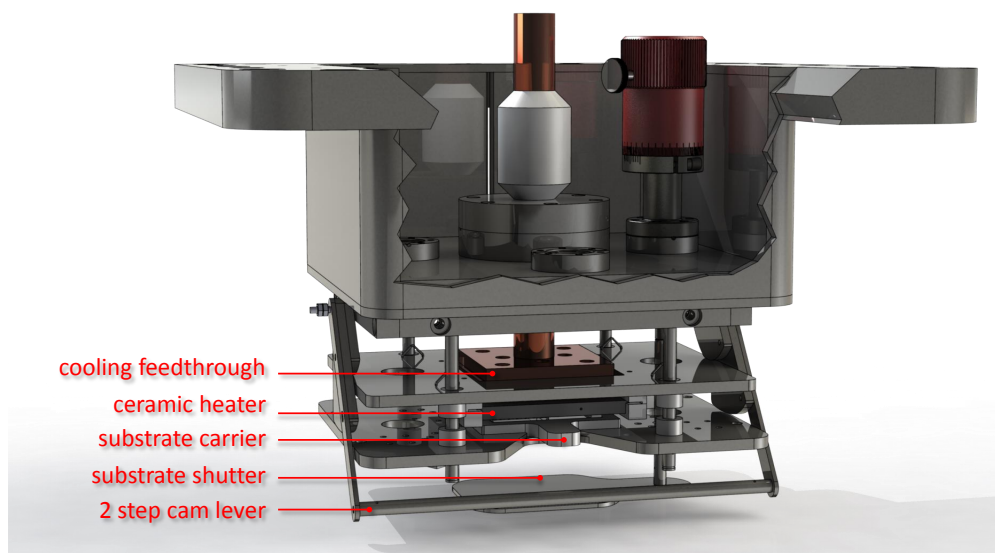
Figure 2-9: *Schematic drawing of the top flange with the mounted sample holder. The substrate holder includes a ceramic heater and a cooling feedthrough which can be brought in contact with the substrates by a two step cam lever mechanism. The substrate can be shaded from the evaporation sources located in the bottom of the chamber by a substrate shutter which is mounted on a rotary vacuum feedthrough with manual operation from the outside of the chamber.*

Heater and cooling are utilized by a two step cam lever mechanism which can press the substrate onto the heating and the cooling block. The heater is equipped with a type-K thermocouple, which is used to estimate the substrate temperature and control the heater temperature in a closed loop. At the current state, no active cooling system is mounted on the cooling feedthrough so that the temperature can be adjusted between ambient temperature and 150 °C. The sample can be protected by a substrate shutter mounted on a rotary feedthrough in the top flange as well. Quartz balance monitors are mounted in close proximity to the substrate carrier to allow precise control of evaporation rates and film thickness. The quartz balances are equipped with shading tubes to ensure, that each quartz is only exposed to the vapor of a single source and crosstalk is minimized.

At the bottom of the chamber an adapter is mounted containing six DN 40 CF flanges arranged in a circle and tilted in-plane to point to the center of the substrate. Centered in this circle an additional DN 63 CF flange is mounted facing the substrate perpendicularly. The flanges can be used for evaporation sources as well as for viewports for in-situ process

control. The tilting of the DN 40 CF flanges is not only beneficial for directing the evaporation from the sources onto the substrate but also enables direct reflection measurements with equal incident and detection angle configuration. At the current state of the setup, three crucible based thermal evaporators (*CreaPhys DE-4-CF40-SHE*) are mounted in the DN 40 CF flanges. Each evaporator is equipped with a type-K thermocouple for temperature control and a rotating source shutter. To protect the evaporator material from the corrosive influence of halide vapor, all metallic parts coated with gold. Two more opposing flanges as well as the DN 63 CF flange hold quartz windows for optical in-situ process control.

In-Situ Characterization Setup

All system status parameters of the different components of the chamber are logged by a software written by Roland Mainz, to have full control over the evaporation process and monitor the conditions of the setup. These include vacuum pressure of the system, substrate temperature, temperature and electrical power of the evaporation sources, evaporation rate and current partial thickness of any of the source from the quartz balance monitors as well as the quartz crystal quality. By monitoring these parameters during the process any abnormal situation of the evaporation can be detected and possibly readjusted.

Additionally, to gain insight into the formation processes during the evaporation of the perovskite films, the optical reflection of the films is monitored spectrally as well as spatially resolved. A schematic drawing of the arrangement of the setup is depicted in Figure 2-10. A high power halogen lamp with stabilized power output (*Thorlabs SLS301*) is mounted on one of the DN 40 CF flanges illuminating the entire substrate. To reduce the heat load of the lamp onto the sample, two custom made H_2O filters of each $1\,cm$ thickness are mounted in the beam path of the lamp. At the opposing DN 40 CF flange an off-axis parabolic mirror is mounted to focus the reflected light of a $8\,mm$ diameter measurement spot on the sample into an optical fiber which is connected to a spectrometer (*Avantes AvaSpec-2048*). This allows to record the evolution of the reflection spectrally resolved. It has been shown, that the evaluation of the white light reflection can yield valuable information about semiconductor thin-film properties, such as film thickness, surface roughness and band gap (see Section 3.5).[108] Although the geometry of the reflection is set to have the same incident and reflection angle in the plane (as shown in Figure 2-10), this plane is slightly tilted against the surface. This geometry was chosen, since the area of interest for the in-situ measurements is not located in the center of the sample, but slightly shifted to one side, making the geometry slightly "off-axis" (see Section 3.5 for details). Therefore, the measured reflection does contain influences of
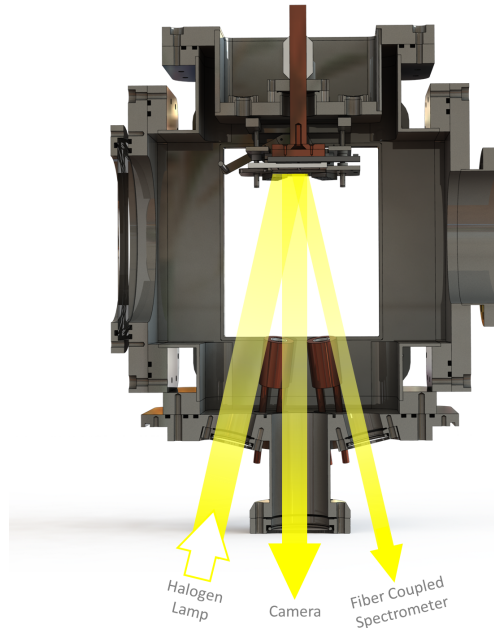
Figure 2-10: *Schematic drawing of the vacuum chamber designed for perovskite evaporation in cut side view. In the bottom flange three optical view ports are mounted additional to the evaporation sources, allowing in-situ monitoring of the optical parameters of the films. A halogen white light source and a fiber coupled spectrometer are set up at the opposing ports. A camera is mounted on the centered flange with a perpendicular view onto the substrate.*

the direct and diffuse reflection, thus complicating a quantitative analysis. In this work, however, the analysis focuses on a comparison of different evaporation processes, which were acquired in the same geometry, thus reporting relative changes rather than absolute values.

Since this method is limited to monitoring one specific spot on the substrate, which is determined by the direction of the off-axis mirror, an additional method is employed monitoring the diffuse reflection of the entire sample spatially resolved. Therefore, a camera (*The Imaging Source DBK 41AU02.AS*) is mounted on the center flange in the bottom adapter facing the substrate perpendicular to monitor the uniformity of the film formation. The sensor of the camera itself is not equipped with an infrared blocking filter. Thus, an external infrared filter (*Baader UV/IR Cut*) is installed for measurements with the halogen light source, which only transmits light with wavelength between 400 nm and 680 nm to avoid saturation of the detector.

Combining the results from monitoring the spectrally and the spatially resolved reflection of the substrate a detailed insight into processes happening during the formation of the films can be gained.

2.4 CsPbI$_3$ Thin-Film Preparation and Application

For the studies, which are reported in this work, thin-film samples of CsPbI$_3$ are prepared by thermal evaporation. The optical properties of these samples are studied and solar cells are prepared to investigate their potential as photoabsorbers in thin-film solar cells.

Evaporation Procedure

For the deposition of all films described in this work, the evaporation chamber was configured in a way, that the crucibles of two evaporation sources, which are opposing each other, are filled with CsI and PbI$_2$ salts, respectively. Both materials were acquired from *Sigma Aldrich* as 10 mesh beads and have a purity of 99.999 % on trace metals basis. Due to the opposing orientation of the sources a lateral gradient in the composition of the final film is expected, thus enabling to study the material properties depending on the composition within a single substrate.

After the substrates are mounted, the chamber is pumped down and a base pressure of $<10^{-7}$ hPa is awaited. Subsequently, the sources are individually heated up with closed substrate shutter. When the desired evaporation rate read by the quartz balance monitors is reached, the rate of each is individually controlled and kept constant by a PID-controller (*Eurotherm 3504*), which monitors the rate and adjusts the electrical power of the evaporation sources. During heating up of the sources the substrate heater is turned on as well. The heater and a thermocouple within the heater are connected to a PID-controller as well, which guarantees a stable substrate temperature over the whole process. When the desired source temperatures and substrate temperature (T_{sub}) are reached and stabilized, the process is started by opening the substrate shutter.

After the required thickness of the film as read by the quartz balance monitors is reached, the substrate shutter is closed and the substrate heater as well as the evaporation sources are switched off for cool down. The thickness of the absorber layers reported in this work was estimated from the quartz balance monitor readings to be (500 ± 20) nm. After all components are sufficiently cooled down, the chamber can be vented with nitrogen and the samples are taken out, directly into the inert atmosphere of the glove box.

Thin-Film Solar Cells

The most common type of solar cells is based on single crystalline silicon, which is cut in wafers with thicknesses down to 0.18 mm. The working principle of these cells is based on the doping of the silicon material to achieve p and n-type material, which form an intrinsic space charge region in between them. The charge carriers are generated in this

space charge region and transported to the electrical contacts through the field of the doped layers.

In contrast, thin-film solar cells often do not show this strict separation between these layers. In perovskite materials even the debate about the type of doping is still ongoing, which seems to depend strongly on the fabrication conditions.[109–111] The architecture of perovskites based solar cells is partially adopted from dye-sensitized solar cells, employing the perovskite material as photoabsorber. It is sandwiched between two very thin semiconducting layers, which act as charge-selective contacts due to their band alignment.

Thus, separated charges are generated in the photoabsorber by the incoming photons and randomly drift through the absorber material. If they reach the respective charge transport layer, they are transported to the electrical contact.

Solar Cell Fabrication

Solar cells were prepared, employing the material described in this work as photoabsorber. Since the focus of this work is put on an improved understanding of the materials properties, rather than on maximizing the PCE of the full solar cell, only little effort was put into finding optimal contacting layers for this specific absorber. Nevertheless, the contacting layers described here allow a comparison of absorber materials produced with different evaporation parameters. The details of the fabrication of the cells was already described in [107]. At this point the description of the fabrication will be limited to the details, which are relevant for the understanding of the results presented in this work.

Glass substrates with laser patterned ITO (from *Automatic Research GmbH*) were coated with poly(triarylamine) (PTAA). ITO is used as a transparent conducting front contact to allow the illumination of the cell from this side, with PTAA being a p-type semiconductor, that acts as a hole transporting material, whilst blocking electrons from the ITO contact. These substrates were transferred into the evaporation chamber without exposure to ambient air and the $CsPbI_3$ absorber was evaporated (see details below). Subsequently, the sample was transferred into a second evaporation chamber, where fullerene C_{60} and BCP were evaporated as n-type electron transporting material and copper as metallic back contact. To reduce the contact resistance, the contact areas are covered with silver paste. The resulting layer stack can be seen in Figure 2-11(a). A schematic drawing of the cell layout, showing the structuring of the different layers on the $1\,\text{inch}\times1\,\text{inch}$ glass substrate, is depicted in Figure 2-11(b). The layer patterning of the ITO electrically separates the six different cells from each other. Since the PTAA layer is deposited by spin coating, it covers the entire substrate and has to be partially removed in order to reach the front contacts. The $CsPbI_3$ layer can either be evaporated through a mask,

(a)

(b)
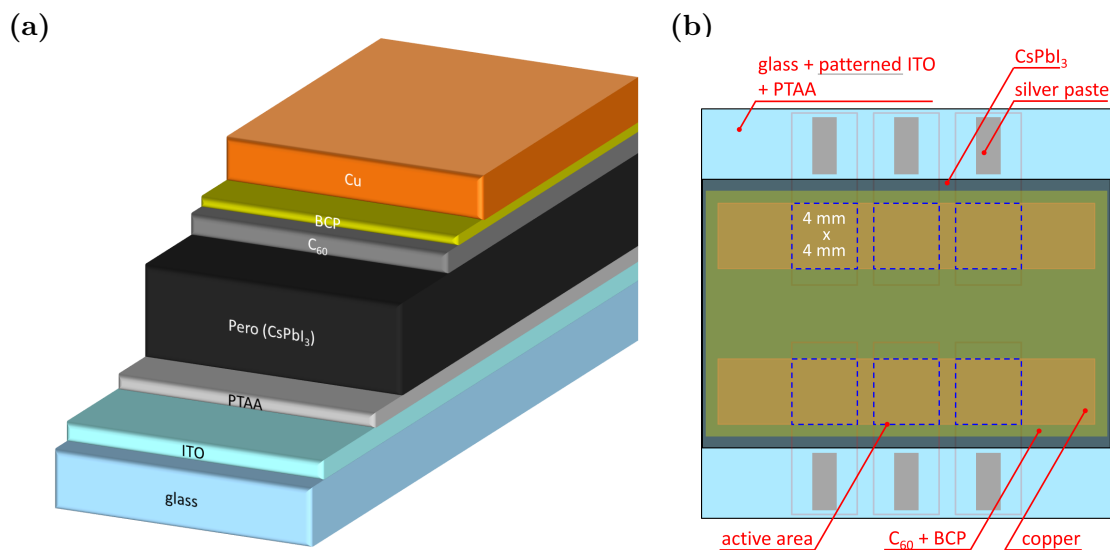
Figure 2-11: *(a) Schematic view of the layer stack for the fabrication of solar cells consisting of glass, laser patterned ITO, PTAA, CsPbI₃ (500 nm), C₆₀ (23 nm), BCP (8 nm) and copper (100 nm). The cell is illuminated from the glass side. (b) Schematic drawing of the cell layout for the solar cell fabrication on 1 inch×1 inch glass substrates. The active area for the individual cells is defined by the overlap of the ITO areas separated by the laser pattering and the evaporated copper stripes, which results in 4 mm×4 mm sized areas.*

leaving out the area of the front contacts, or be removed together with the PTAA. C_{60} and BCP are evaporated with a mask, shading the front contacts. Finally, two copper stripes are evaporated through a mask, forming the back contact. The active area of the cell is defined by the overlap of the ITO front contact rectangles with the copper back contact stripes and results in a $4\,\text{mm}\times4\,\text{mm}$ area.

For the evaporation of the $CsPbI_3$ absorber layer for the solar cells described in this work, four $1\,\text{inch}\times1\,\text{inch}$ glass substrates were mounted for each run. The evaporation rates of the CsI and PbI_2 sources were set to result in a nominal ratio of $[CsI]:[PbI_2] = 1.2{:}1$ to ensure, that the evaporation would yield four samples with brown γ-$CsPbI_3$. The arrangement of the substrates with the orientation of the single cells and their resulting composition is shown in Figure 2-12 and yields 24 sub-cells in total. The aforementioned gradient in the composition of the $CsPbI_3$ thin-films, results in sub-cells with six different compositions of $[CsI]/[PbI_2] = 1.10$, 1.13, 1.16, 1.24, 1.27 and 1.30, respectively. Since four sub-cells for each composition are oriented on a line perpendicular to the gradient, the reproducibility of the cell fabrication can be investigated. Unfortunately, all compositions used for the cell fabrication are more CsI-rich than the compositions used in the samples, which were characterized by the techniques mentioned above. Thus, the optical properties of the
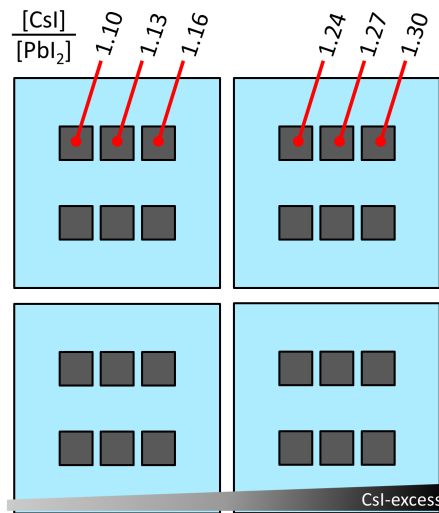
Figure 2-12: *Sample alignment during the evaporation of the CsPbI$_3$ photoabsorber for the fabrication of full stack solar cells. The gradient in the composition due to the evaporation characteristics of the evaporation sources results in four different [CsI]/[PbI$_2$]-atomic ratios of* 1.10, 1.13, 1.16, 1.24, 1.27 *and* 1.30, *respectively. The four cells which are aligned perpendicular to the gradient for each composition can be used to investigate the reproducibility of the cell fabrication.*

compositions used for the cell fabrication can only be estimated by careful extrapolation of the known values for less CsI-rich compositions.

3

Growth and Physical Properties of Co-Evaporated CsPbI$_3$ Thin-Films

A series of CsPbI$_3$ thin-films was evaporated with different substrate temperatures. In-situ reflection measurements were performed during the deposition of the films to improve the understanding of the growth mechanism. The structural, compositional and morphological properties were studied depending on the substrate temperature during deposition and the chemical composition.

3.1 Sample Preparation Procedure and Appearance

For this study a series of four samples with different substrate temperatures was fabricated to study the influence of the substrate temperature on the film formation and final film properties. The deposition procedure for these films is described in Section 2.4. The substrate temperature was chosen to be T$_{\mathrm{sub}}$ = <35 °C, 50 °C, 65 °C and 80 °C, respectively. During the evaporation of the 35 °C sample the substrate heater remained switched off, which led to a gradually increase of the substrate temperature from 25 °C to 35 °C during the deposition due to the thermal radiation of the evaporation sources. This sample is hereafter being referred to as T_{sub} = 35 °C.

Despite an expected gradual gradient in the composition, all samples exhibit a dark brown and a bright yellow region, with a sharp boundary in between. Figure 3-1 shows a photographic image of a typical as-evaporated sample with T_{sub} = 50 °C and nominally stoichiometric evaporation rates of [CsI]/[PbI$_2$] = 1 as an example.
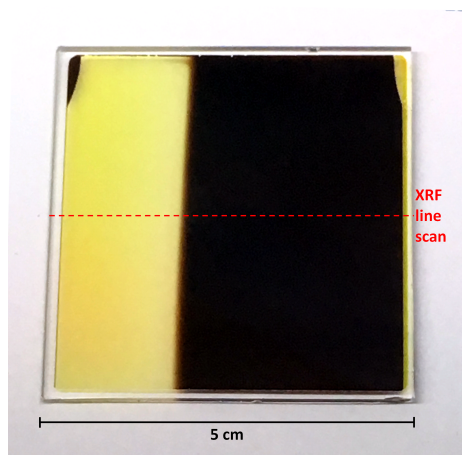
Figure 3-1: *Photographic image of an as evaporated sample with $T_{sub} = 50\,°C$ and nominally stoichiometric evaporation rates of [CsI]/[PbI$_2$] = 1. Two clearly distinct yellow and brown regions can be seen. The dashed red line marks the position of the XRF line scan.*

3.2 Elemental Composition

An XRF linescan was performed across the samples, perpendicular to the boundary between the yellow and brown region, to verify, if the lateral gradient of the chemical composition has formed as expected. The ratio of the cesium and lead contents is calculated, which were extracted from the XRF spectra as described in Figure 2.2. The result of these calculations for the four samples is shown in Figure 3-2. For easier comparison, the position on the sample is given relative to the boundary for each sample individually. The [Cs]/[Pb] atomic ratio increases almost linearly over a wide range of the substrate for all of the samples. Only at the cesium rich border of the samples a saturation of the ratio can be observed, possibly originating from inhomogeneous evaporation characteristics of one of the sources or unintentional shading effects.

The measurements show, that the atomic ratio of [Cs]/[Pb] at a given position relative to the boundary between the regions is independent of the substrate temperature. This means especially, that within the precision of this measurement, the point of stoichiometry occurs at the same relative position for all of the samples, which is close to the boundary.

For further verification, two more samples with $T_{sub} = 50\,°C$ were prepared. For these samples the ratio of the evaporation rate of the CsI and PbI$_2$ sources were varied independently to yield nominal compositions of [CsI]:[PbI$_2$] = 0.94:1 and 1.10:1, respectively. Photographic images of the three samples with $T_{sub} = 50\,°C$ are shown in Figure 3-3 along with the results of the XRF line scans for these samples.
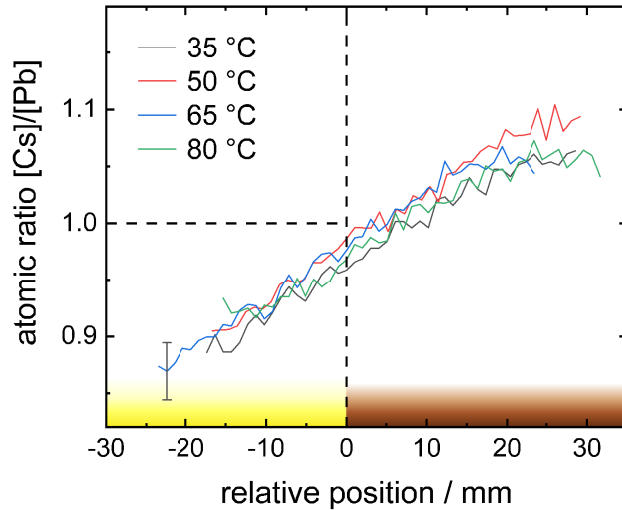
Figure 3-2: *Atomic ratio of [Cs]/[Pb] from XRF measurements as a function of lateral position on the samples relative to the observed boundary between the yellow and brown region. The ratio increases linearly over a wide range of the sample. The substrate temperature seems to have a negligible influence on the composition within the error of this method. The errorbar is representative for the error in the relative composition within the four measurements.*
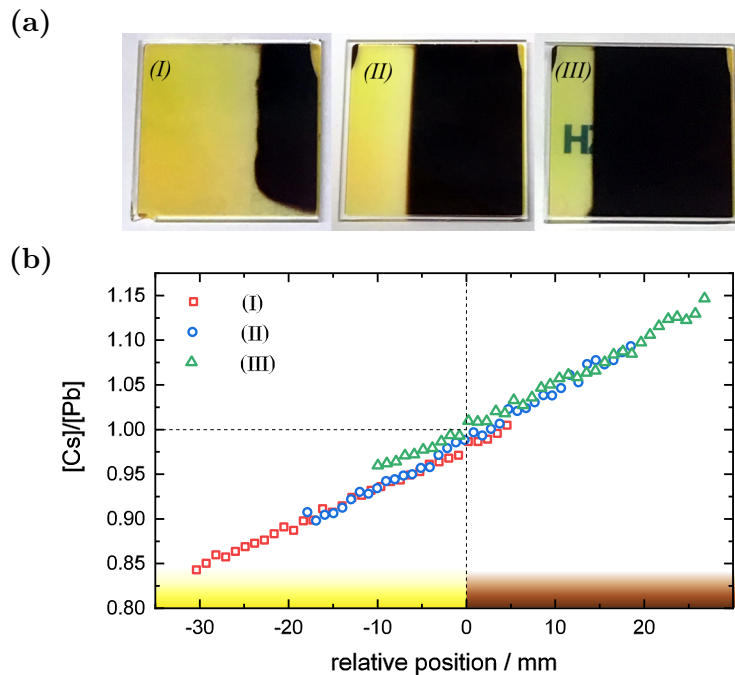
Figure 3-3: *(a) Photographic images of the three samples deposited with $T_{sub} = 50\,°\mathrm{C}$ with deposition rates [CsI]:[PbI$_2$] of (i)0.94:1 (ii)0.99:1 and (iii)1.10:1, respectively. (b) [Cs]/[Pb] atomic ratios from XRF measurements over the lateral sample position relative to the observed boundary between the yellow and brown region. For either of the three samples the boundary is located at the same compositional ratio.*

It is clearly visible, that the boundary between the yellow and brown region shifts in position, if the evaporation rates are changed. These results confirm, that the position of the boundary between the two regions always occurs at the same composition. For compositions with increased cesium content the sample looks brown, for a lead rich composition, the sample looks yellow. The almost linear nature of the position dependent chemical composition of the sample allow an easy estimation of the composition based on the relative position. Therefore, the results of all measurements reported in this work, which are acquired as a function relative lateral position on the sample can be translated into compositional dependent measurements.

Although the evaluation of the XRF measurements only quantifies the atomic ratio of cesium and lead, the composition is hereafter given as [CsI]/[PbI$_2$] ratio, as the evaporation of the precursors is assumed to occur congruently. To test this assumption, more precise measurements and evaluations have to be performed, to quantify the content of all three elements. Despite the verified gradient in the composition in the films, which would be correctly displayed by the chemical formula of Cs$_{1+x}$Pb$_{1-x}$I$_{3-x}$ according to the above mentioned assumption of congruent evaporation, the material will still be referred to as "CsPbI$_3$" for readability reasons.

3.3 Crystal Structure

To clarify the nature of the two regions, synchrotron based XRD measurements were performed as a line scan on the $T_{sub} = 50\,°\mathrm{C}$ sample. To exclude any influence from ambient air, the samples were transported and measured in the XRD-holder presented in Section 2.2 without any intermediate air exposure. For an easy comparison with measurements conducted at an XRD-instrument equipped with a copper X-ray tube, the monochromator of the beamline was set to match the copper K-α emission line at 8.048 keV. The diffraction signal was acquired by a 2D-detector and the images were processed as described in Section 2.2. The measurements were performed with fixed incident angle of $\omega = 5°$ and varying detection angle 2Θ. In contrast to the Bragg-Brentano geometry (so called Θ–2Θ geometry) the geometry applied here increases the contribution of lattice planes not being parallel to the surface, which is especially beneficial for textured samples (see Section 2.2). The results of the line scan are shown in Figure 3-4(a). A sharp transition between two distinctly different crystal structures can be seen at the same relative position, and therefore chemical composition, as the boundary between yellow and brown region of the sample. The appearance of a phase mixture in the two diffraction patterns next to the transition stems from the fact, that the interaction volume of the X-rays was overlapping the phase boundary. A comparison of patterns taken entirely in one of the regions with

(a)

(b)
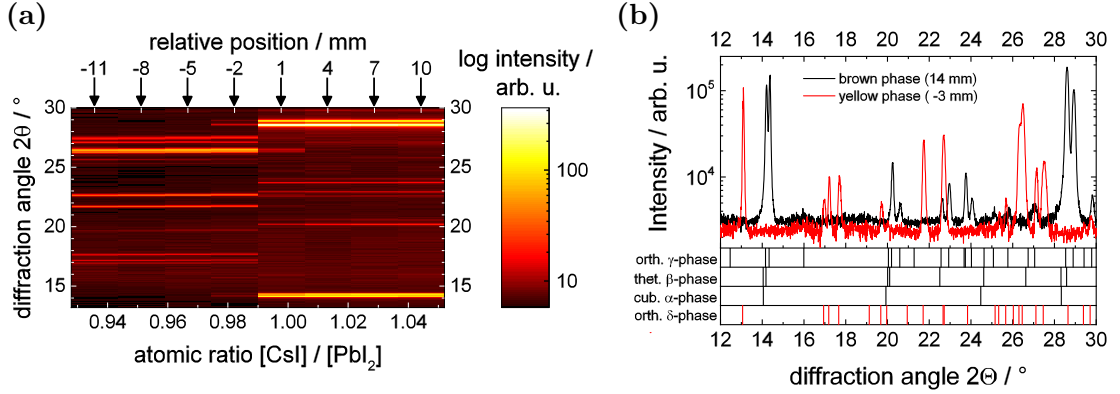
Figure 3-4: *(a) XRD patterns over the [CsI]/[PbI$_2$] atomic ratio from a line scan. The patterns were taken at the positions marked by the arrows. Two regions with clearly distinct crystal structure are visible. (b) Single XRD patterns extracted from the line scan where the interaction volume was completely in the brown (14 mm) and in the yellow region (-3 mm), respectively. Comparison with reflex positions from literature [69] reveal, that the yellow phase consist of δ-CsPbI$_3$ whereas the reflexes of the brown phase can only be fully explained by γ-CsPbI$_3$.*

reference patterns (see Figure 3-4(b)) reveals, that the yellow region consists of the CsPbI$_3$ δ-phase. The reflexes of the measurement in the brown region can only be fully explained by the distorted perovskite CsPbI$_3$ γ-phase, as described in Section 2.1, while the α- and β-phases can only explain some of the reflexes. Therefore, it can be concluded, that the brown part of the samples consists of the γ-CsPbI$_3$ phase. However, minor contributions of the α and β-phase can not be excluded due to the overlap of the peaks. This is in contrast to many reports in literature, which describe the brown CsPbI$_3$ phase at room temperature as the cubic non-distorted perovskite α-phase.[44, 64, 75, 80, 82, 112] It is, however, in agreement with more recent literature, which reports the orthorhombic brown γ-phase to be the (meta-)stable phase at room temperature.[69, 113] The meta-stability of the brown γ-phase will be discusses in Section 6 in more details.

Measurements that are taken farther away from the boundary between the phases start to show additional peaks which increase in intensity as the composition diverges from stoichiometry. Figure 3-5 shows examples for this effect, which hint towards the formation of secondary phases. Comparison with reference patterns [89, 114] reveal, that in the PbI$_2$-rich region the segregation is PbI$_2$ and the segregation in the CsI-rich region is CsI. No ternary phase besides the intended CsPbI$_3$ could be detected over the range of this measurement. Peaks from different lattice planes were fitted for the four components γ-CsPbI$_3$, δ-CsPbI$_3$, CsI and PbI$_2$ for all patterns of the line scan to determine the compositional dependent transition between the phases. The list of peaks used for this evaluation is shown in Table B-3. The evolution of the individually normalized intensities of the phases can be seen in Figure 3-6. As expected the phase transition between yellow

(a)

(b)
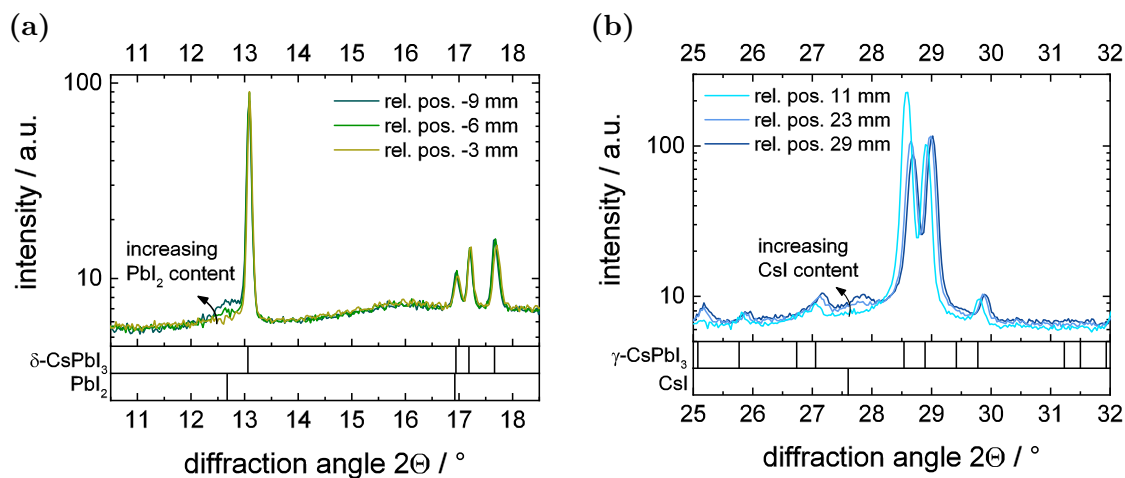
Figure 3-5: *XRD patterns showing the segregation of a secondary phase depending on the relative position, and thus composition, of the sample. (a) Segregation of PbI$_2$ in addition to the CsPbI$_3$ δ-phase. (b) Segregation of CsI in addition to the CsPbI$_3$ γ-phase. The shift towards larger angles between the three patterns originates form a slight misalignment of the sample during the line scan.*
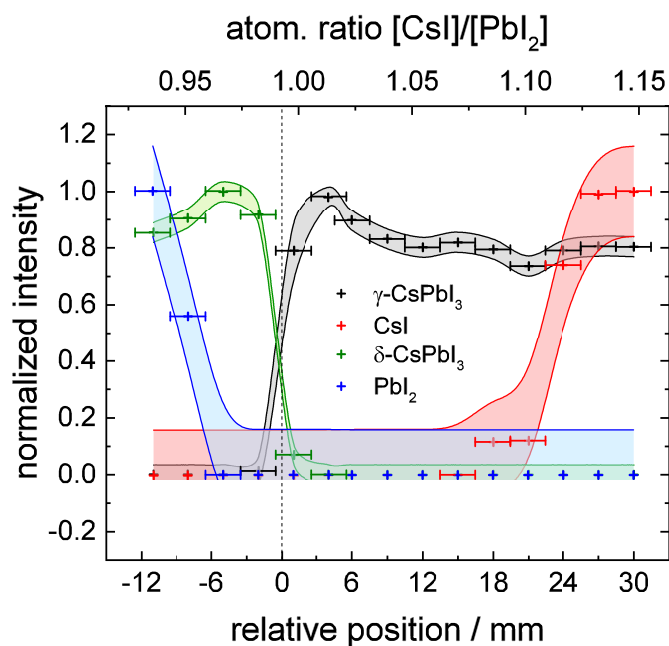
Figure 3-6: *Individually normalized intensity of the four phases γ-CsPbI$_3$, δ-CsPbI$_3$, CsI and PbI$_2$ as extracted from the XRD line scan. The intensities were obtained by integrating the area of several reflexes of the four components, respectively. To avoid influences from changing texture, reflexes from different lattice planes were averaged. The transition from δ-CsPbI$_3$ to γ-CsPbI$_3$ occurs at the position of the boundary between yellow and brown region as expected. PbI$_2$ and CsI segregation can be detected at [CsI]/[PbI$_2$] atomic ratios of $< 0.96 \pm 0.1$ and $> 1.07 \pm 0.1$, respectively.*

δ-CsPbI$_3$ and brown γ-CsPbI$_3$ occurs at the same position as the transition between the yellow and brown region. The segregation of PbI$_2$ and CsI can be detected for [CsI]/[PbI$_2$] atomic ratios $< 0.96 \pm 0.1$ and $> 1.07 \pm 0.1$, respectively. However, segregation of secondary phases with small volumes or non-crystalline segregations can not be excluded due to the limited sensitivity of this technique.

High resolution measurements for the samples with T$_{sub}$ = 35 °C, 50 °C, 65 °C and 80 °C, respectively, were performed at a dedicated XRD instrument to be able to determine the lattice parameters of the δ-CsPbI$_3$ to γ-CsPbI$_3$ phases by LeBail refinement as described in Section 2.2. The XRD-patterns for all samples on the brown γ-phase are depicted in Figure 3-7 with subtracted background. Since the measurements were acquired in the Θ-2Θ-geometry, information about the texturing of the sample can be gained from the different attenuation of reflexes from different lattice planes. The comparison of the four patterns reveals, that the texturing strongly depends on T$_{sub}$. While the pattern for the sample evaporated at T$_{sub}$ = 35 °C shows a very strong texturing, due to which almost no peaks can be seen aside from the two main double peaks at ~14° and 29°, the intensity of the reflexes in between those main reflexes increases with T$_{sub}$. As a result the intensity of the main peaks decreases simultaneously.
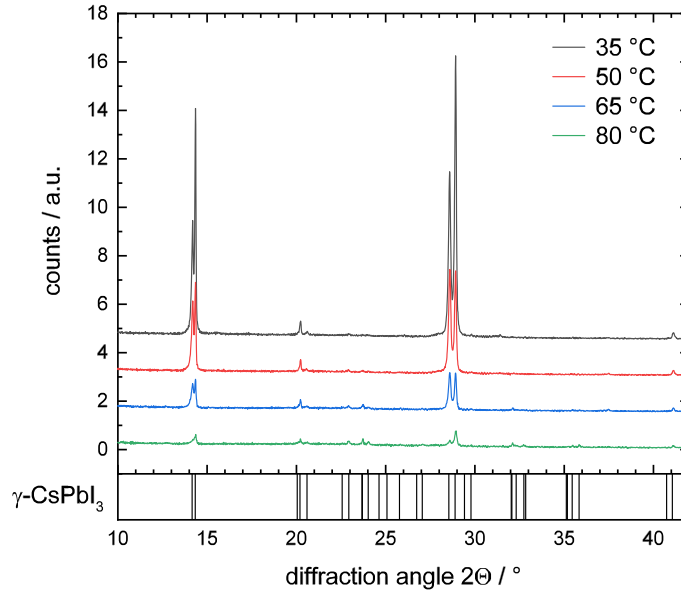
Figure 3-7: XRD patterns for measurements performed in the brown γ-phase region of samples with different T$_{sub}$. Since the measurements were performed in Θ-2Θ-geometry, the different texturing of the sample becomes apparent. The 35 °C sample reveals a strong texturing, which emphasizes the main double-reflexes at ~14° and 29° and attenuates almost all intermediate reflexes. With increasing T$_{sub}$ the influence of the texturing decreases, which can be seen in the decreasing intensity of the main reflexes and the weak rise of the remaining reflexes. All patterns were acquired with the same integration time and are merely shifted for the presentation.

LeBail-refinements were performed on all patterns of the brown γ-phase and the yellow δ-phase, to investigate, if T$_{sub}$ also influences the lattice parameters of the crystal structure. For the sample with T$_{sub} = 50\,°$C the results of these refinements are shown in Figure 3-8 as an example, along with the lattice parameters from the refinements. The refined reference patterns explain all major reflexes of the measurements reasonably well. The remaining residuals originate mostly from a non-optimal peak profile used for the modeling as well as minor peaks for the segregation of PbI$_2$ in the yellow region as well as CsI segregation in the brown region. Comparing the patterns taken at the synchrotron (see Figure 3-4(b)) in fixed-ω geometry and those taken in the laboratory in Bragg-Brentano geometry (in this work as well as in literature)[44, 83, 115, 116] it becomes evident, that most of the thin-film samples are highly textured. This leads to strong attenuation of specific reflections of the orthorhombic γ-phase in Bragg-Brentano geometry measurements, thus causing false identifications of the room temperature phase.

Similar refinements were performed for the patterns of the remaining three samples. The resulting lattice parameters of the more relevant γ-CsPbI$_3$ phase are listed in Table 3-2 along with values extracted from recent literature. It is worth noting, that some of the literature values were taken at elevated temperatures thus resulting in a lattice expansion. Therefore, for an easier comparison, the ratios of lattice constants a/b and $c/(a+b)$ are calculated, which can be seen as a measure for the different rotations of the octahedra. While the ratio of $c/(a+b)$ can be seen in the diffraction patterns by the degree of splitting of the two major double peaks at ~14° and 29° (002 and 110, and 004 and 220), a/b shows in the splitting of the minor peaks in between. Comparison of the ratios shows, that only
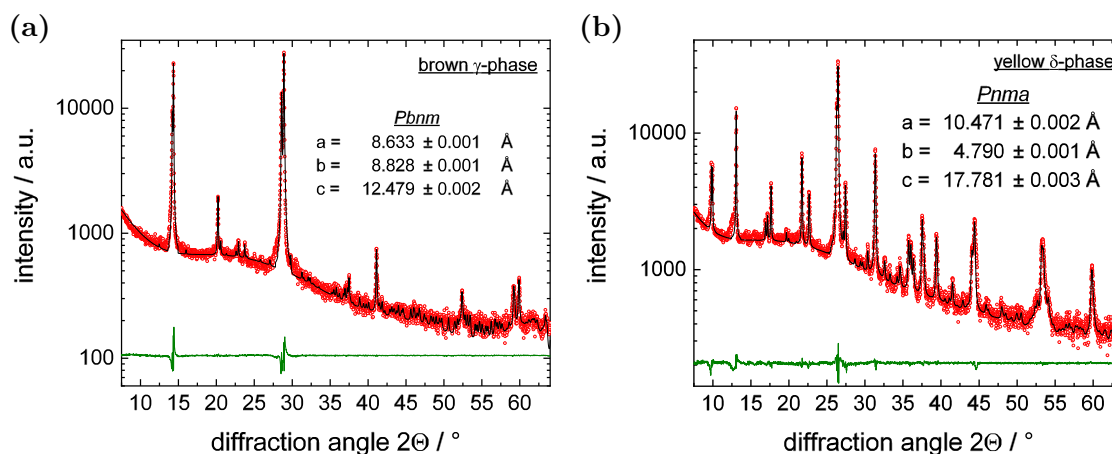
Figure 3-8: *XRD measurements on a T$_{sub} = 50\,°$C sample taken at a "PANalytical X'Pert Pro MPD" (a) in the brown part of the sample and (b) in the yellow part. The LeBail refinement (black) was performed with the software "PowderCell". The residuals (green) show that for both phases all major reflections can be explained.*

Table 3-2: *Lattice parameters for the orthorhombic Pbnm CsPbI$_3$ γ-phase obtained from LeBail re-finement of four samples with $T_{sub} = 35\,°C$, $50\,°C$, $65\,°C$ and $80\,°C$, respectively. To reduce the influence of lattice expansion due to increased temperature the ratios a/b and $c/(a+b)$ are calculated.*

	a / Å	b / Å	c / Å	a/b	c/(a+b)	V / Å^3	T / K
Marronnier[69]	8.620	8.852	12.501	0.9738	0.7155	953.9	325
Sutton[75]	8.577	8.856	12.472	0.9684	0.7154	947.3	293
Bertolotti NCs[113]	8.612	8.845	12.524	0.9737	0.7174	954.1	298
This work 35 °C	8.623	8.853	12.495	0.9741	0.7150	953.8	~298
This work 50 °C	8.633	8.828	12.479	0.9779	0.7147	951.0	~298
This work 65 °C	8.625	8.833	12.479	0.9764	0.7148	950.6	~298
This work 80 °C	8.622	8.827	12.479	0.9767	0.7152	949.7	~298

minor changes are found $c/(a + b)$, while a/b reveals more prominent variations. This indicates a difference in the degree of the distortion of perovskite structure by tilting of the octahedra against the plane.

As an additional result of the LeBail refinement, an estimation of the domain size can be extracted, which can be strongly correlated with the grain size, which again is an important parameter for the stability and formation of the different CsPbI$_3$ crystal phases as described in Section 2.1. The resulting domain sizes as extracted from the refinement of the four samples in the brown region are shown in Figure 3-9. All domain sizes are in the order of 100 nm with slightly increasing values for increasing T$_{sub}$. The value for the
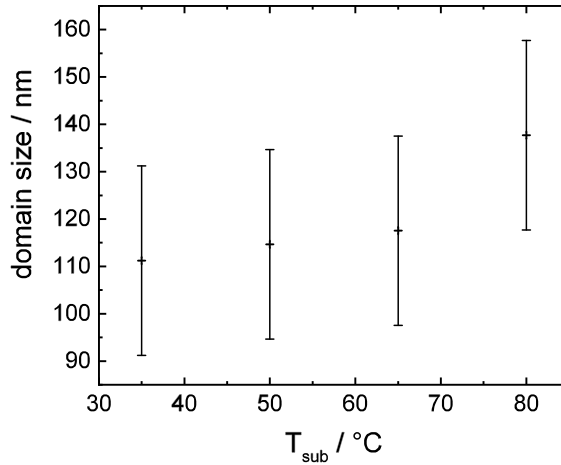
Figure 3-9: *Domain size extracted from LeBail fits of the XRD patterns depending on the substrate temperature (T_{sub}) during evaporation. A slight increase in the domain size with increasing T_{sub} can be seen. The sample with $T_{sub} = 80\,°C$ deviates from the trend of the other samples towards even higher domain sizes.*

T$_{sub}$ = 80 °C sample slightly deviates from the trend towards even larger domain sizes. For the measurements in the yellow δ-phase domain sizes of 165 nm to 200 nm are obtained from the fit, which is higher than the maximum detectable domain size for the given setup, which is estimated from the known instrumental resolution with the Scherrer equation to be around 150 nm.[117]

With the domain sizes of the γ-phase trending towards the limits of the detection and the values for the δ-phase even exceeding that limit, more detailed investigation of the size are required to gain reliable information about the grain growth conditions.

3.4 Surface Morphology

The morphology of the films was investigated by SEM to bring more insight into the influence of T$_{sub}$ and the chemical composition on the grain size. Although the XRF data reveal, that the chemical composition of the sample increases gradually, the crystal structure of the sample seems to change abruptly at a given composition. SEM images will reveal, if this abrupt change in crystal structure correlates with a change in the morphology.

To minimize the exposure to ambient conditions the samples were prepared for the measurements within a glove box and sealed in a transport bag. The transfer time from the transport bag into the SEM specimen chamber was kept as short as possible and was around 3 s. Only little changes in color of the samples were observed after the transfer. To furthermore minimize damage by the electron beam, a low acceleration voltage of 2 keV was used for the measurements.

Images were taken on a line parallel to the chemical gradient in 5 mm steps for each of the four samples with different T$_{sub}$ to investigate the influence of the composition as well as of the substrate temperature on the morphology of the samples. The images taken with magnifications of 10k and 75k are shown in Figure 3-10 and Figure 3-11, respectively.

The images with 10k magnification are taken with the InLens-detector and show flat surfaces over the entire compositional range for all the samples. Three single intermediate images for the sample with T$_{sub}$ = 65 °C show an exceptionally rough surface, which might be caused by an uneven substrate or dust particles attached to the substrate before film deposition.

A clear difference in the morphology in the CsI-rich and the PbI$_2$ part of the sample is visible. In the PbI$_2$-rich part a patchy pattern with domains in the µm regime is visible. The different brightness of the single domains hints towards differently oriented crystallites. In the CsI-rich part, however, white spots can be found on a dark background, with the
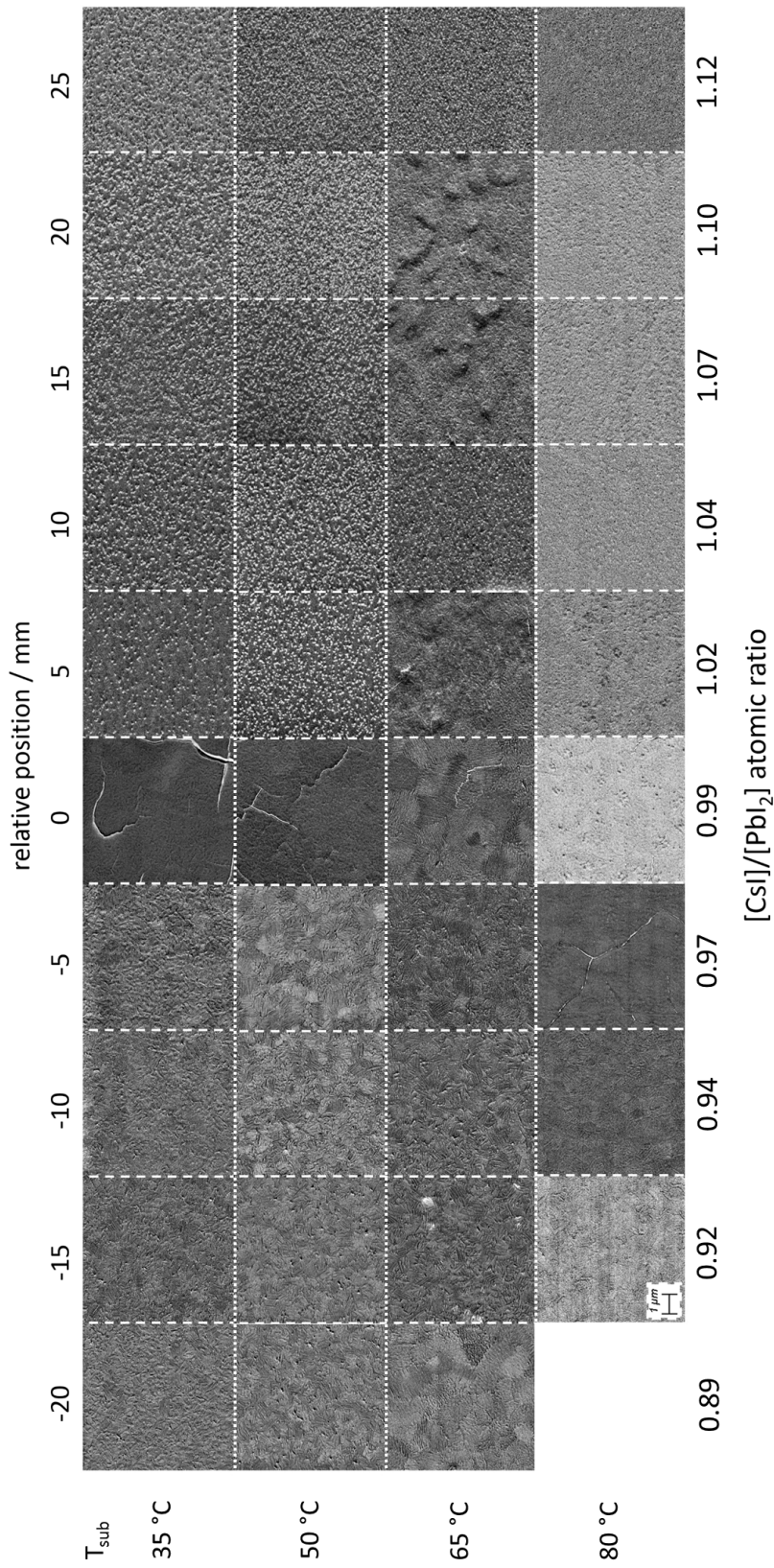
Figure 3-10: *SEM images taken with the 'InLens-Detector' on four samples with different T_{sub} and position on the sample relative to the boundary between brown γ and yellow δ-phase. The composition stated in the bottom is estimated from XRF data (see Figure 3-2). In the CsI-rich part of the sample, bright spots with diameters in the order of $100\,\mathrm{nm}$ appear, hinting towards a charging material. In the PbI$_2$-rich part a patchy pattern can be observed, which might originate from differently oriented grains.*
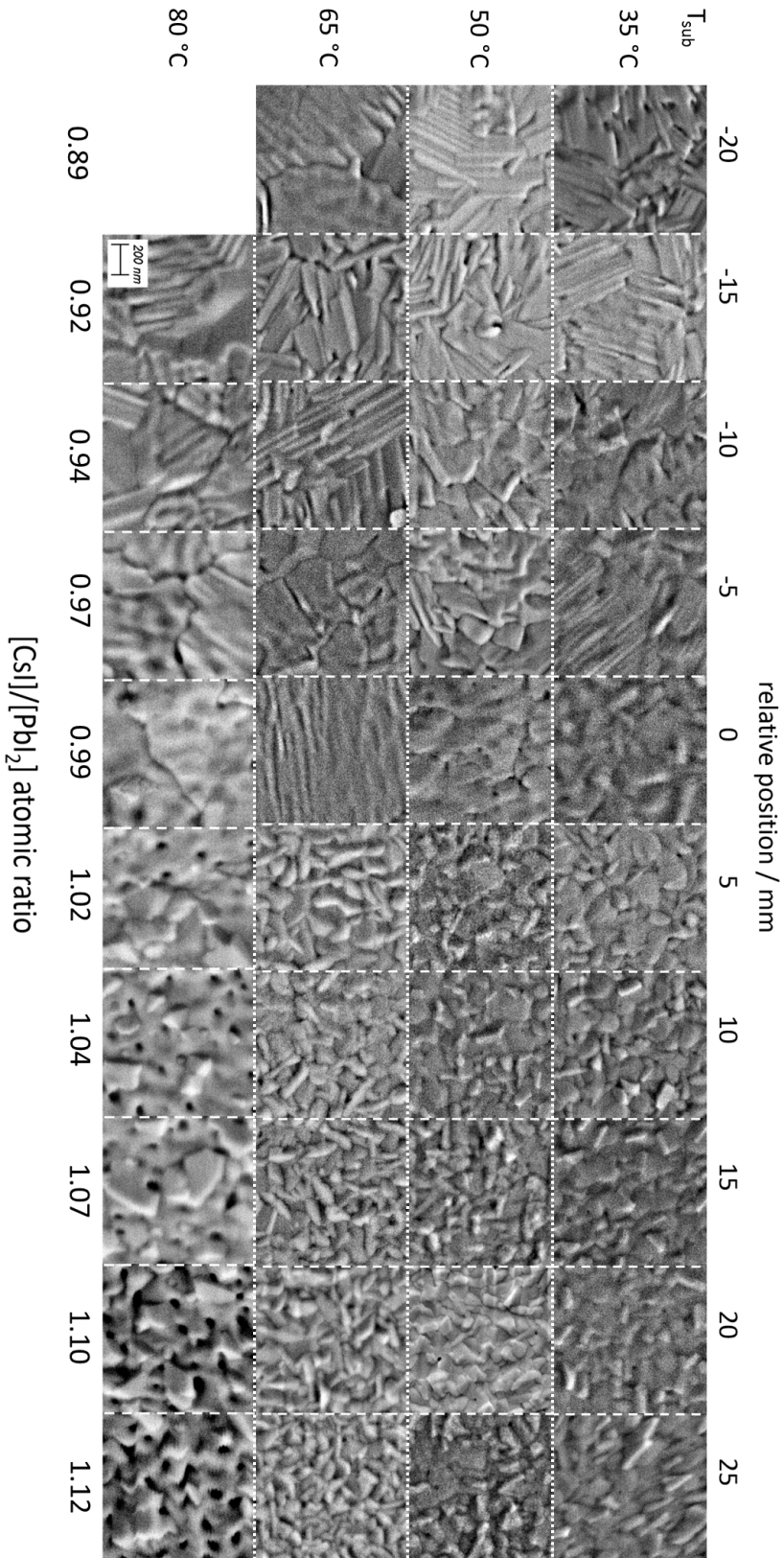
Figure 3-11: *SEM images taken with the 'SE2-Detector' on four samples with different T$_{sub}$ and position on the sample relative to the boundary between brown γ and yellow δ-phase. The compositions stated in the bottom are estimated from XRF data (see Figure 3-2). The grain sizes in the CsI-rich brown γ-phase are in the order of 100 nm, while grains in the PbI$_2$-rich yellow δ-phase are significantly larger and in the order of 1 μm. Samples deposited at T$_{sub}$ = 35 °C, 50 °C and 65 °C, respectively, show closed films over the entire sample, in contrast to the sample deposited at 80 °C, which exhibits holes in the structure in the γ-phase. As the PbI$_2$ excess increases, more and more needled structures appear.*

density of the white spots increasing with increasing CsI excess in the composition. This might indicate the segregation of a secondary phase of CsI, which exhibits an exceptionally high band gap of 6.4 eV and thus act as an insulator, which is electrically charged by the electron beam.Images at the same position taken with the SE2-detector reveal, that the bright spots are incorporated within the film and not positioned on the top of the surface.

At higher magnification of 75k the differences between the CsI-rich and the PbI$_2$-rich part become more clear. While the grain sizes in the CsI-rich part range in the order of 100 nm, grains in the PbI$_2$-rich part are significantly larger and even in the µm range. In all four samples the grains in the PbI$_2$-rich part develop more and more needle shaped structures with increasing PbI$_2$ excess, as known from the mixed organic-inorganic per-ovskites.[118–120] In the CsI-rich part, the samples with $T_{sub} = 35\,°C$, $50\,°C$ and $65\,°C$ show distinct grains. Only in the sample with $T_{sub} = 65\,°C$ a few holes in the layer are visible. The sample with $T_{sub} = 80\,°C$ shows many holes, while the grains appear molten and smeared out. To investigate the change of the grain size in the CsI-rich part, an automated grain analysis was applied to the images. The resulting grain sizes can be seen in Figure 3-12. While the grain size for all four samples gradually decreases with increasing CsI-content, the grain sizes for the three samples with $T_{sub} = 35\,°C$, $50\,°C$ and $65\,°C$ are similar and around $\sim$100 nm. The grain sizes for the $T_{sub} = 80\,°C$ sample, however, are slightly larger and around 150 nm. This is in very good agreement with the results
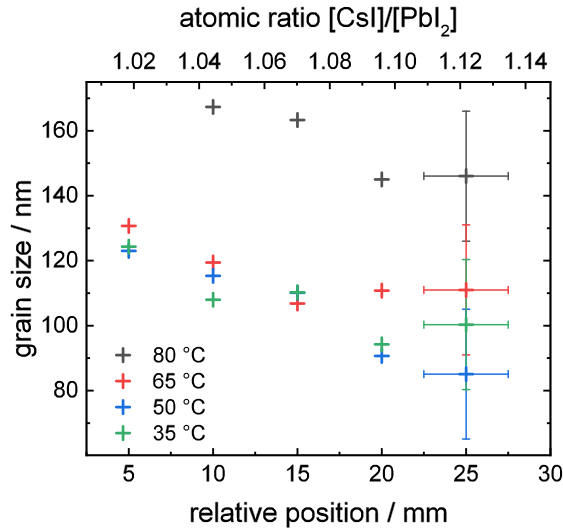
Figure 3-12: *Grain sizes in the CsI-rich part of four samples with different T_{sub} as extracted from grain analysis of SEM images as shown in Figure 3-11. The errorbars marked at the single data points are representative for the error of all points in the plot. A general trend shows that the grain sizes decrease with increase CsI excess. While the grain sizes of the samples with $T_{sub} = 35\,°C$, $50\,°C$ and $65\,°C$, respectively, show similar grain sizes of $\sim$100 nm the grains of the $T_{sub} = 80\,°C$ sample are larger with $\sim$150 nm.*

from the domain size analysis from LeBail refinements on the XRD patterns as shown in Figure 3-9.

Concluding the results from the SEM and XRD measurements, the hypothesis is formed, that that excess CsI can not or only in very small amounts be incorporated into the perovskite structure and thus forms a secondary phase. It can however not be concluded, if this secondary phase consists of pure CsI or rather a mixture of CsI and the CsI-rich ternary component such as Cs$_4$PbI$_6$. The presence of excess CsI in the integral chemical composition also seems to hinder the grain growth and thus result in CsPbI$_3$ grains with drastically reduced sizes in the order of $100\,\mathrm{nm}$ as opposed to grains in the µm range as found in the region with no CsI excess but PbI$_2$ excess.

As described in Section 2.1 the stability of the brown γ-phase, and thus the capability to form the phase, depends on the grain size. While the brown γ-phase exhibits a lower Gibbs free surface energy as the δ-phase, the Gibbs free bulk energy is lower for the δ-phase. Thus, the energetically favored phase is determined by the ratio of the bulk and surface of a crystallite. Therefore, the small grains in the CsI-rich part of the film exhibit the brown γ-phase, while the significantly larger particles in the PbI$_2$-rich part form in the yellow δ-phase.

3.5 In-Situ Monitoring of Optical Properties During the Deposition

To investigate the formation of the two phases during the evaporation of the films in more detail, in-situ measurements were performed during the deposition. For this, the white light optical reflection (WLR) of the films in the visible and infrared region was monitored spectrally as well as spatially resolved, as described in Section 2.3. It was shown, that in-situ spectral WLR can be a valuable method to monitor and optimize the growth of thin-films.[108] As the films described in this work exhibit a gradient in composition, the spectral WLR has to be limited to a well defined, small spot on the sample, in which the composition of the film is estimated to be very similar, thus only giving information about the formation for this composition. In addition the reflection is continuously recorded by a camera as complementary method, which yields spatially, and thus compositionally, resolved reflection data, however, with only limited spectral information.

In this work, the interpretation of the reflection data will focus on to the information required for the investigation of the formation of the different phases. A detailed description and interpretation of the optical properties of the films will be given in Section 4.1.

Figure 3-13 shows single images, which represent the evolution of the reflection for different times during the deposition, using the $T_{\mathrm{sub}} = 50\,°\mathrm{C}$ sample as an example. Two

artifacts are visible in the reflection images. One is the narrow horizontal bright lines which originate from reflection on the edges of the four substrate stripes. The other one is a brought vertical stripe in the center of the substrates, which originates from the direct reflection on the rough surface of the substrate heater, which can be seen through the substrates.

As can be seen in the image taken 10 min after the start of the deposition, the film initially forms in a brownish color over the entire substrate and thus over the entire compositional range. Only starting from the image at 20 min a separation of a brighter and a darker area can be observed, which leads to the two clearly distinct regions as known from the completed deposition (see Section 3.1).

This change in color can be quantified by the intensity of the reflection in the imaging. Figure 3-14 shows the normalized intensity, which was integrated over the area marked with the red circle in Figure 3-13, which undergoes the transition from brown to yellow during the evaporation. Strong fringes from thin-film interference can be seen in the evolution of the reflection intensity, indicating a smooth surface throughout the deposition process.
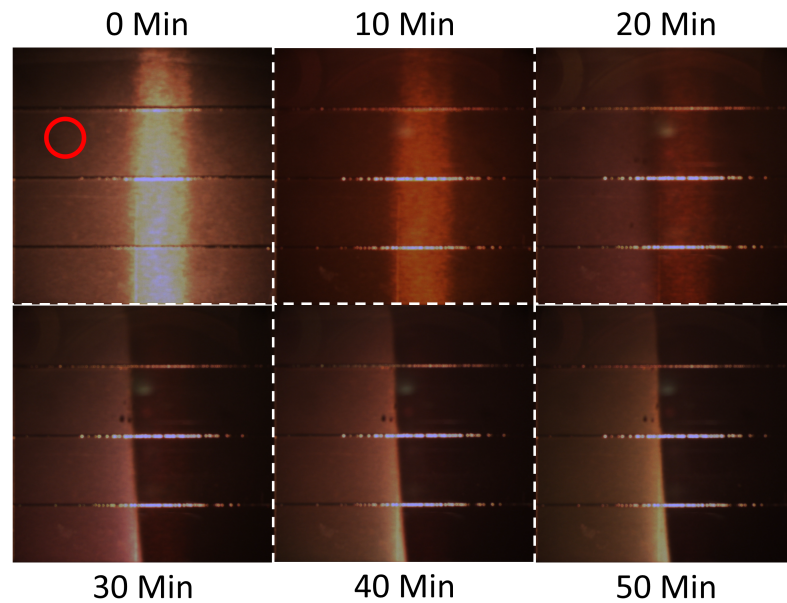
Figure 3-13: *Evolution of the reflection imaging during the evaporation for different intermediate times. The red circle marks the area which is monitored by the spectrally resolved WLR. The narrow horizontal bright stripes are direct reflections on the edges of the four substrate stripes, whereas the broad vertical bright stripe in the center of the substrates originates from a direct reflection on the rough surface of the substrate heater, which can be seen through the the substrates. The film initially forms entirely brown (10 min) before it turns yellow in the PbI$_2$-rich part, while the CsI-rich part remains brown.*
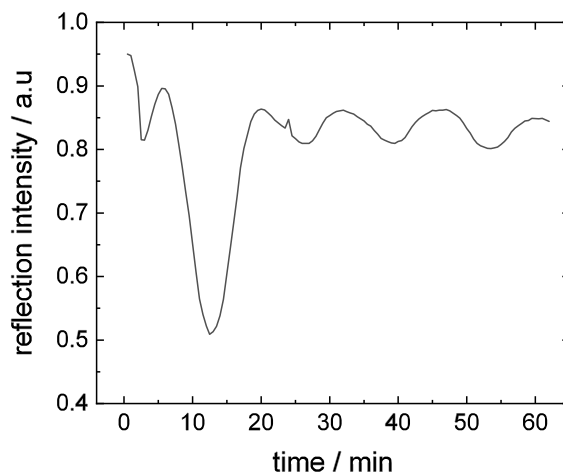
Figure 3-14: *Normalized intensity of the reflection as extracted from the reflection imaging in the position marked with the red circle in Figure 3-13. The trend in the intensity over time is superpositioned with fringes from thin-film interference. A rapid decrease of the intensity can be seen as the brown γ-phase forms. At ~12 min the transition towards the yellow δ-phase starts, which can be seen by a steep increase in the intensity, before it remains almost constant asides from the interference fringes.*

The trend in the intensity without the interference shows a rapidly decreases until ~12 min, indicating the growth of a brown layer with increasing thickness. After this point in time, the intensity shows a steep increase, before it remains almost constant for the rest of the process, which is an indication for the beginning of the transformation from the brown γ-phase towards the yellow δ-phase.

For more detailed and precise analysis of this transition, spectrally resolved WLR was applied in this area. Since this area is not in the center of the film and thus not on the optical axis, defined by the light source and the collimating mirror, which collects the reflected light, the measurement contains contributions from direct as well as diffuse reflection. This complicates a proper normalization and numerical evaluation of the data, while it does not significantly affect the observation of the phase transition during the evaporation.

Spectra of the WLR are recorded every 30 s. For easier understanding of the data Figure 3-15 shows seven separate spectra, to illustrate characteristic states of the evaporation. The entire data set for WLR measurements on evaporation runs with $T_{sub} = 35\,°C$, $50\,°C$, $65\,°C$ and $80\,°C$, respectively, is shown in Figure 3-16. In the beginning of the evaporation (Figure 3-15(a)) an absorption edge forms at ~710 nm, which is around the band gap of the γ-CsPbI$_3$ phase as known from literature (see Table 2-1). This confirms the suggestion from the reflection imaging, that the brown γ-phase forms on the entire substrate in the the early stage of the evaporation. Interestingly, a bump in the reflection

(a)

(b)
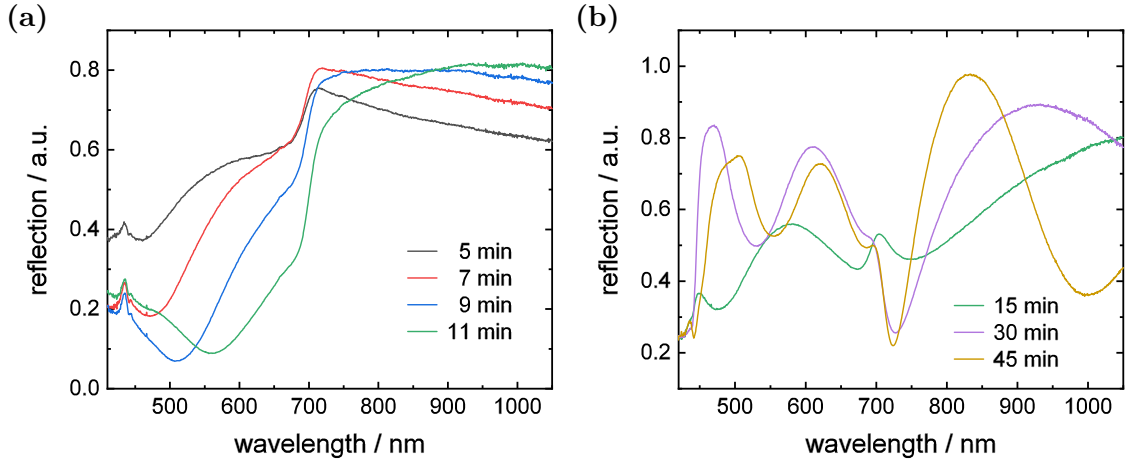
Figure 3-15: *WLR spectra taken at different times during the evaporation with $T_{sub} = 50\,°C$ (a) while the entire film is still brown and (b) in the yellow part, after the yellow and brown region separated. In both cases, absorption edges are visible for both, the brown γ-phase at ~710 nm and the yellow δ-phase at ~430 nm, as well as thin-film interference fringes at energies below the respective edges.*

is visible at ~430 nm in these early reflection spectra as well, being around the band gap of δ-CsPbI₃. Thin-film interference fringes for wavelengths above that bump support the hypothesis, that in the first minute of the evaporation, before the formation of the brown γ-phase, a very thin layer of yellow δ-CsPbI₃ forms. Evaluation of single spectra reveal, that an absorption edge at ~430 nm is visible in the first spectra already, while the rise of the absorption edge for the brown γ-phase start at ~1.5 min, resulting in an estimated thickness of the δ-phase layer of $(10 \pm 5)\,$nm. UV-Vis measurement on final films after full evaporation support this hypothesis, as described in Section 4.1.

In the WLR spectra taken at later times of the evaporation, as shown in Figure 3-15(b), the rise of a much stronger absorption edge at ~430 nm can be observed. The interference fringes for wavelengths above this edge increase in intensity. In contradiction to the observations from the reflection imaging, the absorption edge at ~710 nm for the γ-phase does not vanish completely. The interference fringes above this edge even increase in amplitude. Comparison with UV-Vis data for films with completed evaporation do not show this second absorption edge (see Section 4.1). This suggests, that the appearance of this edge is an artifact of this measurement. Since it is necessary for the simultaneously recorded reflection imaging to illuminate the entire sample, it seems likely that reflected light from different, still brown parts of the sample is falsely collected by the collimating mirror, thus creating the artifact of the second absorption edge.

A more complete picture about the processes during the evaporation can be gained from looking at the entire data set of the WLR spectra as depicted in Figure 3-16. The

two absorption edges at ~710 nm and ~430 nm, which were described above, form in all processes. No significant differences between the wavelength of the edges can be seen. The fringes from thin-film interference are clearly visible for all of the samples. The similarity in the number and shift of the interference fringes above 710 nm in between the samples suggests, that the films grew with similar optical properties as well as similar rate and thickness during these processes. Measurements with different numbers of interference fringes were observed during other evaporation processes, indicating issues with the quartz crystal balances, which control the evaporation rates. Another indicator for a deviation from the expected evaporation procedure can be seen in the measurement for the T$_{sub}$ = 65 °C sample. The edge of the absorption onset at ~430 nm only appears with much lower intensity, as compared to the other processes, while no obvious difference can be observed from reflection imaging. The reason for the deviation for this process might be the formation of a film with increased surface roughness. The SEM images in Figure 3-10
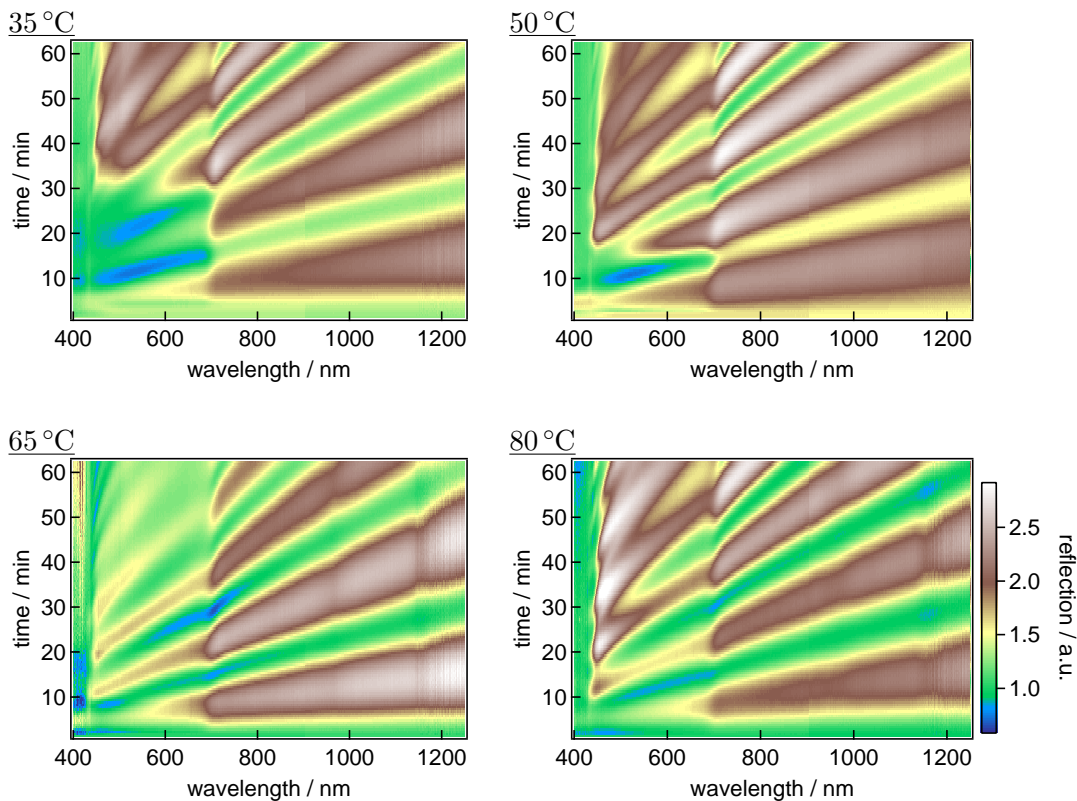
Figure 3-16: *Evolution of WLR spectra during the deposition with different substrate temperatures of T$_{sub}$ = 35 °C, 50 °C, 65 °C and 80 °C. In the beginning of the evaporation a strong absorption edge at ~710 nm forms, while a second absorption edge at ~430 nm forms later, at different times depending on the substrate temperature. Distinct interference fringes can be seen for wavelengths larger than these edges, which shift to higher wavelengths, as the thickness of the films increase with time.*

show an increased roughness for this sample within the brown region. However, it is not unlikely, that an increased roughness can be observed in different positions within the yellow region, which were not investigated by SEM.

Further comparison in between the different measurement in Figure 3-16 reveal, that the time of transition from the brown to the yellow phase varies with the substrate temperature. Following the conclusion from Section 3.4 that the formation of the phases depends on the grain size, it can be hypothesized, that in the beginning of the evaporation the size of the domains is sufficiently small, so that the lower surface free energy still dominates the phase formation. As the grains grow with progressing evaporation, and dependent on the substrate temperature, the influence of the bulk free energy increases and, at some point, dominates over the surface free energy, thus changing the crystallographic phase.

To test this hypothesis, interrupted depositions with $T_{sub} = 50\,°C$ were performed, in which the evaporation was stopped after $5\,min$ and $9\,min$, with the entire sample still being brown. SEM images were taken for the two samples and are shown in Figure 3-17. The images reveal, that the formation of a closed layer is not completed after $5\,min$ nor after $9\,min$. Both films exhibit holes in the Cs-rich region of the sample. However, both samples
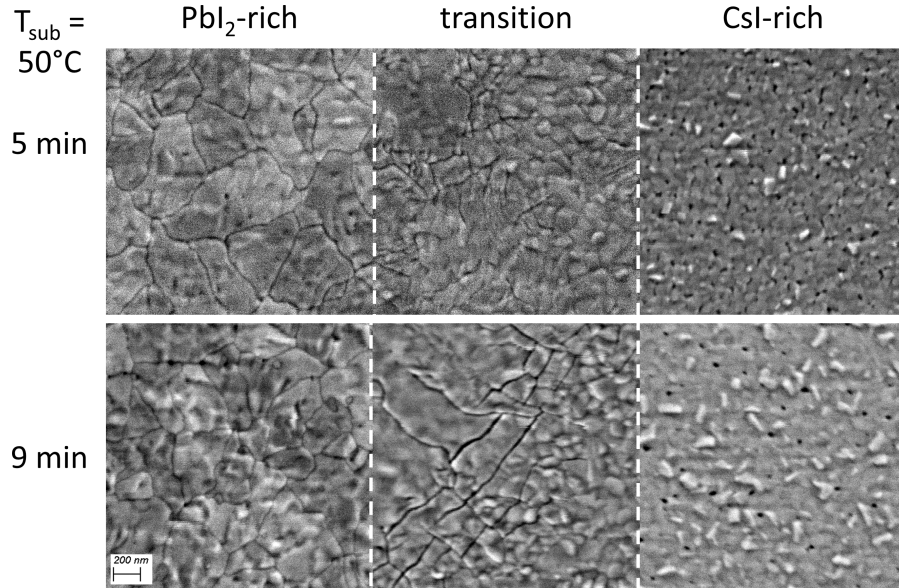
Figure 3-17: *SEM images of two samples evaporated at $T_{sub} = 50\,°C$ with interrupted deposition after $5\,min$ and $9\,min$, respectively. The images were taken in the PbI$_2$-rich part, in the CsI-rich part and at the boundary between the two regions, respectively. The grain sizes in the two off-stoichiometric regions are similar to those in the sample with completed evaporation (see Figure 3-11). At the transition point the grain size changes abruptly in between neighboring grains. After $5\,min$ the layer is not completely formed and shows numerous holes. The number of holes is significantly decreased after $9\,min$.*

reveal very similar grain sizes as compared to the samples with completed deposition. While grain sizes in the Cs-rich part are in the order of 100 nm, grains in the PbI$_2$-rich region are in the order of several 100 nm. At the transition point between the phases an abrupt change in grain size even between neighboring grains can be observed, supporting the hypothesis, that any excess of CsI in the chemical composition inhibits the grain growth. The similarity in the grain sizes as compared to completed films, however, is in contrast to the hypothesis, that at early stages of the evaporation small grains with large surfaces form, that cause the brown γ-phase to be dominant.

The rejection of this hypothesis is supported by the in-situ WLR-spectroscopy measurements performed during the interrupted depositions. After the evaporation was stopped by closing the substrate shutter and switching off the substrate heater, the shutters of the evaporation sources were closed as well. Subsequently, the substrate shutter was opened again to allow continued WLR measurements without further evaporation. The measurement for the evaporation process, which was interrupted after 9 min, is shown in Figure 3-18. Similar to the WLR measurement for the completed evaporation as shown in Figure 3-16, the evaporation starts with the rise of an absorption edge at ~700 nm for the brown phase. The stop of the evaporation after 9 minutes by closing the substrate shutter, can be seen by the blue line in Figure 3-18(a). After the shutter is opened again, an absorption edge at ~420 nm starts to grow at 42 min after the start of the evaporation. This is around the same time, as the beginning of the transition for the evaporation with $T_{sub} = 35\,°C$. The constant interference fringes in the near infrared region prove, that the thickness of the layer does not increase any further, after the deposition was stopped.

(a)   **(b)**
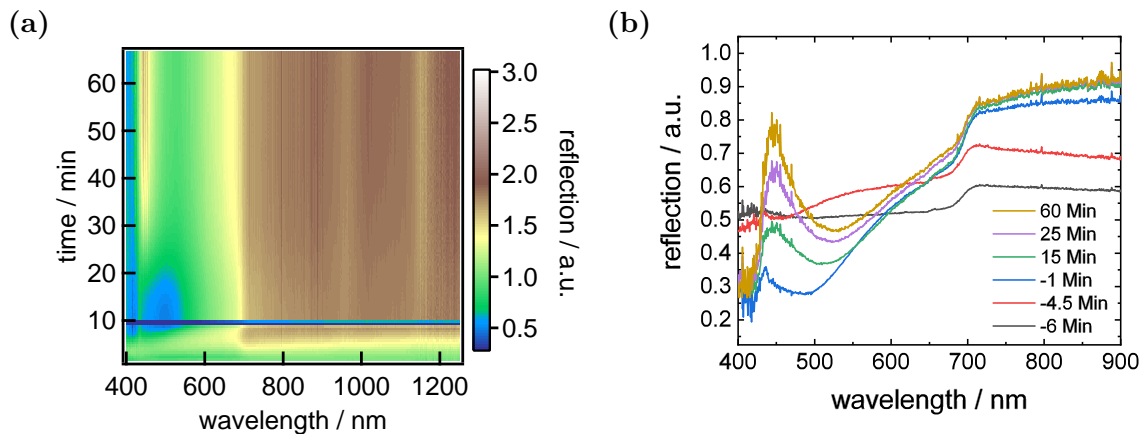
Figure 3-18: *Spectral WLR of an evaporation process, which was interrupted after* 9 min *(a) as a function of time (b) single spectra, extracted from the continuous scan. Before the evaporation was stopped, the formation of the brown phase with absorption edge of ~700 nm can be observed. After the source shutters were closed, a slow rise of and absorption edge at ~420 nm can be observed.*

This observation suggests, that the changing crystal structure is not an effect of growing grains, but rather a thermally activated process. To investigate this in detail, the substrate temperatures and transition times are read from the evolution of the WLR spectra shown in Figure 3-16 as well as from three more processes with the same substrate temperatures. The times are entered into an Arrhenius plot, for further evidence of a thermally activated process. The plot with a linear fit to the data is shown in Figure 3-19. The fit describes the data reasonably well, which strengthens the hypothesis of a thermally activated process.

The activation energy extracted from the fit is $(4.0 \pm 0.2) \cdot 10^4$ J/mol. Extrapolation of the fit to room temperature (20 °C) results in a transition time of 56 minutes, which is in an order of magnitude, that would allow most of the characterization methods presented in this work. Thus evaporation runs at substrate temperatures below room temperature might allow to gain insight into the properties of a PbI$_2$-rich, large grain size γ-phase.

The measurements of the as-deposited films reveal, that despite the linear gradient in composition, two distinctly different regions form in the film. The composition of the film at the boundary between the regions is [CsI]/[PbI$_2$] $= 0.99 \pm 0.02$. SEM images reveal, that the compositional excess of CsI results in small grains of ~100 nm, while grains with PbI$_2$ excess are significantly larger and in the order of 1 µm. Compositional dependent XRD measurements revealed, that in the CsI-rich region the brown γ-CsPbI$_3$ was formed with small amounts of CsI-segregation. These segregations could be found in the SEM-measurements as bright dots in the InLens-images. The crystal structure of the PbI$_2$-rich region of the sample was shown to be the yellow δ-CsPbI$_3$.
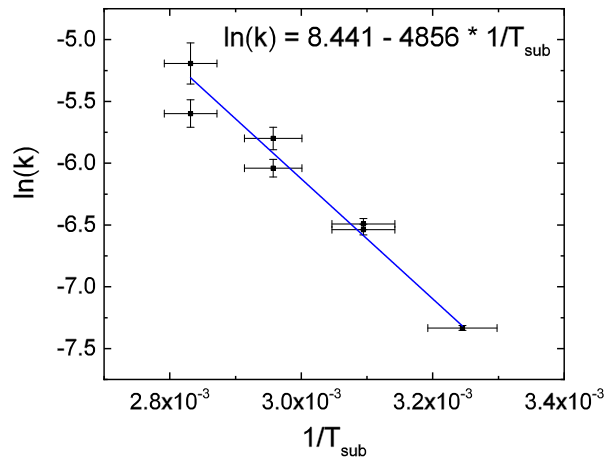
Figure 3-19: *Arhenius plot for the transition of the brown γ-phase to the yellow δ-phase during the evaporation dependent on T_{sub}. The times for the transitions were obtained from WLR-spectroscopy. From the linear fit to the data an activation energy of the transition process of* $(4.0 \pm 0.2) \cdot 10^4$ J/mol $= (2.49 \pm 0.12) \cdot 10^{23}$ eV/mol *is calculated.*

In-situ optical reflection measurements revealed, that initially the brown γ-phase forms over the entire substrate. However, the large-grained PbI$_2$-rich part transforms to the yellow δ-phase in a thermally activated process during the deposition. In addition, indications for $\sim(10 \pm 5)$ nm thick layer of the yellow δ-phase could be found, which forms between the substrate and the actual brown γ-phase layer.

4

Optoelectronic Properties of As-Deposited Films

For the application of the evaporated thin-films in photovoltaic devices, the optoelectronic properties of the material play a major role. The films described above feature a gradient in chemical composition and are evaporated at different substrate temperatures $T_{sub} = 35\,°C$, $50\,°C$, $65\,°C$ and $80\,°C$. Therefore, they give valuable information about the influence of these parameters on the optoelectronic properties. For a most complete picture of these dependencies, the measurement techniques were applied spatially resolved on all the four samples, where possible.

4.1 Optical Properties

UV-Vis measurements were performed on the as-evaporated films, to access information about the absorption coefficient and the band gap. Since the chemical composition is expected to influence these quantities, the measurements were performed in a line scan across the sample along the compositional gradient. The measurements were performed in the inert atmosphere of a glove box with the setup described in Figure 2.2 to protect the films from the influence of oxygen and humidity. The step size was chosen to be $1\,mm$ to be able to resolve fine variations. For easier understanding of the results of the line scan, Figure 4-1 shows two single measurements of a sample, evaporated at $T_{sub} = 65\,°C$, one taken in the brown region, one in the yellow region. The measurement of the yellow δ-phase was taken at a position of $-4\,mm$ relative to the boundary between brown and yellow phase, whereas the measurement of the brown γ-phase was taken at a relative position of $4\,mm$. Both transmission measurements show a low transmission at low wave-
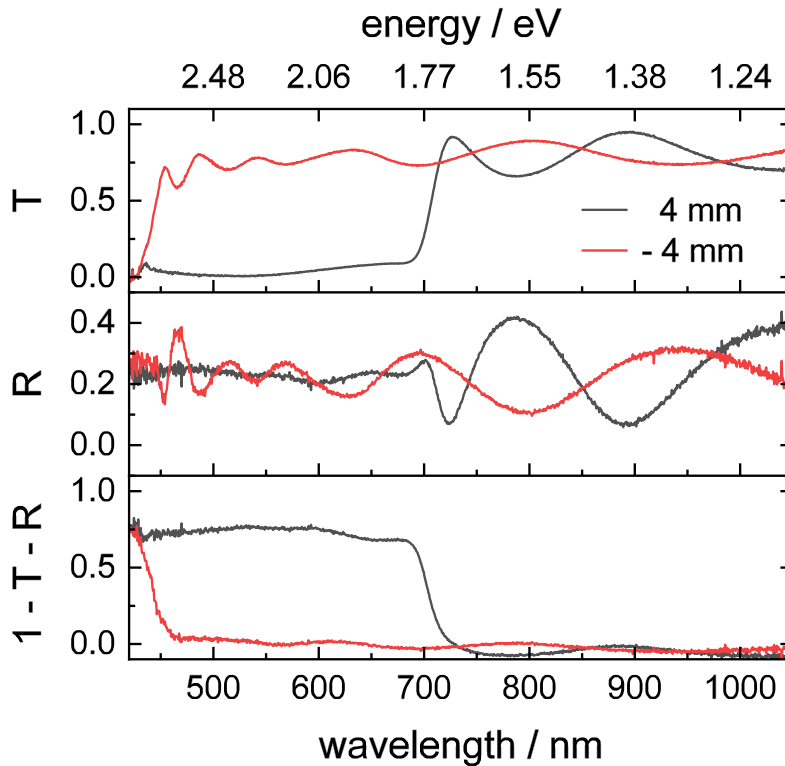
Figure 4-1: *Single spectra for transmission (T), reflection (R) and absorption (1-T-R) measured by UV-Vis spectroscopy in the brown region (black line) and yellow region (red line) of a $T_{sub} = 65\,°\text{C}$ sample, respectively. In the yellow region, an absorption onset at $\sim 430\,\text{nm}$ with interference fringes for higher wavelengths is visible. In the brown region, an absorption edge at $\sim 710\,\text{nm}$ with strong thin-film interference fringes can be seen. Another, much weaker feature is visible at the same wavelength as the absorption edge of the yellow phase.*

lengths, which increases towards higher wavelengths. While the transmission in the brown region increases steeply at ~710 nm, the transmission in the yellow region shows a slightly shallower increase at ~430 nm. Both transmission signals show very prominent thin-film interference fringes as already observed in the in-situ reflection (see Section 3.5), which indicates a low roughness. On a closer look, a very weak secondary absorption edge can be seen in the measurement of the brown phase at the approximate position of the absorption edge of the yellow phase, supporting the observation of a secondary absorption onset in the in-situ reflection. The reflection signal for both positions is around 20 %, revealing the same interference fringes as seen in the transmission. The onset of the fringes coincides with the step in the transmission.

In the calculated absorption signal the absorption edges seen in the transmission are even more pronounced. Absorption values slightly below zero as well as weak remains of the interference fringes are visible. These might be caused by minor errors in the reference

measurements and a slight mismatch between reflection and transmission measurement. The secondary absorption onset in the brown phase is visible in the absorption as well, strengthening the hypothesis, that it is not caused by an artifact but rather a very thin layer of δ-CsPbI$_3$ between the quartz substrate and the γ-CsPbI$_3$.

The absorption spectra for the entire line scans on all four samples are shown in Figure 4-2. In order to suppress noise and allow a clearer picture of the compositional dependent changes, the absorption spectra were smoothed by a moving average over ~35 nm. The boundary between the brown and the yellow phase is clearly visible in all samples. As already seen by eye and observed in the XRD line scan (see Figure 3-4(a)) the transition region is very sharp and below the step size of 1 mm. While the absorption edge of the brown phase seems to be constant at ~710 nm, the absorption edge of the yellow phase
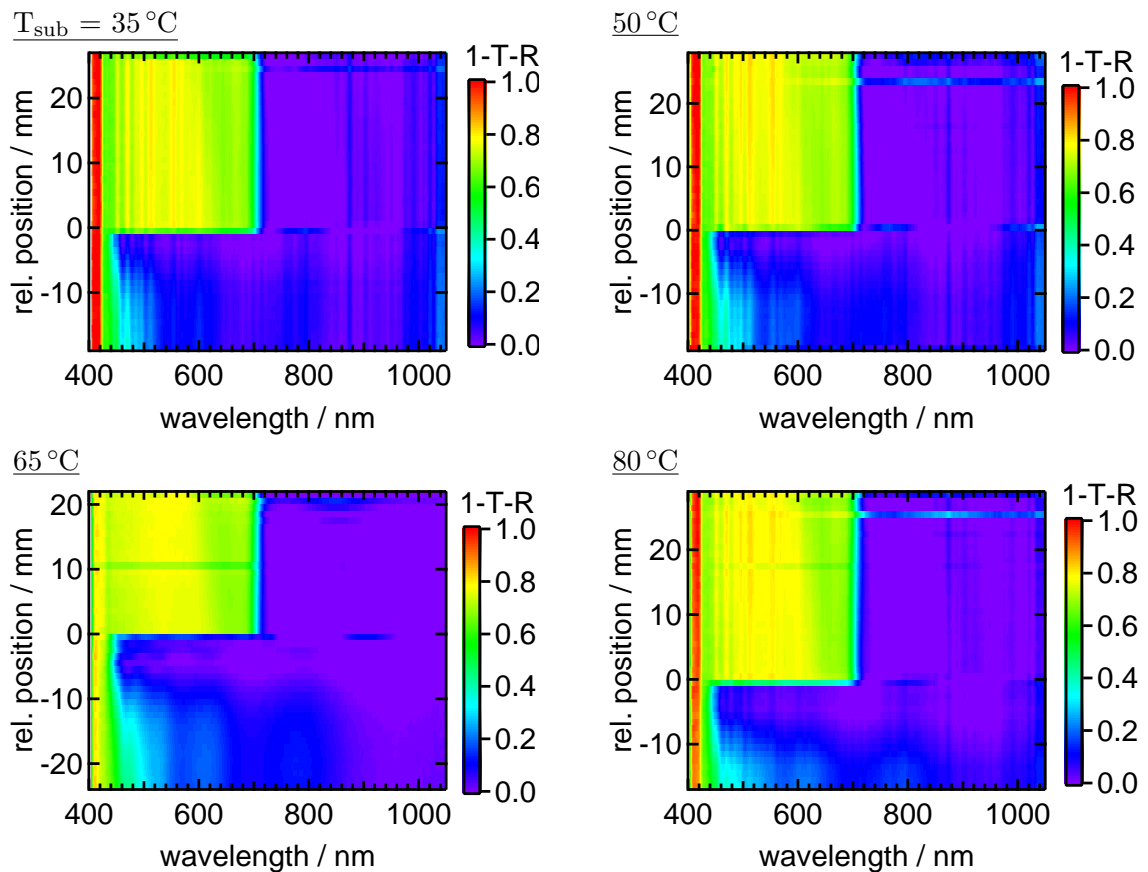
Figure 4-2: *Absorption spectra dependent on the sample position and T$_{sub}$ for line scans parallel to the compositional gradient of the films. A sharp boundary between the brown γ-phase and the yellow δ-phase is visible. The absorption onset of the brown phase seems to be constant around 710 nm, while the absorption onset of the yellow phase shifts from ~430 nm towards higher wavelengths for increasingly PbI$_2$-rich compositions.*

moves towards higher wavelengths and flattens for increasingly PbI$_2$-rich compositions (towards negative relative positions).

For both phases the position of the interference fringes remains almost constant for the different positions on the samples, which indicates a constant layer thickness in first approximation. This underlines the accurate evaporation characteristics of the deposition setup, which results in films with a linear gradient in composition, as seen in XRF but an constant overall layer thickness.

The noisy features which can be seen between 450 nm and 600 nm as well as the steep edge at ~420 nm most likely stem from a slight mismatch in between the reference measurements and the recorded reflection and transmission measurements. While the measurements for 35 °C, 50 °C and 80 °C were performed in one run using the same reference spectra, the measurement for 65 °C employs different reference spectra and shows less artifacts in the specified regions. The secondary absorption edge in the brown phase is hard to see in these pictures due to the noise, which was described above.

At this point the shift in the absorption edge of the yellow δ-phase will not be studied any further, since the material is not relevant for photovoltaic application due to its high band gap. For the investigation of the band gap of the brown γ-phase, the absorption coefficient will be used, since it represents a material property, which is decoupled from the layer thickness. The absorption coefficient was calculated for all spectra of the four line scans using Equation 2-3. Since the consistency of the interference fringes suggested a constant layer thickness, the integral thickness read from the quartz balance monitors of 500 nm was used for the calculations. Figure 4-3(a) shows two single absorption coefficients from the line scan of the 65 °C sample and their derivatives as an example. The two single spectra were calculated from smoothed transmission and reflection spectra, which were averaged over ~15 nm to reduce noise and allow a clearer view on the shape of the absorption coefficient. All following calculations and fit procedures were performed on the raw, non-averaged data. For the absorption coefficient of the brown phase a clear and steep absorption onset can be seen, while the absorption onset for the yellow phase is at the border of the spectrum and thus object to much larger error. As described in Figure 2.2 the derivative of the absorption coefficient can be used to quantify the energy of the absorption onset. It is important to note, that the absorption onset is not necessarily equal to the energy of the band gap, but still can be used as a measure to describe relative changes for different compositions within a sample or similar samples.

For the brown phase a clear peak is visible in the derivative of the absorption coefficient, indicating an inflection point in the absorption coefficient. The energy, at which this inflection point occurs, is defined as the absorption onset. For the yellow phase a shoulder
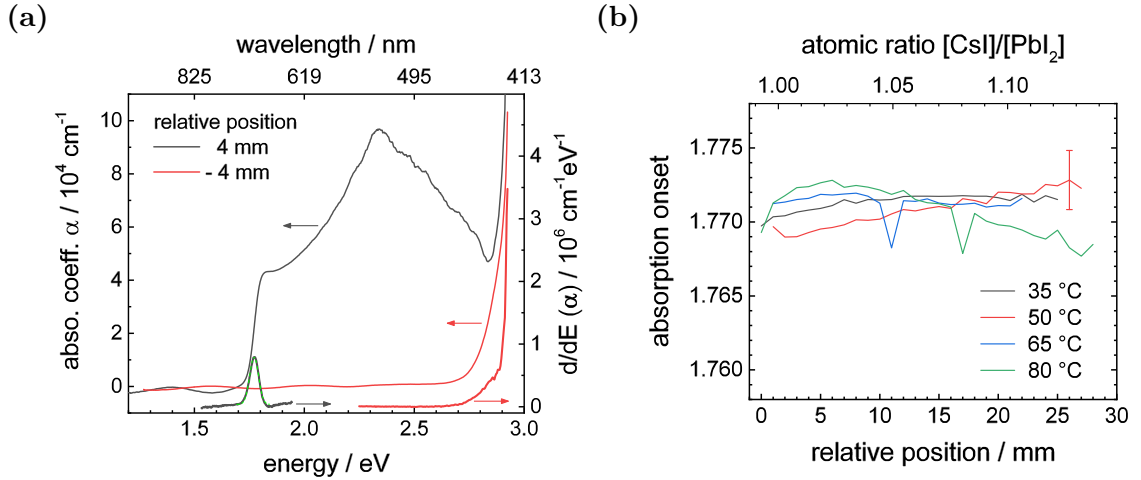
Figure 4-3: *(a) Absorption coefficient α on the left axis for two different positions on a sample evaporated at $T_{sub} = 65\,°C$, one in the brown region (black line) one in the yellow region (red line). The derivatives of the absorption coefficients, which are used to determine the energy of the absorption onsets, are plotted on the right axis. A Gaussian fit to the derivative of the absorption coefficient of the brown phase is inserted (green line). (b) Evolution of the absorption onset dependent on the sample position, and thus chemical composition, for the four samples evaporated at different substrate temperatures.*

is visible in the derivative, which might be the beginning of a peak, indicating an inflection point in the absorption coefficient as well. Due to the limited spectral range of the used setup, no full peak can be seen, so that the determination of the absorption onset is not possible for the yellow phase.

For all four samples, the absorption onset was determined for all spectra of the line scan within the brown region of the sample. The result of these fits is shown in Figure 4-3(b). All absorption coefficients determined for all four samples are within a range of $(1.770 \pm 0.003)\,eV$. Although the energies of the absorption onsets show a gradual trend for most of the sample, which seems to be well above the level of noise, no clear trend in between the samples evaporated at the different substrate temperatures can be found. Considering the step size of the spectrometer of $2\,meV$ in this region, the magnitude of the trends within the single samples appears very small.

The observed trend might also be caused by a change of the shape of the absorption edge. For a simplification of the fitting procedure of the derivative, a Gaussian function is used, although, from a physical point of view, no Gaussian shape nor even a symmetric curve is expected.

From the measurements presented here, no clear assignment of the observed trend to an artifact or a real influence of composition and T_{sub} can be made. Within the limits of error

for the evaluation presented here, the absorption onset does not seem to be significantly influenced by neither the composition, nor T_{sub} and is $(1.770 \pm 0.003)\,\text{eV}$.

4.2 Charge Carrier Generation and Recombination

To investigate the influence of the composition and the substrate temperature during the evaporation on excited charge carriers, photoluminescence measurements were performed. By using a calibrated setup, not only the center energy but also the quantum yield of the photoluminescence can be determined, thus yielding information about the quality of the material as an absorber material for solar cells. The setup used for this measurements is described in Equation 2.2 and employs a calibrated CCD-camera as a detector with a tunable liquid crystal optical filter to allow the acquisition of hyperspectral photoluminescence images. The setup and the script, which was used for the evaluation of the images, were build by José A. Márquez.

The system was used to measure PL imaging on all four samples with different T_{sub}. Figure 4-4 shows an exemplary PL spectrum, which was extracted from the imaging data of the $T_{sub} = 65\,°\text{C}$ sample. The PL spectrum consists of a single peak which can be fitted reasonably well with a Gaussian function to determine the center energy and photon yield of the luminescence. In this example the center energy and yield are calculated to be $1.77\,\text{eV}$ and $5.9 \cdot 10^{16}\,\frac{\text{photons}}{\text{m}^2\,\text{s}}$, respectively. By normalization of the PL-intensity with the known illumination intensity, the external PL-quantum yield can be calculated, which yields $3.7 \cdot 10^{-5}$ in this example. This fit was applied to all pixels of the hyperspectral imaging stack and the resulting parameters are depicted in Figure 4-5 as a 2D map. A
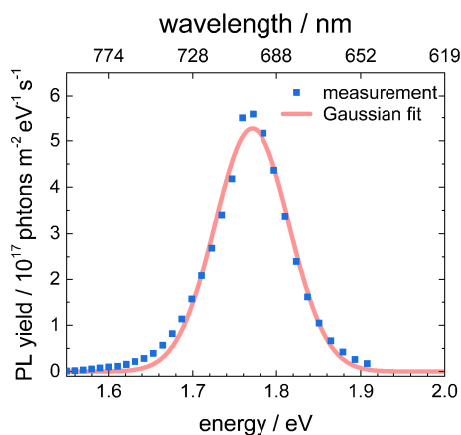
Figure 4-4: *Exemplary PL spectrum (blue dots) for the $65\,°\text{C}$ sample extracted from the PL imaging data set with a Gaussian fit (red line) to the data, which is used to extract the center energy of the PL emission as well as the PL yield.*

(a)

(b)
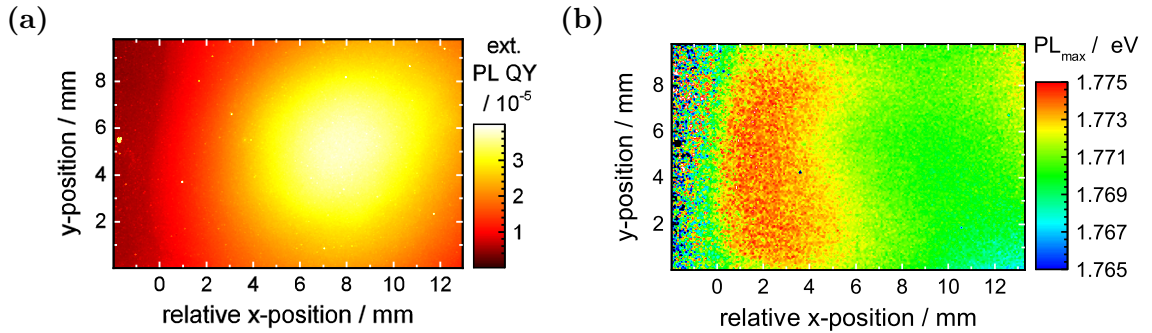
Figure 4-5: Resulting parameters of a Gaussian fit applied to all pixels of the hyperspectral imaging stack of the $T_{sub} = 65\,°C$ sample, where the chemical gradient is oriented in x-direction. (a) External PL quantum yield and (b) center energy of the PL depending on the lateral position on the sample. While the center position mostly shows a dependency in direction of the gradient, the quantum yield also shows a dependency perpendicular to the gradient.

step in the external PL-quantum yield can be seen at the approximate position of the boundary between yellow and brown phase. This is expected, since the band gap of the yellow δ-phase is below excitation wavelength of 455 nm of the LEDs (see Section 4.1). A local maximum of the quantum yield not only parallel but also perpendicular to the compositional gradient can be seen in the center of the depicted section of the brown phase. This might be an artifact due to inhomogeneous illumination, since no correction for inhomogeneous illumination was applied and no change of the materials properties is expected perpendicular to the gradient. Detailed measurements of the homogeneity of the illumination have to be performed, to confirm this hypothesis.

In the center energy of the PL this trend perpendicular to the gradient is much less pronounced. A more distinct trend parallel to the gradient is visible, which reveals a decreasing energy as the composition deviates from stoichiometry towards increasing CsI content.

To visualize this trend, line scans were extracted in x-direction from the 2D set of fit parameters, which were averaged over relative y-positions between 5 mm and 7 mm to reduce the noise level. This section of the relative y-position was chosen to minimize the effect of inhomogeneous illumination perpendicular to the compositional gradient described above.

The resulting line scans for all four samples are shown in Figure 4-6. All four samples show a similar trend in quantum yield and center energy of the PL. The quantum yield increases with increasing CsI content of the sample towards a local maximum, as already seen in Figure 4-5(a). It seems, that the increase in the quantum yield occurs closer to the stoichiometric boundary with increasing T_{sub}. Due to the possibly inhomogeneous illumination, however, a definitive correlation can not be confirmed. In addition, it can
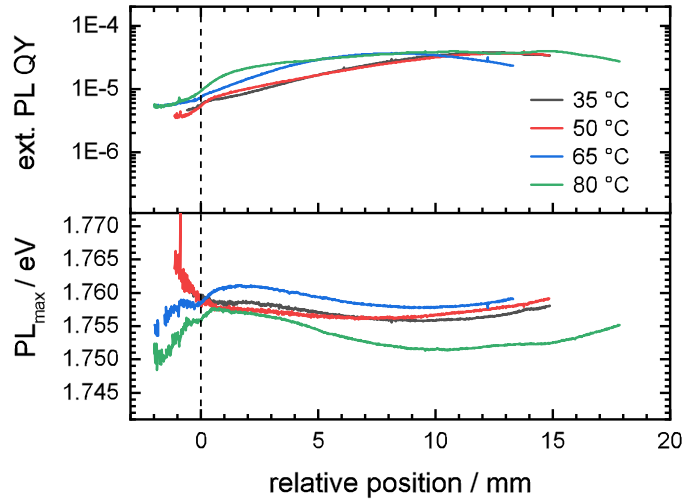
Figure 4-6: *Extracted lines of the 2D fit results by averaging over relative y-position between $5\,\mathrm{mm}$ and $7\,\mathrm{mm}$ for the four samples with different substrate temperature, respectively. The top graph shows the external PL quantum yield, while the bottom graph shows the center energy of the PL emission dependent on the position relative to the boundary between yellow and brown phase. For all four samples the quantum yield seems to increase, as the composition becomes more CsI-rich, while the PL maximum shows a local maximum close to the stoichiometric boundary.*

be seen, that the quantum yield does not decrease to zero in the PbI_2-rich yellow region of the sample. This is unexpected, since the wavelength of the illumination is above the band gap of this phase. This error might be caused PL luminescence of the neighboring brown part of the sample, which is reflected within the quartz substrate.

All four samples show a local maximum of the .PL center energy at around $2\,\mathrm{mm}$ relative to the stoichiometric boundary, which proceeds to a local minimum at around $10\,\mathrm{mm}$. For more CsI-rich compositions, the center energy of the PL seems to increase again.

Large relative margins of error have to be declared for the values determined by this method due to the non-corrected inhomogeneous illumination. Since the minimum in the position of the PL maximum is reminiscent of the shape of the maximum in the PL QY, which is supposed to be dominated by the inhomogeneous illumination, the precision of these values has to be questioned as well. Despite these large margin of errors, however, the measurements still reveal, that neither composition nor T_{sub} have a drastic influence on the luminescence properties of the material. All values for the external PL quantum yield are in the same order of magnitude and the center position of the PL is in a range of $(1.755 \pm 0.010)\,\mathrm{eV}$ for all samples and all compositions. The measurements therefore confirm the results from the UV-Vis measurements as described above.

4.3 Charge Carrier Dynamics

For the application of the material in solar cells, not only the band gap and thus the generation of the charge carriers is of importance, but the charge carrier dynamics, as well. For insights into the lifetime and mobility of the carriers, time resolve PL and OPTP measurements were performed. The TRPL measurements and data evaluation was performed by Charles Hages. [121] The measurements and evaluation of the OPTP was performed by Hannes Hempel.[105, 106] Therefore, only the results of the measurements will be presented here, which is the Shockley-Read-Hall lifetime τ_{SRH} from TRPL and the sum mobility of electrons and holes μ_{THz} from OPTP. The data was already presented in [107], where more details about the measurements can be found.

The resulting data is shown in Figure 4-7. Since the band gap in the yellow region of the sample is above the excitation energy of 1.85 eV no lifetime can be measured in this area, which is represented by negative relative positions and compositions smaller than $[CsI]/[PbI_2] = 0.99$. From the boundary between the two phases towards increasing CsI-content in the films, the lifetime increases steeply to a maximum of ~80 ns at a relative
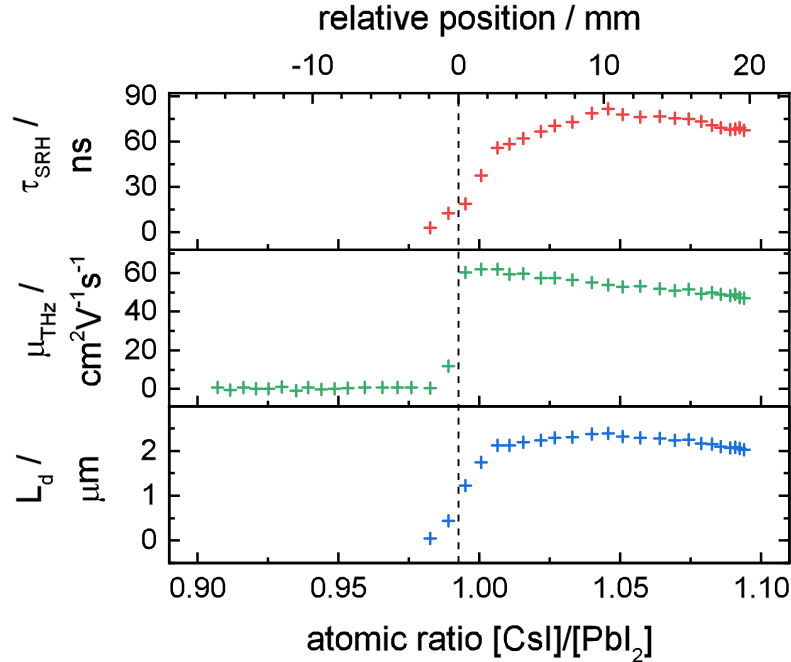
Figure 4-7: *From top to bottom: Shockley-Read-Hall lifetimes from TRPL, sum mobility of electrons and holes from OPTP and diffusion length, calculated from Equation 4-4 over the position relative to the phase boundary and thus over composition for a $T_{sub} = 50\,°C$ sample. While the lifetime shows a local maximum at ~10 mm and $[CsI]/[PbI_2] = 1.04$, the mobility is largest close to the boundary and slightly decreases for more CsI-rich compositions. The resulting diffusion length is ~2 µm and shows only slight variations within the investigated range of composition.*

position of ~10 mm, which represents a composition of ~1.04. Within the compositional range of this sample, the lifetime is above a value of 60 ns, which is higher than in most previous reports on CsPbI$_3$.[72, 116, 122]

The mobility from OPTP measurements has its maximum value of 62 $\frac{\text{cm}^2}{\text{Vs}}$ closest to the boundary between the phases. The mobility slightly decreases as the composition becomes more CsI-rich and results in a mobility of 48 $\frac{\text{cm}^2}{\text{Vs}}$ at a relative position of 18 mm, which translates to a composition of [CsI]/[PbI$_2$] = 1.09.

It has been calculated, that in CsPbI$_3$ the electron mobility μ_{e^-} and hole mobility μ_{h^+} are very similar, [123] so that they can be calculated from the sum mobility measured by OPTP by $\mu_{e^-} \approx \mu_{h^+} \approx 0.5 \ \mu_{\text{THz}}$. Using this relation and Equation 4-4 the diffusion length of the charge carriers can be estimated.

$$L_d = \sqrt{\mu \ \tau_{SRH} \ \frac{k_B T}{e}} \qquad (4\text{-}4)$$

The results for this calculation are shown in Figure 4-7, as well. For all ratios of [CsI]/[PbI$_2$] > 1 investigated in this sample, the diffusion length is above 2 μm and thus four times larger than the estimated thickness of the layer of 500 nm. Therefore, charge carrier transport within the CsPbI$_3$ layer should not be a limiting factor for the performance of the material as absorber in solar cells.

Summing up the results from the measurements of the optoelectronic parameters presented above, no significant change in these parameters can be observed depending on composition and T$_{\text{sub}}$. For all T$_{\text{sub}}$ and compositions, the band gap is in the optimal range for application in tandem cells,[64] and long charge carrier lifetimes and high mobilities result in a sufficiently long diffusion length for efficient charge extraction. This demonstrates, that high efficiency solar cells can be produced from CsPbI$_3$ by co-evaporation at low substrate temperatures.

4.4 Application in Photovoltaic Devices - Solar Cell Performance

To verify this expected suitability of the material for application in photovoltaics, solar cells were produced, employing the evaporated CsPbI$_3$ layers as absorber material, as described in Equation 2.2. Apart from the evaporation of the CsPbI$_3$ absorber, the fabrication of the cells as well as the measurements on the cells were performed by Amran Al-Ashouri and were already presented in [107].

For the evaporation of the cells four inch×inch substrates with already prepared front contacts were mounted on the substrate holder. To ensure the formation of γ-CsPbI$_3$ on

all four substrates, the evaporation rates were chosen to be [CsI]:[PbI$_2$] = 1.2:1, resulting in cells with compositions of [CsI]/[PbI$_2$] = 1.10, 1.13, 1.16, 1.24, 1.27 and 1.30, respectively (see Section 2.4). For three of the samples the layer stack was completed and the cells were characterized by JV-scans to determine their photovoltaic performance. For 14 out of the 18 sub-cells, a photovoltaic behavior could be observed, while three sub-cells could not be measured due to a partial malfunction of the contacting substrate holder.

The measurement of the JV-scan on the best performing sub-cell can be found in Figure 4-8(a) as an example. A strong hysteresis effect can be seen between the two measurements with different direction of the voltage sweep. This manifests in a large difference in V$_{OC}$ of 0.90 V in forwards direction and 0.96 V in reverse direction, while the J$_{SC}$ is more constant with $-18.1\,\mathrm{mA\,cm^{-2}}$ and $-17.8\,\mathrm{mA\,cm^{-2}}$, respectively. For the FF, a large difference can be seen with values of 60.7 % and 70.0 %, as well as for the PCE with values of 9.99 % and 12.47 %, respectively. Despite the hysteresis, the cell performance is comparable to cells, which were recently reported in literature. [78, 124, 125] While the current is decently high as compared to the theoretical Shockley-Queisser limit of ~21 mA/cm^2,[126, 127] the open circuit voltage shows an enormous deficit as compared to the theoretical maximum of 1.47 V.[127] This difference might partially be caused by the same issue as the hysteresis effect.

In recent literature the origin of this hysteresis is found in slow drifting ions, leading to a charge accumulation. Often times this effect is promoted by energetic barriers at the interfaces between the different layers of the cell, such as energy offsets between different
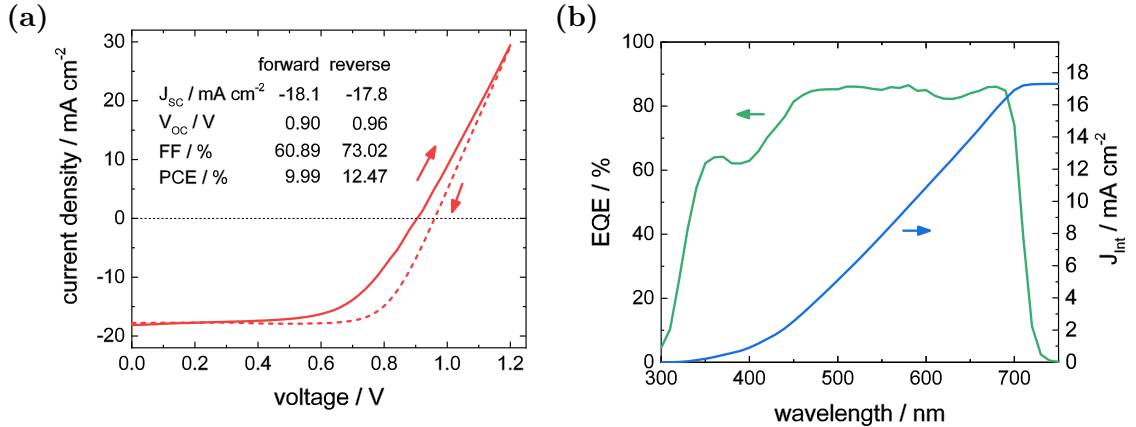
Figure 4-8: *(a) JV-scan and (b) EQE measurement of the best performing sub-cell. In the JV-scan a strong hysteresis effect can be seen for the different directions of the voltage sweep. The characteristic parameters for both scan directions are given in the inset table. In the EQE measurement (green line) high values above* 80 % *can be seen over a wide range of the spectrum. The integrated current (blue line) results in a total of J$_{Int}$ =* 17.3 mA cm^{-2}.

layers of the cell or even insulating interlayers.[128–131] Another indication for this hypothesis is the shallow slope at the voltage-axis intercept in this measurements, showing a high series resistance of the cell.

As seen in the SEM images presented in Section 3.4, the segregation of a secondary phase is visible at the top of the evaporated layers, which covers an increasing amount of the surface with increasing CsI-excess in the integral composition of the film and is thus suspected to be CsI. Although no SEM images were taken in the compositional range used for the cell fabrication, careful extrapolation of the increasing trend of the coverage suggests, that a major part of the surface might be covered or even a closed layer might have formed. Since CsI features a high band gap of $6.4\,\mathrm{eV}$ it is likely to form an energetic barrier, hindering the charge transport and lowering the cells voltage.

Additional indications for intermediate layers hindering the charge transport can be found in EQE measurements, which are especially sensitive to parasitic light absorption at the front contact. The result of the EQE measurement for this cell is shown in Figure 4-8(b). The EQE of the cell is above $80\,\%$ over a wide range of the spectrum, which is similar to the current record cell with $17\,\%$ power conversion efficiency.[78] The integrated current density yields $J_{\mathrm{Int}} = 17.3\,\mathrm{mA\,cm^{-2}}$ for the spectral range of this measurement, which is in agreement with the J_{SC} from the JV-scan.

A prominent dip in the EQE can be seen at around $400\,\mathrm{nm}$, hinting towards a parasitic absorption of light. For a more detailed investigation, the EQE of three sub-cells with different $CsPbI_3$-compositions are measured and depicted in Figure 4-9. It can be seen,
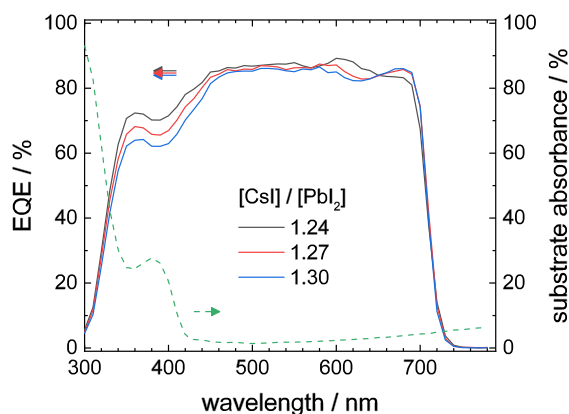
Figure 4-9: *EQE for three sub-cells on the same substrate (left y-axis). Each of the sub-cells employs an absorber with different composition of $[CsI]/[PbI_2] = 1.24$, 1.27 and 1.30. The intensity of the dip at $\sim 400\,\mathrm{nm}$, that can be seen for all samples, varies for the different compositions. This also manifests in the integrated $J_{sc,int}$ of $17.72\,\mathrm{mA/cm^2}$, $17.54\,\mathrm{mA/cm^2}$ and $17.28\,\mathrm{mA/cm^2}$, respectively. The optical absorbance of a substrate with only the ITO and PTAA front contact (right y-axis) shows a peak at the same position as the dip in the EQE of the cells.*

that all three samples show a similar dip in the EQE as described above, strengthening the hypothesis of parasitic absorption. Therefore, the optical absorption of a substrate covered with the ITO and PTAA front contact is measured and is inserted in Figure 4-9. The absorption shows a peak at the same position as the dip in the EQE, which verifies, that the front contact attenuates the light before it reaches the absorber. However, a comparison of the EQE spectra for the different compositions reveals, that the dip seems to have the same shape, but is shifted to lower values for increasing CsI content. A variation of the thickness of the contacting layers could partially explain this behavior. However, the PTAA layer was deposited by spin coating, which is unlikely to produce a linear variation in thickness but rather a concentric one. In addition, for cells produced with the same type of substrates and contacting layers but different absorber material, no such trend in the EQE was observed.

This suggests, that the substrate and front contacts are not the only reason for the decrease in EQE, which is supported by the fact, that the decrease in the EQE starts at higher wavelengths than the absorption. Comparison of the band gaps of different secondary phases of the $CsPbI_3$ (see Table 2-1) reveals, that this absorption could be caused by the yellow δ-$CsPbI_3$. This seems especially likely, since the UV-Vis measurements on the bare absorbers (see Section 4.1) as well as in-situ reflection measurements during the evaporation (see Section 3.5) suggested the presence of a very thin layer of yellow δ-$CsPbI_3$ between the substrate and the brown γ-phase layer. The presence of the thin insulating layer of δ-$CsPbI_3$ could explain the additional decrease of the EQE and also account for the increased series resistance and hysteresis, which was observed in the JV-scan. The trend in the decrease of the EQE hints towards a correlation of the composition of the sub-cells with the thickness of the δ-$CsPbI_3$ layer. This can also be seen in the decrease in the total, integrated current density for the three sub-cells, of $J_{sc} = 17.72\,\text{mA/cm}^2$, $17.54\,\text{mA/cm}^2$ and $17.28\,\text{mA/cm}^2$ for the compositions of $[CsI]/[PbI_2] = 1.24$, 1.27 and 1.30, respectively.

For a more detailed analysis of this trend, all cell parameters for all measured and working sub-cells are presented in Figure 4-10. Although a general trend of a decreasing current density with increasing composition can be found within each of the three samples, no general trend for the current density can be found for the entire investigated compositional range. It can however be seen, that the differences between different sub-cells can be enormous, especially when comparing sub-cells on different substrates. While most of the cells show a current density of above $15\,\text{mA/cm}^2$, some values, especially for the very CsI-rich sub-cells, are as low as $9\,\text{mA/cm}^2$.

Similar variations can also be seen for the other solar cell parameters. For the open circuit voltage and the fill factor the variations are not as prominent with values between
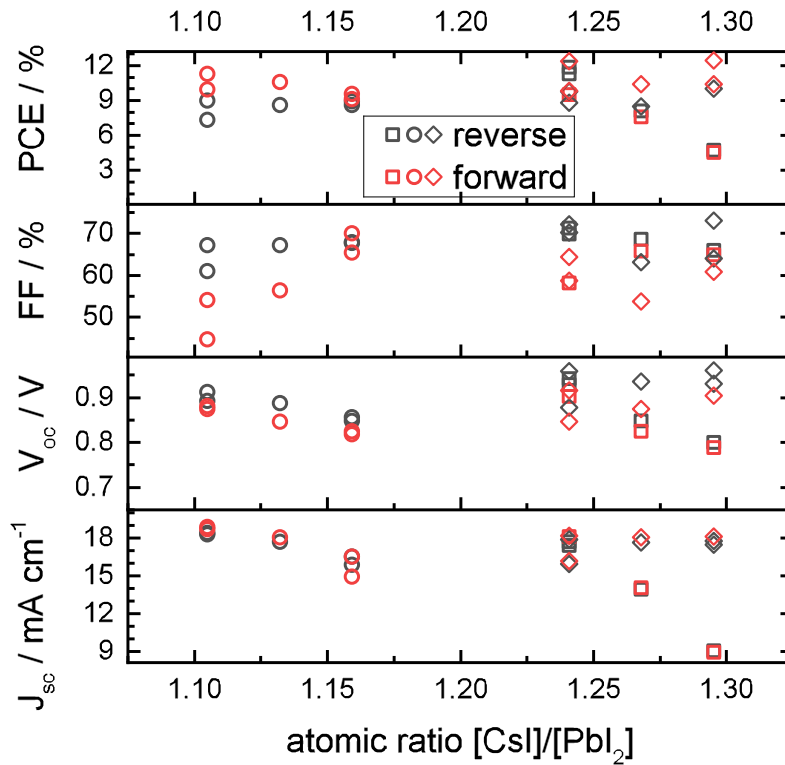
Figure 4-10: *Photovoltaic performance parameters for all working sub-cells for forwards scan direction (red symbols) and reverse scan direction (black symbols) over the composition of the absorber. Different symbols are used for sub-cells on different substrates. No clear trend of the parameters dependent on the composition can be found. Major differences in the parameters for cells with the same nominal composition can be seen, especially if they are located on different substrates. This indicates a deficient reproducibility in cell fabrication.*

$0.79\,V$ and $0.96\,V$ for the V_{OC}, and FF values between $45\,\%$ and $73\,\%$. The relative deviations in the PCE between the sub-cells, however, is even larger than for the J_{SC}, ranging between $4.5\,\%$ and $12.5\,\%$. For none of these quantities a clear trend can be found for the entire compositional range of these samples. Thus, the origin of the trend in parasitic absorption in the EQE cannot be further clarified.

As already suggested by the characterization of the optoelectronic properties of the materials, the fabricated solar cell devices demonstrate the suitability of the co-evaporated $CsPbI_3$ thin-films for photovoltaic applications. The elimination of the suspected energetic barriers from insulating layers at the interfaces, as well as optimization of the contact layers are promising approaches from an improvement of the power conversion efficiencies.

5

High Temperature Phase Transition

In most reports on the formation of $CsPbI_3$ and its application in solar cells the initial material, which is formed during the deposition, is the yellow δ-phase of $CsPbI_3$.[83, 90, 116, 132] It is then transformed to the desired brown phase by thermal annealing at high temperatures. For pure $CsPbI_3$ the required temperature for the transition to the brown phase is reported to be 300 °C to 320 °C [83, 90, 116, 132]. More recent recipes, which include additional components, as described in Section 1, require lower annealing temperatures of 100 °C to 80 °C.[44, 71, 73, 74]

Here, such a high temperature annealing step is applied to the samples described above to investigate the influence of the phase transitions on the properties of the material. In order to investigate the differences in the properties also depending on the substrate temperature during the evaporation, again four samples with different T_{sub} are considered.

This section is structured similar to the report of as-deposited samples. After the description of the annealing step the physical properties of the material such as chemical composition, crystal structure and morphology are reported, followed by the optoelectronic properties. In chronological order, however, the optoelectronic measurements were performed first. During the measurement of the PL, the former yellow, PbI_2-rich part of the film returned to the yellow δ-phase at ~3.5 h after the annealing. Thus, only UV-Vis measurements could be performed, while the sample was present completely in the brown phase. The rest of the measurements were performed only in the remaining brown part of the sample or, where possible, in the yellow phase.

5.1 Annealing Procedure

The annealing is performed on a hotplate within the inert atmosphere of a glove box without any intermediate air exposure, to ensure, that the $CsPbI_3$ layers are not affected by the influence of ambient air. A thermocouple was moved across the surface of the hotplate, to test homogeneity of the temperature. It was found, that only an area of roughly 6 cm by 6 cm in the center of the hotplate showed a temperature of ~320 °C, when the hotplate was set to nominal 400 °C. This area was marked on the hotplate, to be able to place the substrates precisely for the annealing.

The samples used in this process are as-deposited samples with T_{sub} = 35 °C, 50 °C, 65 °C and 80 °C with a gradient in composition, which contain a region with the brown γ-phase and a region with the yellow δ-phase, as described in Section 3.3. From reports in literature it is expected, that the brown γ-phase part of the samples transforms to the yellow δ-phase at a temperature of ~80 °C.[83] Upon further heating the entire sample, which now completely consists of the yellow δ-phase, is expected to transform into the black cubic α-phase.[69]

All four samples are placed on the pre-heated hotplate simultaneously and the temperature of the samples starts to increase with time. After the transition temperature to the cubic α-phase is reached and the samples turned black completely, they are removed from the hotplate simultaneously by pushing them onto a solid aluminum block. This leads to a rapid cooling and thus freezes the crystal phase, preventing the films to undergo the transition back to the yellow δ-phase.[116, 133]

5.2 In-Situ Monitoring of the Optical Reflection

For a quantitative study of the phase changes during annealing, the process is monitored with a CCD-camera (*The Imaging Source, DBK 41AU02.AS*), which continuously acquires images of the reflection of the films. A series of images taken at a frequency of 3 Hz was taken, to show the entire annealing process. Since more thermal inhomogeneities on the surface of the hotplate are expected, the samples were placed in a mixed-up T_{sub}-order. Therefore, effects of the sample position on the phase transition behavior can be decoupled from effects from composition and T_{sub} during evaporation of the samples.

Single images extracted from the continuous imaging series, which display the γ-to-δ-transition, are shown in Figure 5-1. The transition from the brown γ-phase to the yellow δ-phase occurs very fast and is almost completed at 10.5 s after the samples were placed on the hotplate. The remaining dark stripes at the top left corner of the sample consist of very CsI-rich material due to shading of the substrate holder during the evaporation,
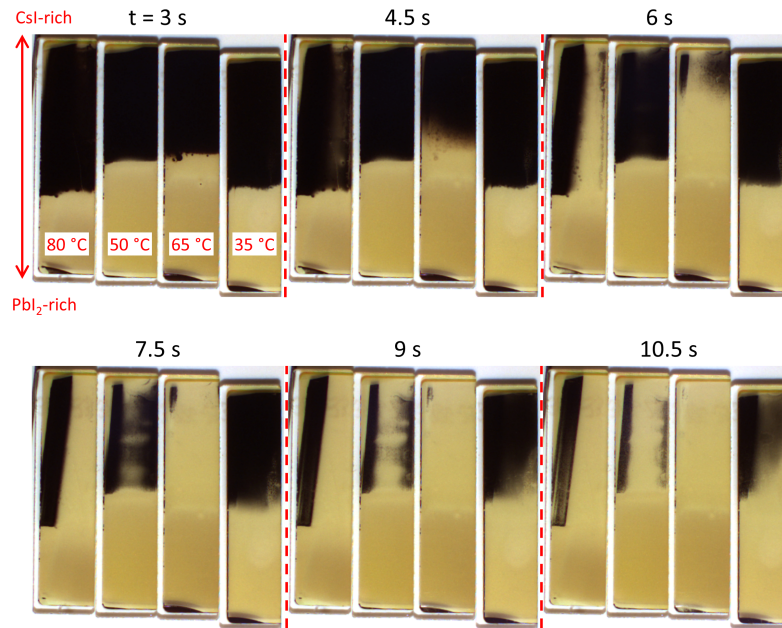
Figure 5-1: *Images from different times of the annealing process, showing the transformation from the brown γ-phase to the yellow δ-phase on samples evaporated at $T_{sub} = 35\,°C$, $50\,°C$, $65\,°C$ and $80\,°C$. $10.5\,s$ after the samples are placed on the hotplate, the transformation is almost completed. For the samples with high T_{sub} the transition occurs faster than for samples with lower T_{sub}. The remaining dark stripes at the top left corner of the sample consist of very CsI-rich material due to shading of the substrate holder during the evaporation.*

which transforms significantly later than the rest of the samples. A trend in the transition times depending on T_{sub} can be seen. While the $65\,°C$ and $80\,°C$ samples transform first at ~6 s after being placed on the hotplate, the $50\,°C$ sample only transforms after 9 s, followed by the $35\,°C$ sample, which has not completely transformed after 10.5 s. For the $80\,°C$ and $50\,°C$ samples the transition time seems to occur almost simultaneously in the entire brown region, independent of the vertical position on the sample and thus chemical composition. For the $65\,°C$ and $35\,°C$ samples, however, the transition seems to start close to the stoichiometric boundary and proceed upwards towards the most CsI-rich edge of the sample. The differences between the color of degraded CsI-rich region of the sample and the PbI$_2$-rich region of the sample will be addressed in Section 6.

The second phase transition, in which the films converts to the black cubic α-phase, occurs at a longer time scale. Figure 5-2 shows single images from the annealing process during this transition. As most prominent feature of this image series, a trend in the transition times, starting from the corners of the samples and moving towards the center can be seen. Due to the almost symmetric and concentric evolution of the phase transition, this effect most likely originates from a temperature effect rather than from sample
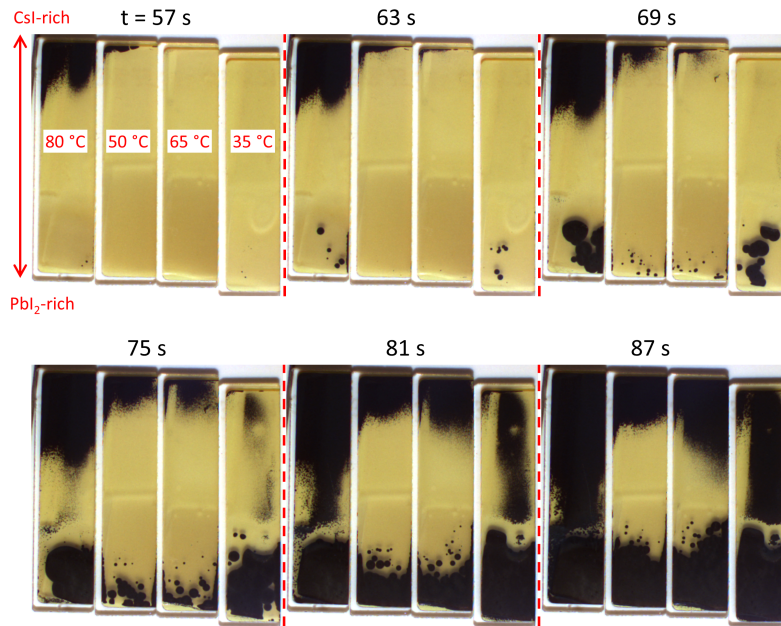
Figure 5-2: *Optical reflection images of the phase transition from the yellow δ-phase to the black α-phase during annealing of samples with different T_{sub}. The images are taken at different times after the start of the annealing. A clear trend in the transition times from the corners of the samples towards their center can be seen. Domains with significantly different sizes form depending on the composition of the sample.*

composition or T_{sub}. Compared to the γ-to-δ-transition, the δ-to-α-transition takes significantly longer. While the appearance of the first black spot on the sample occurs in the top left corner ~52 s after the samples were placed on the hotplate, the transformation in the center finishes only ~144 s after the beginning of the annealing. The second prominent feature in the image series, which is the different nucleation and growth of nuclei depending on the composition, will be discussed below.

For a more detailed analysis of both phase transitions, the transitions are quantified by the change of brightness of each pixel. The time of the phase change is defined to be the inflection point of the brightness over time, which is determined by fitting a peak function to its derivative. Following this method, one vertical line per sample was evaluated, which was chosen at a position, that is not affected by the very CsI-rich areas described above. The resulting transition times for these extracted lines and for the two transitions are shown in Figure 5-3. The γ-to-δ-transition seems to mainly depend on T_{sub} and on the position relative to the former phase boundary, thus on the chemical composition of the sample. While the transition for the 65 °C and 80 °C samples is finished after 6 s, the transition for the 50 °C sample finishes after 9 s. The transition for the 35 °C sample even takes 12 s, being twice as long as the transition for the 65 °C and 80 °C samples. This

(a)

(b)
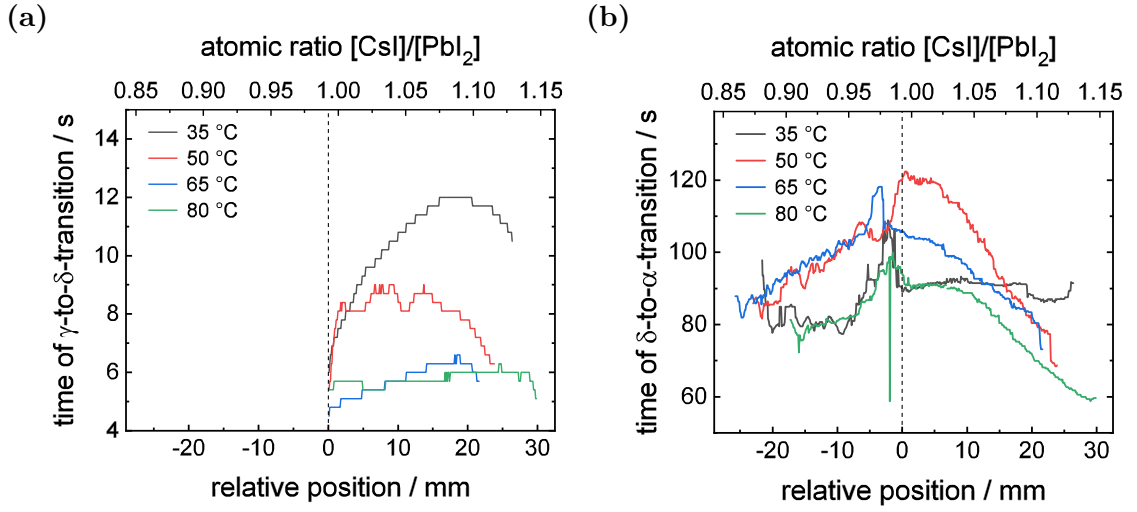
Figure 5-3: *Times for the phase transition during annealing of samples with different T_{sub} dependent on the position on the sample relative to the former phase boundary. The first transition (a) refers to the transformation from the brown γ-phase to the yellow δ-phase, therefore only reporting values in the former brown, CsI-rich part of the sample, denoted by positive relative positions. The δ-to-α-transition (b) refers to the transition of the yellow δ-phase to the black α-phase. While for the first transition a dependency on T_{sub} can be seen, the second transition seems to mostly depend the position on the hotplate.*

confirms the qualitative observations made with the single extracted images as described above.

The dependence of the transition times on the chemical composition can be seen by the fact, that the transition starts at the stoichiometric boundary in the center of the samples, denoted with the relative position of 0 mm and continues to move towards larger relative positions, indicating an increase in CsI content. As T_{sub} increases, this trend gets less pronounced, so that the transition of the 80 °C sample occurs almost simultaneously for all compositions. Details on the stability of the samples depending on the composition and T_{sub} will be discussed in Section 6.

The time, after which the δ-to-α-transition occurs, is mainly dominated by the position on the samples. For all samples the transition starts at the edges of the sample and then moves towards the center, showing a peak or step at the stoichiometric boundary. In addition, the transition of the outer two samples, being 35 °C and 80 °C, starts and finishes earlier, than the transition for the 50 °C and 65 °C samples, which were placed between the former two samples. This confirms the observation made on the single extracted images as described above.

Since an inhomogeneous temperature distribution of the hotplate was already discovered by the measurements with a thermocouple, it seems likely, that the temperature varies

significantly even within the marked rectangle. For more precise measurements of the distribution of the temperature, an IR-camera (*Fluke TiS75*, $\varepsilon = 0.93$, temperature error $3\,\%$) was used. A montage of the optical image from this camera and the temperature data from the IR-image of this camera is shown in Figure 5-4. Although the hotplate is set to a nominal temperature of $400\,°C$ the maximum temperature on its surface is below $340\,°C$, as already measured with the thermocouple. The temperature image verifies, that a temperature above $320\,°C$ is only reached within the area, which was determined with the thermocouple measurement. Even within this area significant variations in the temperature of over $20\,°C$ can be seen, which manifest especially in two spots with temperatures above $330\,°C$. To investigate the influence of this inhomogeneity on the surface temperature of the substrates during the annealing procedure, an IR-image series was recorded during a reference annealing process. To avoid contamination of the IR camera, the reference process was performed in a fume hood outside of the glove box and with clean bare quartz substrates. The reference process was conducted with the same procedure and timing as the actual annealing process to maximize the comparability.

Figure 5-5 shows the temperature distribution from two images, which are extracted from the image series and are taken at $1.5\,s$ and $87\,s$ after the placing the reference substrates on the hotplate, respectively. $1.5\,s$ after the samples were placed on the hotplate, a slightly cooled area ~$1\,cm$ around the substrates can be seen on the surface of the hot-
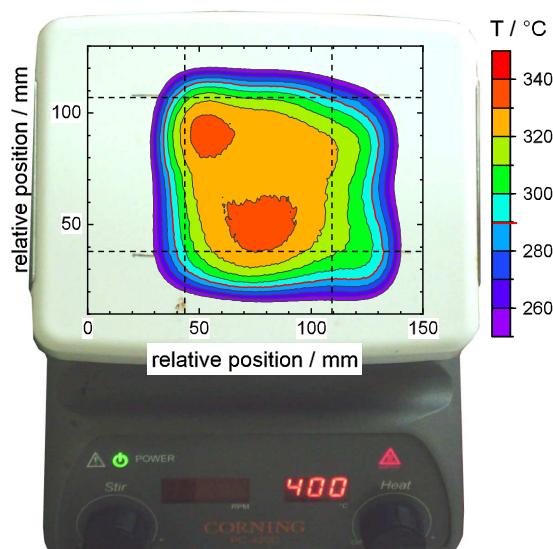
Figure 5-4: *Montage of the optical and the IR-image of the empty hotplate, which is used for the annealing process. The hotplate is set to a nominal temperature of $400\,°C$. The dashed lines indicate the area, which was marked to have a temperature above $320\,°C$ as measured with a thermocouple. Even within this area the temperature varies over more than $60\,°C$.*
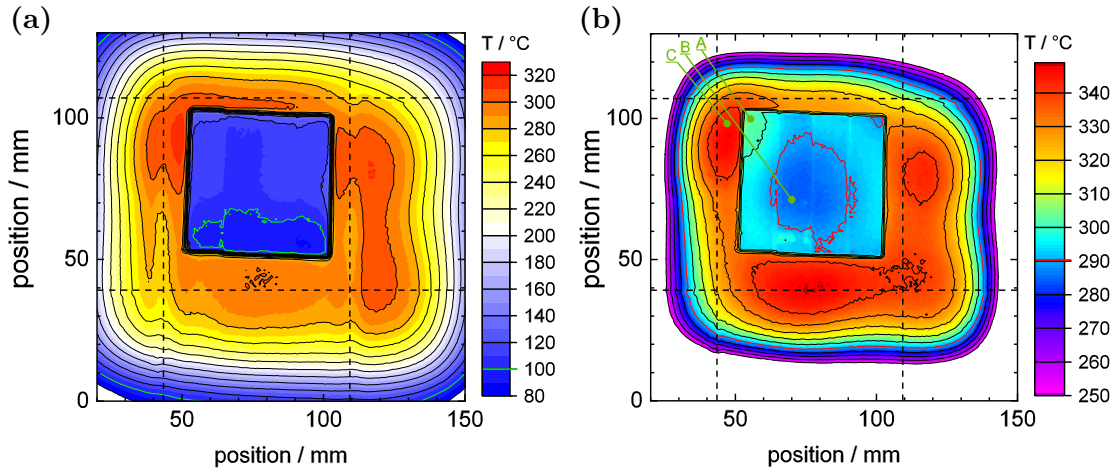
Figure 5-5: *2D-temperature distribution from IR-images, which are extracted from an image series of a reference annealing process (a)* $1.5\,\text{s}$ *and (b)* $87\,\text{s}$ *after the substrates were placed on the hotplate. After* $1.5\,\text{s}$ *the substrates show a slight temperature gradient in vertical direction with temperatures above* $100\,^\circ\text{C}$ *(green contour) over most of the sample. The temperature gradient after* $87\,\text{s}$ *is concentric with values above* $300\,^\circ\text{C}$ *at the corner and below* $290\,^\circ\text{C}$ *(red contour) in the center. The dashed lines mark the predefined region with temperatures above* $320\,^\circ\text{C}$ *on the hotplate. Note the different color scheme for the different temperature ranges in the two images.*

plate. This is caused by the metal frame, which is used to push the samples onto the hotplate. The temperature on the entire surface of substrates is above the phase transition temperature from the brown γ-phase to the yellow δ-phase of $80\,^\circ\text{C}$ as described above. The gradient in temperature on the substrates is mostly linear, which results from the fact, that the substrates were pushed onto the hotplate from below. Therefore, the top edge of the samples is in touch with the hotplate slightly longer and the bottom part is moved over a path on the hotplate, that has already been slightly cooled by the rest of the substrate. The second sample from the left has a marginally lower temperature than the rest of the samples, which might be caused by a dust particle between the substrate and the hotplate.

After $87\,\text{s}$ the temperature of the hotplate is increased to values above $340\,^\circ\text{C}$ to counter the aforementioned cooling. The highest temperature values can be seen in the two hot spots, that were already seen in the image of the empty hotplate in Figure 5-4. It can be seen, that these hot spots influence the surface temperature of the substrates. The spot with the highest temperature on the substrates can be seen in the top left corner, in direct proximity to the hot spot on the hotplate.

The temperature gradient on the surface of the substrates is concentric with the highest temperatures on the edges. While for common temperature distributions of hot bodies

the reverse trend is expected due to the increased surface-to-volume ratio on the edges, the trend seen here can be explained by the insufficient heat capacity of the hotplate. As the cold substrates get in contact with the hotplate, the hotplate is cooled down in the positions, where the substrates touch. While the area in the center of the sample is surrounded by likewise cooled material, the areas at the edges of the sample can draw heat from the surrounding hotplate material, which remains at relatively higher temperature. Thus the temperature at the edges of the sample increases faster, while material in the center of the samples awaits the re-heating of the hotplate itself.

Quantitatively, this can be seen by extracting the time dependent temperature values at characteristic points on the substrates from the IR-image series. Figure 5-6(a) shows this evolution for the three points on the sample that are marked in Figure 5-5(b). The hotplate is initially cooled down by the substrate. To counter this cooling, the temperature is increased and overshoots to almost $350\,°C$ before it cools down to $330\,°C$ again. The spot on the corner of the substrates heats up significantly faster than the spot in the center. It benefits from the increase of the hotplate temperature and follows the course of the overshoot. In the end of the process, the temperature in the corner of the sample is lower than in the center, following the expected thermal distribution of a heated body as described above.
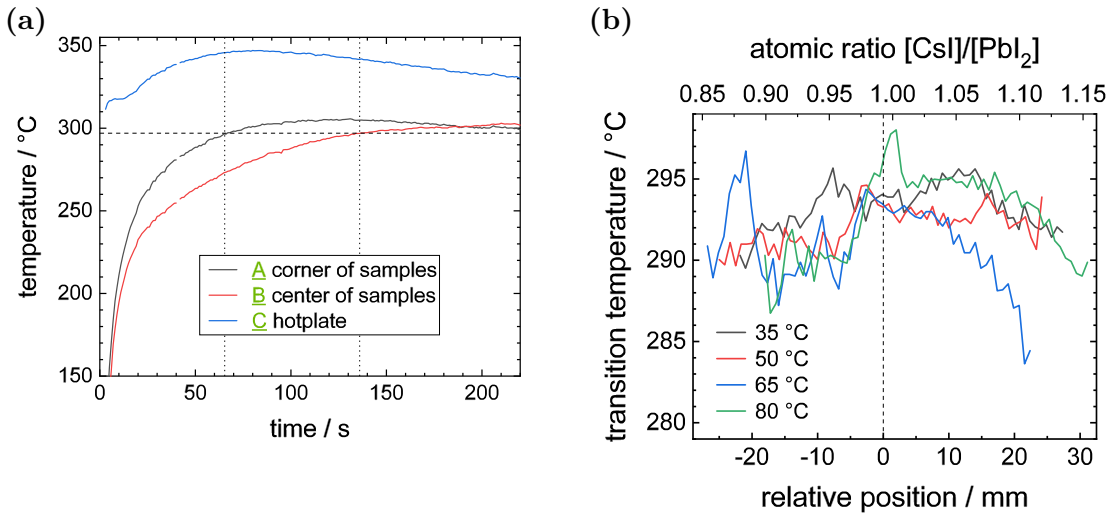
Figure 5-6: *(a) Temporal evolution of the surface temperature on two characteristic points on the substrates and on the surface of the hotplate during the reference annealing process. The temperature at the corner of the substrate increases significantly faster than in the center of the substrates. The dashed lines mark the time of the phase transition at the two spots on the sample. (b) Temperature of the phase transition to the black α-phase dependent on the relative sample position and thus composition for samples with different T_{sub}. The temperatures were obtained from a combination of optical monitoring of the phase transition and the temperature evolution from an IR-image series.*

When comparing the time of the phase transition at this two specific points as read from the in-situ imaging (see dashed lines in Figure 5-6(a)), it becomes apparent, that the current temperatures for the two points at the respective times are identical. In combination with the strong resemblance of the temperature distribution on the substrate surfaces after 87 s and status of the phase transition after 87 s (see Figure 5-2), the concentric trend in the phase transition seems to be mostly caused by the temperature gradient. For a quantitative evidence of this hypothesis, the linescans in Figure 5-3(b) are reevaluated. For this, the transition times of the single points in the lateral linescans are translated into a temperature at this time in this spot, using the time dependent IR-image series. Conversion errors rise from the fact, that the pixel density in the IR-images is lower than in the optical images. In addition, the data from two similar, but yet not identical, processes are combined.

The resulting transition temperatures depending on the relative position on the four samples can be seen in Figure 5-6(b). Despite the above mentioned errors in the calculation, it becomes evident, that phase transition temperature is almost independent of the relative position on the sample within $\pm 3\,°C$. A slight offset between the PbI_2-rich, former yellow part of the sample, denoted by negative relative positions, and the CsI-rich, former brown part of the sample, denoted by positive relative positions, can be seen. While the phase transition in the PbI_2-rich part occurs at ~290 °C, the transition temperature in the CsI-rich part occurs at ~294 °C. The deviation from the compositionally independent, constant transition temperature as seen especially for the 65 °C sample, is suspected to result from the above mentioned errors due to the combination of the two different processes for the optical and the IR-imaging. No clear trend in the transition temperature depending on the T_{sub} can be seen.

Within the precision of this measurement, these results show that the transition temperature of the evaporated thin-films investigated in this work is slightly lower than for the material reported in literature, as described above.[83, 90, 116, 132] However, these reports do not state how the temperature of the transition was determined. The enormous deviation between the nominal hotplate temperature and the temperature measured with the IR-camera, as presented above, rise the question of precision of the literature values.

In addition to the dynamics of the phase transition to the black α-phase, a different nucleation behavior was seen in Figure 5-2 (page 72) in the CsI-rich and in the PbI_2 rich region of the sample. In the CsI-rich region of the sample, numerous very small black dots appear, which cover the entire area, strictly following the concentric trend as described above. In contrast, in the PbI_2 rich part of the sample significantly fewer nuclei form in comparably large distances to each other and proceed to grow until they touch each other. While single structures in the CsI-rich part of the sample are below 1 mm in size,
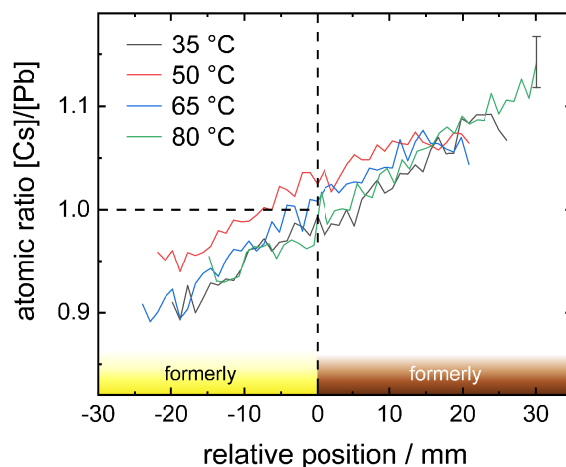
Figure 5-7: *Chemical composition from XRF dependent on the position on the sample relative to the former boundary between yellow and brown phase for samples with different T_{sub}. The atomic ratio of [Cs]/[Pb] increases linearly for all samples almost over the entire range. The point of stoichiometry is marked by the dashed lines and coincides with the optically observed, former boundary between the brown and yellow region. The errorbar is representative for all data points presented.*

the structures in the PbI_2-rich part reach dimensions of up to $10\,mm$, as can be seen in the $80\,°C$ sample. However, due to the anisotropic increase in temperature no trend in the nucleation depending on T_{sub} or the composition can be found. The morphology of the annealed samples will be investigated by SEM in more detail (see Section 5.5).

While CsI and PbI_2 are evaporated at ~$460\,°C$ and ~$230\,°C$ in vacuum, respectively, they are not expected to evaporate in large amounts at around $330\,°C$ at atmospheric pressure. Nevertheless, the constant phase transition temperature, independent of the relative position on the sample, rises the question, if the composition of the sample has changed by evaporation of the compositional excess CsI and PbI_2.

5.3 Elemental Composition

XRF measurements were performed to investigate, if the chemical composition of the samples was changed by the annealing step. These measurements were performed in line scans, along the compositional gradient, as already described for the as-deposited films in Section 3.2. Although no visible boundary between the CsI-rich and PbI_2-rich part of the film exists any more, the position on the samples will still be given relative to the former boundary for all following measurements to allow an easy comparison between the measurements and between the samples with different T_{sub}.

The results of the XRF-scan for the four samples is shown in Figure 5-7. The [Cs]/[Pb]

atomic ratio extracted from these line scans increases linearly over the relative position on the sample. This linear trend was already observed in the line scans on the as-deposited samples (see Figure 3-2 on page 35). The averaged atomic ratio of the four samples at the estimated position of the former boundary between the two regions is slightly shifted towards stoichiometry from $[Cs]/[Pb] = 0.97$ in the as-deposited films to 0.99 for the annealed films. This would mean a slight loss of Pb or PbI_2 during the annealing. Although this change is in the order of the estimated error of the measurement, the consistent shift of the compositions of all four samples hint towards a change in the composition by the annealing step. However, for evidential proof of this change, more measurements are required.

5.4 Crystal Structure

In earlier reports in the literature the crystal phase, that remained metastable after the annealing process, was claimed to be the black cubic α-phase.[44, 115, 116] In more recent reports however, it was demonstrated, that even by quenching of the annealed samples, the films do not remain in the black α-phase, but undergo a transition to the aforementioned brown orthorhombic γ-phase.[69, 113, 133, 134] Since the setup used for the annealing did not allow in-situ measurements of the crystal structure during the annealing, only the state of the crystal structure after the quenching can be reported. The measurements were conducted in the same way, as already described for the as-deposited samples in Section 3.3. The result of the measurements of the four samples can be seen in Figure 5-8. For easier comparison, the background of the measurement was fitted by a polynomial and subtracted. Comparison with reference patterns yields, that all four samples are present in the γ-phase.[69] The differences in the texturing of the samples dependent on the T_{sub} as seen for the as-deposited samples (Figure 3-7) are significantly reduced. Although the measurements are performed in the Θ-2Θ-geometry, which is prone to the influence of texturing, most of the peaks for the orthorhombic phase can be seen for all of the samples. The reduced texturing of the samples, as compared to the as-deposited films, can also be seen in the decrease of the intensity of the main peaks, since less crystallites are in the required orientation to contribute to this reflex. As a result the signal-to-noise ratio of the samples is significantly decreased, which makes a detailed analysis of patterns challenging and increases the uncertainties of the results.

With increasing T_{sub} two peaks at ~12° seem to rise. The low signal-to-noise ratio, however, makes it difficult to distinguish, to which extend this rise is promoted by an inconvenient background subtraction or a true effect of the different T_{sub}. Comparison of the suggested peak position with reference patterns reveals, that the peaks could indicate
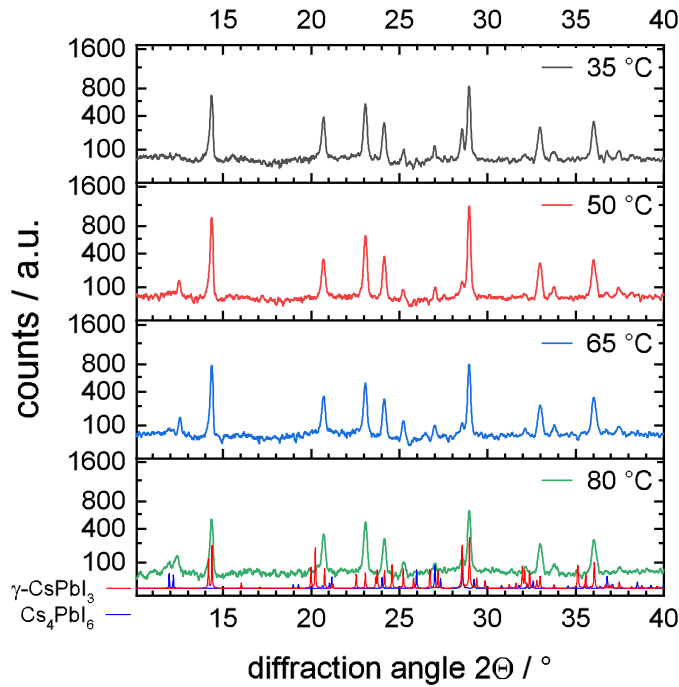
Figure 5-8: *XRD patterns for four samples with different T_{sub} after an annealing step. The calculated reference patterns below the measurements reveal, that the crystal structure of the annealed samples is the brown γ-phase. Hints for the presence of the very CsI-rich Cs_4PbI_6 can be found for $2\Theta \approx 12°$.*

a segregation of the very CsI-rich Cs_4PbI_6-phase. This would support the observation from the XRF line scans, that small amounts of Pb or PbI_2 might have evaporated during the annealing process, thus leaving a film with increased integral CsI content.

Since the measurement of the crystal phase had to be performed ex-situ, it cannot be excluded, that the black α-phase, which forms on the hotplate, remains stable for several minutes after quenching. On the timescale of hour, however, these measurements once again deliver clear evidence, that the meta-stable perovskite phase observed at room temperature is the brown orthorhombic γ-phase.

5.5 Surface Morphology

SEM images were recorded to investigate, how the phase transitions during the annealing step influence the morphology of the samples. Although the evaluation of the XRD patterns did not allow an estimation of the domain size, the altered texturing of the annealed sample as compared to the as-deposited samples suggests an extensive recrystallization.

As described above, the PbI_2-rich, former yellow part of the samples had already transformed back to the yellow δ-phase before the beginning of this measurement. Therefore,

the images reported for the PbI_2 rich part of the samples document the status of the sample after this degradation. It cannot be deduced, if the changes in the morphology occurred during the annealing process or during the degradation.

The images of the fours samples, which were acquired with two different detectors, are shown in Figure 5-9. In both regions and for all of the samples, the sizes of the grains is increased substantially as compared to the as-deposited samples. While the grain sizes in the former brown part of the samples were in the order of $100\,nm$, the size of the grains in the annealed samples is in the order of µm. In the images, which were detected by the InLens-detector, dark spots with bright boundaries stand out, which have a diameter of ~$500\,nm$. These dots are located at the grain boundaries of the larger grains. While a segregation of CsI was seen in the SEM images of the as-deposited film, the segregation in the annealed samples has a different appearance. This is in agreement with the XRD patterns, which suggested the occurrence of Cs_4PbI_6 segregations. In combination with the increased [Cs]/[Pb] ratio seen by XRF, it seems likely, that these small grains are the
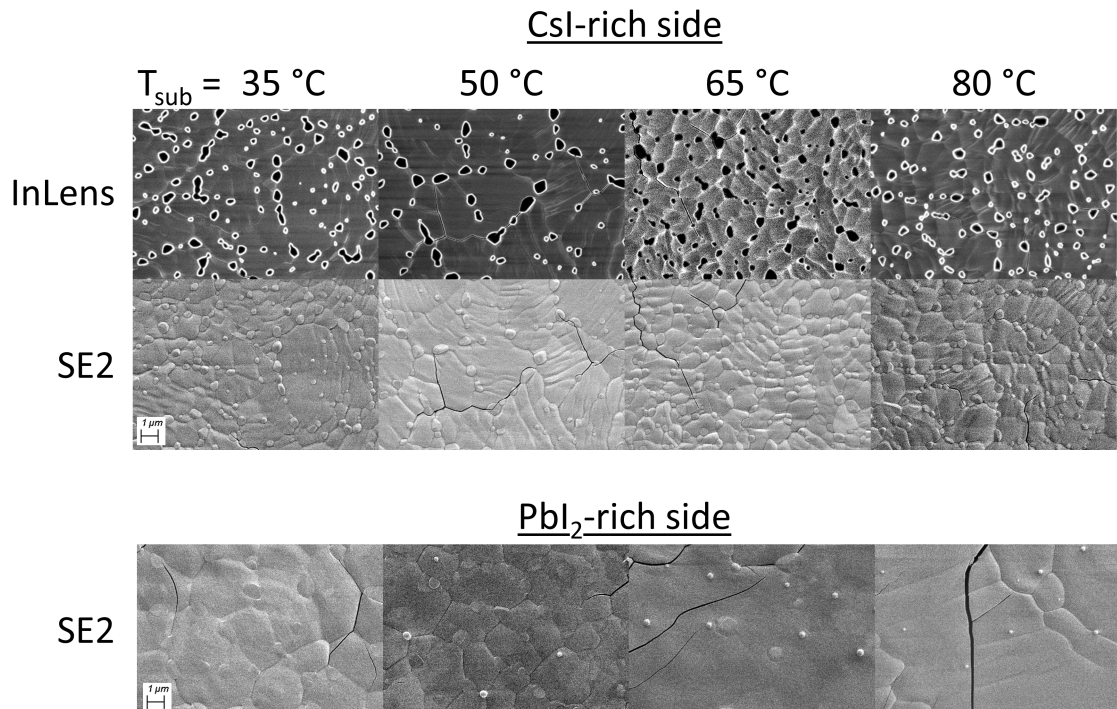
Figure 5-9: *SEM images of four samples with different T_{sub} after annealing, taken with an InLens and a secondary electron detector. The scale bar represents a distance of $1\,\mu m$. The images in the top were taken in the CsI-rich part of the sample and show grains with diameters of several µm. In the InLens detector, dark spots with very bright boundaries can be seen with a diameter of around $500\,nm$. The images on bottom were taken in the PbI_2-rich part of the sample and exhibit significantly larger grains, which partially exceed the size of the image.*

very CsI-rich Cs_4PbI_6-phase. On the PbI_2-rich side of the sample, no segregation with such appearance could be found in the InLens detected images, giving further evidence for this hypothesis.

In the images in the CsI-rich region, which are acquired with the secondary electron detector, the segregation appears to be embedded in the main layer. Thus, it cannot be distinguished, whether the segregation can only be found on the surface of the sample or throughout the bulk of the material.

On the PbI_2-rich side of the sample, the grain size is in the order of $1\,\mu m$ for the as-deposited films. After the annealing and the subsequent re-transition to the yellow δ-phase, the size of the grains has increased to several µm. In the images for the $65\,°C$ and $80\,°C$ samples, the grain size is even above $10\,\mu m$ and exceeds the range covered by the image. As described above for the brown part of the sample, no clear evidence for a trend in the grain size depending on T_{sub} can be found. The needle-like structures as seen in the as-deposited samples in the PbI_2-rich region have vanished. The surface is very smooth over the entire image section, apart from wide cracks, that traverse the layers. Since the phase transitions are accompanied by changes of the unit cell volume,[69] the cracks might originate from the repeated phase transitions, especially in this part of the sample.

These observations about the very different grain sizes in the CsI and PbI_2-rich parts of the sample, respectively, are in well agreement with the in-situ imaging of the annealing process, in which significantly larger nucleations could be found in the PbI_2-rich, former yellow part of the sample.

5.6 Optoelectronic Properties

The optoelectronic properties of the samples were measured after the annealing step to investigate the influence of the recrystallization on these parameters. As mentioned above, the measurement of optical transmission and reflection is the only measurement, that could be taken, while the entire samples were still in the brown phase. During the measurement of the PL the samples degraded, so that the measurement could only be conducted in the CsI-rich part of the sample, which remained in the γ-phase.

Optical band gap

The absorption onset of the films was determined by UV-Vis measurements, which were performed in inert atmosphere with the setup described in Figure 2.2. As for the as-deposited films, the measurements on the annealed films were performed as line-scan with a step-size of $1\,mm$ and on all four samples in order to investigate, the dependence of the

band gap on the samples composition and T_{sub}. Single spectra extracted from this scan on the 65 °C sample, which were taken in the PbI_2-rich and CsI-rich region, respectively, are shown in Figure 5-10(a) as an example. Comparing these two measurements, the most prominent difference is the amplitude of the thin-film interference fringes in the transmission and reflection signal. In combination with the slightly increased overall reflection of the spectrum taken in the former yellow region, this indicates an increased surface roughness in this area. Considering the results from the SEM images, the increased roughness might be caused by the increased grain sizes. Comparing the two single measurements for the annealed samples as presented here, with the single measurements on the as-deposited films as reported in Figure 4-1 (page 56) this increased roughness can also be seen in between the spectra taken in the CsI-rich, former brown, part of the sample. The weak absorption onset at ~430 nm that was observed in the as-deposited films, can be found in the annealed samples as well. The transmission spectra for both positions on the sample reveal a distinct increase in the signal at this wavelength. In the reflection spectra the signal-to-noise ratio decreases significantly at this wavelength, thus making it difficult to find strong evidence for this absorption onset in the calculated absorption signal. More precise measurements with improved signal-to-noise ratio at this wavelength have to be performed to confirm the presence of the absorption edge. If these measurements confirm
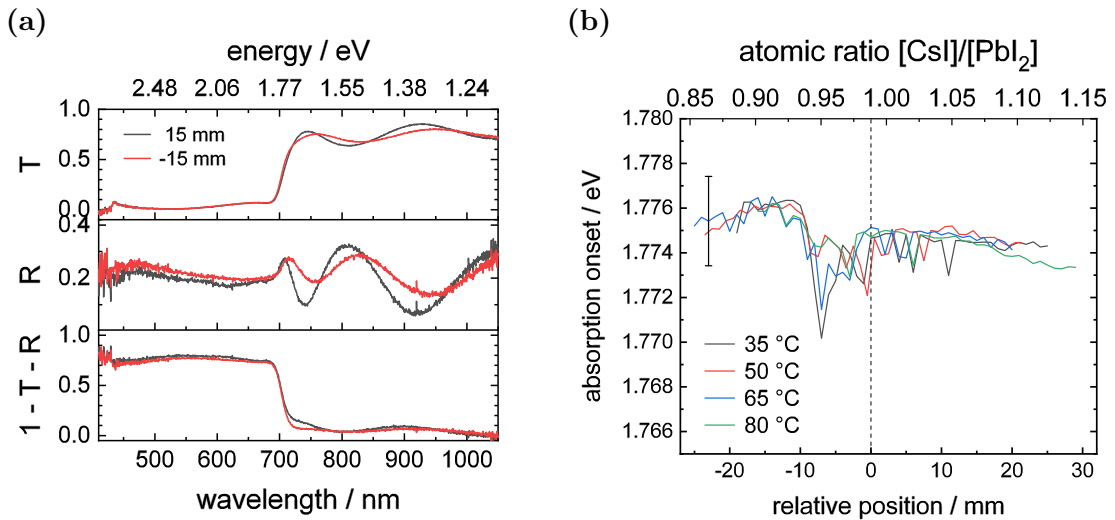
Figure 5-10: *(a) Transmission, reflection and absorption spectra at different relative positions, extracted from a UV-Vis line scan on the $T_{sub} = 65$ °C sample after annealing. The reflection signal for wavelength below the band gap as well as the amplitude of the interference fringes in the transmission and reflection are slightly increased in the former yellow part of the sample as compared to the former brown part, suggesting an increased surface roughness in that region. (b) Absorption onset over the relative position on the sample as extracted from the UV-Vis line scan. Within the precision of this measurement, the onset is almost constant over the entire width of the sample.*

the presence of this absorption edge, the hypothesized thin layer of yellow δ-CsPbI$_3$ can not be converted into the brown γ-phase by annealing at the temperatures reported here. The presence of this insulating layer would make the fabrication of devices with high open circuit voltages challenging.

The main absorption onset of the material was calculated from the UV-Vis measurements by determining the inflection point of the absorption coefficient as already described for the as-deposited samples. The results of these calculations for the linescans on all four samples is shown in Figure 5-10(b). The absorption onset is almost constant for all samples. There is a slight offset of ~1.5 meV between the absorption onset in the PbI$_2$-rich former yellow region and the CsI-rich former brown region of the sample. This difference, however is within the margin of error of this measurement.

Comparison of the values for the different samples yields, that the absorption coefficient after the annealing is independent of T$_{sub}$. Within the precision of the measurement, the absorption onset is identical for all four samples over the entire region of the sample.

PL-Imaging

Absolute calibrated PL imaging was measured on the annealed samples to investigate the influence of the annealing step on the recombination of excited charge carriers. The measurements were performed in the same setup, that was used to measure the as-deposited films. After fitting the energy dependent PL images, the energy of the maximum of the PL (PL$_{max}$) as well as the external PL quantum yield (PL QY) are extracted spatially resolved, as described in Section 4.2. The results of these calculations for the 65 °C sample are depicted in Figure 5-11(a) and Figure 5-11(b), respectively, as an example. The measurements show a clear dependency of the PL$_{max}$ on the x-position, which is parallel to the compositional gradient of the samples. In the direction perpendicular to the gradient only minor changes can be seen, which can partially be attributed to artifacts from the edges of the samples. Since the image is taken close to the edge of the sample, the spot at ~20 mm in x-direction and ~8 mm in y-direction, which shows an increased PL$_{max}$ as compared to the surrounding area, could be an artifact from altered chemical composition due to shading effects during the evaporation.

In the bottom half of the image distinct features with lowered PL$_{max}$ as compared to the surrounding material can be seen. These features could be determined to be the substrate identification number, which is scratched on the back side of the substrate. It has been simulated, that changes in the substrates roughness can result in a changing PL$_{max}$ due to differed energy dependent reflections on the substrate.[135] These reflections also
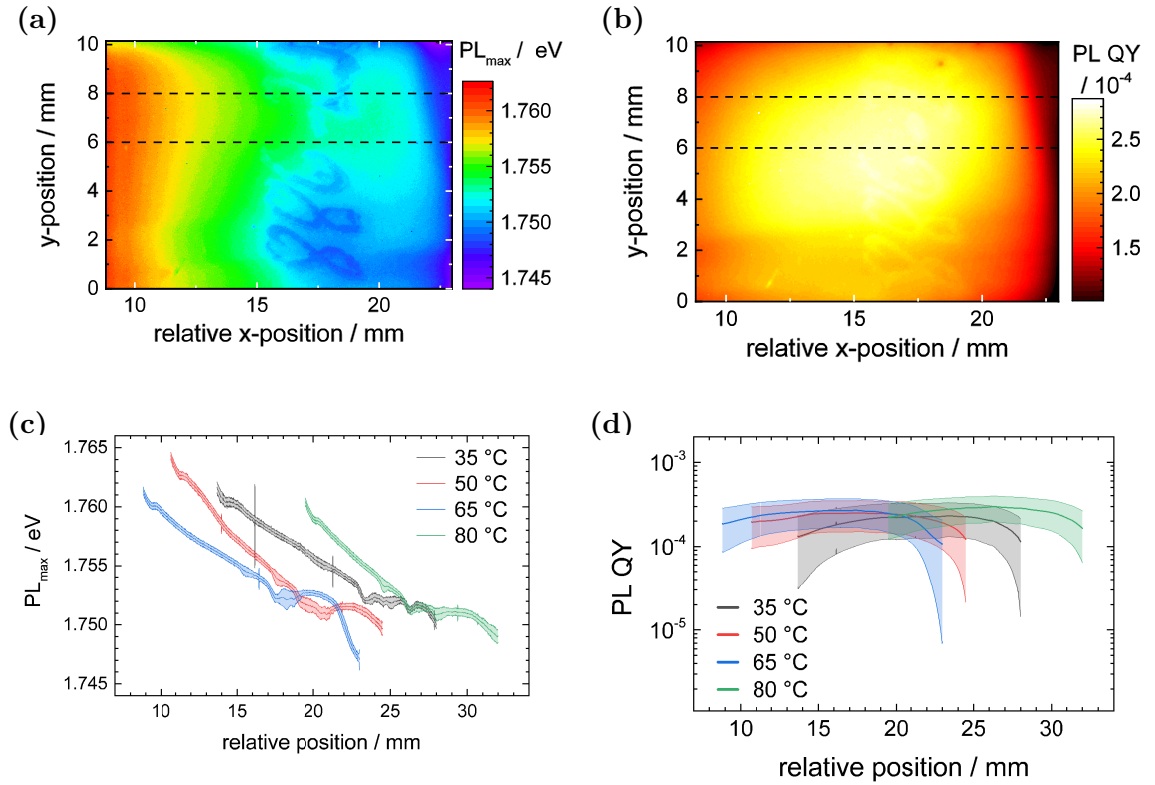
Figure 5-11: *PL parameters extracted from a Gaussian fit of the hyperspectral PL imaging on the 65 °C sample. (a) and (b) PL_{max} and external PL QY, respectively, depending on the lateral position on the sample. While the PL_{max} shows a steady trend in the x-direction, parallel to the compositional gradient of the sample, the PL QY shows a bright spot in the center of the sample with decreasing intensity in all lateral directions. (c) and (d) show line scans, which were extracted from the two dimensional images by averaging over a representative range in the y-direction. The area used for the averaging in the 65 °C sample is indicated in (a) and (b) by the horizontal dashed lines.*

contribute to a different intensity of the PL, resulting in artifacts in the PL QY. This can be seen in increase values of the PL QY in the same area in the image in Figure 5-11(b).

The distribution of the PL QY is reminiscent of the distribution observed for the as-deposited samples. A bright spot is visible in the center of the image, that descends in both lateral directions over a factor of two. As already described for the as-deposited sample, this distribution is assumed to be an artifact from inhomogeneous illumination of the sample. The result of the PL quantum yield can therefore only be considered as a order of magnitude.

For a more quantitative analysis of the data, linescans were extracted from the images by averaging over a representative range in y-direction. The y-position range for 65 °C sample, over which was averaged, is indicated by the dashed lines in Figure 5-11(a)

and Figure 5-11(b). The results of likewise averages for all four samples are shown in Figure 5-11(c) for the PL_{max} and in Figure 5-11(d) for the PL QY. All samples were measured at the most CsI-rich edge of the samples.

The PL_{max} decreases with increasing relative position, and thus increasing CsI-content in the film, for all four samples, while roughly ranging between $1.750\,eV$ and $1.763\,eV$. All samples show a slightly increased noise-signal close to the respective maximal relative position, which can be assigned to the aforementioned artifacts from the batch number. The offset in the relative position between the measurements stems from the fact, that the compositions of the samples are slightly different, thus resulting a lateral shift of the stoichiometric boundary. Beside this shift, the samples show a very similar trend in decreasing PL_{max}. Therefore, this trend seems to depend mainly on the absolute position in respect to the edge of the sample, rather than on the relative position, which is determined by the composition. Thus, the value of PL_{max} in the annealed samples can only be given independent of the composition with $(1.755 \pm 0.010)\,eV$.

As the spatially resolved PL QY is also strongly affected by the inhomogeneous illumination, as stated above, the extracted line scan in Figure 5-11(d) is given with large error-bars as well. However, comparison with the values measured on the as-deposited samples (see Section 4.2) yields, that the annealing procedure significantly increased the PL QY. While the QY of the as-deposited samples was ranging between $3 \cdot 10^{-6}$ and $3 \cdot 10^{-5}$, the values for the annealed samples are above $1 \cdot 10^{-4}$ over the entire compositional range investigated here. This shows, that the annealing procedure improves the quality of the absorber by lowering the non-radiative recombination.

6

Degradation Causes and Principle

During the conduction of the experiments reported above, a rapid degradation of the samples was observed, when exposed to ambient air. The degradation shows in a change in color, turning the sample from brown into yellow, while it remained unclear if it was caused by oxygen, humidity or the combination of both. The mixed organic-inorganic perovskites are known to chemically decompose under the influence of ambient atmosphere.[56, 57, 136, 137] For the fully inorganic $CsPbI_3$ perovskites, however, literature suggests that underlying process is a phase change from the brown γ-phase into the yellow δ-phase.[44, 46, 49, 138, 139] In this section the degradation process is studied in-situ by time resolves XRD as well as by optical reflection.

6.1 In-Situ Monitoring of the Crystal Structure During Degradation

The crystal structure of the $CsPbI_3$ thin-films was recorded time resolved during the degradation to investigate the changes in the crystal structure and verify the nature of the degradation reported in literature. For this, inch-by-inch sized samples with $T_{sub} = 50\,°C$ and a nominal chemical composition of $[CsI]/[PbI_2] = 1.05$ in the center were exposed to atmospheres with a constant temperature of ~20 °C but different relative humidities in different gasses. A schematic drawing of the setup is depicted in Figure 6-1. The dry inert gas is guided through a hot water bath and thus humidified and subsequently passes a cooling column. By cooling the gas, the absolute humidity decreases to the maximum possible relative humidity at the given temperature. The cooling column is connected with the degradation setup via a ~10 m long tube, which allows the gas to heat up to room
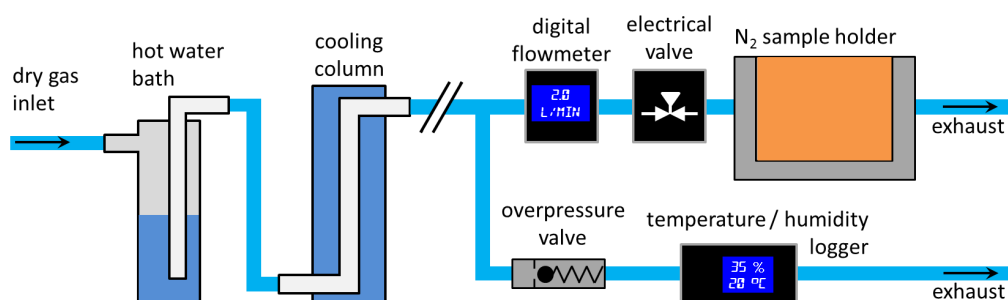
Figure 6-1: Schematic drawing of the setup used for the generation of a humidified atmosphere for XRD in-situ-measurements during the degradation. Dry gas is guided through a hot water bath for humidification and, subsequently, through a cooling column for well defined dehumidification. Two pathways exist for the humidified gas. The first is closed before the start of the experiment and leads through a digital flowmeter, an electrical valve and the sample holder. The second is used for conditioning and probing the atmosphere and leads through an overpressure valve and a temperature and humidity logger.

temperature again. During this process, the absolute humidity remains constant, while the relative humidity decreases. By adjusting the temperature of the cooling column, the relative humidity in the gas, that is used for the experiment, can be adjusted.

The sample is placed in the sample holder within a nitrogen filled glove box, as described in Section 2.2. For a defined start of the experiment, the inlet of the sample holder is equipped with an electrical valve, which is closed at the beginning. Thus, the humidified gas flows though a second pathway, which is equipped with an overpressure valve and a temperature and humidity logger (*testo 175 H1*). Using that pathway, the temperature of the cooling column is adjusted and the tubing of the experiment is flushed, until the the logger constantly reads the required humidity.

Subsequently, the continuous acquisition of XRD patterns is started and the electrical valve is opened to start the experiment. The gas flow can be read from a digital flowmeter, which is mounted before the electrical valve. Owing to the overpressure valve, the second pathway is closed now, sending the gas through the sample holder and thereby exposing the sample to the respective atmosphere.

For the time series, diffraction images were taken with an integration time of $3\,\mathrm{s}$ to compromise between temporal resolution and signal-to-noise ratio. Reference patterns were acquired before and after the degradation experiment with an integration time of $120\,\mathrm{s}$ for improved data quality, which allows a more detailed analysis of the crystal structure. The 2D reference images taken before and after the degradation experiment, respectively, are shown in Figure 6-2. For the visualization of the images, the background was removed by FFT-high pass filtering, which leads to the artifacts at the boundaries between the
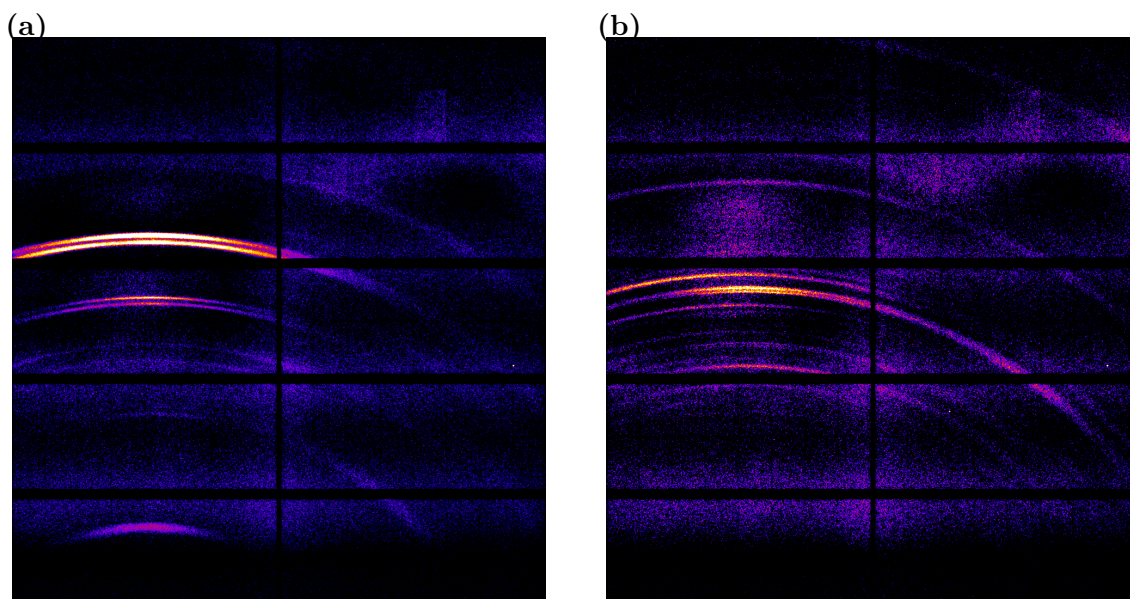
Figure 6-2: *2D diffraction images which were taken (a) before and (b) after the degradation with an integration time of* $120\,\text{s}$. *The background from stray radiation was removed for the presentation of the images, which causes artifacts at the boundaries between the single detector panels. Both images show concentric diffraction rings around the incident beam, which is not visible within the range of the images. The diffraction patterns in the two images are distinctly different, which illustrates the change of the crystal structure during the degradation. The intensity of the rings shows a stronger azimuthal dependency in (a) than in (b), which indicates a stronger texturing of the sample before the degradation.*

single detector panels. For the quantitative analysis described below, this background removal was not performed.

The diffraction reflexes are visible as sectors of concentric circles around the incident beam, which is outsides of the range of the detector. Especially in the image taken before the degradation (Figure 6-2(a)), the intensity of the diffraction rings decreases strongly apart from the vertical axis and vanish at the right side of the image for most of the reflexes. Some reflexes, however, appear only in this off-axis area of the image. This indicates a texturing of the samples, as it was already observed in the laboratory measurements, described in Section 3.3. In the reference image taken after the degradation (Figure 6-2(b)) the dependency of the intensity of the rings on the azimuthal angle is less pronounced, indicating less texturing in this material. By comparing the reference image taken before and after the degradation it becomes evident, that the material undergoes a phase transition during the degradation.

For the evaluation of the diffraction images, the reflexes were quantified by circular integration. At this point, the evaluation of the diffraction images was performed with a focus on the identification of the crystal phase for different times during the annealing. There-

fore, the integration was performed for a single, fixed azimuthal range of φ between $-20°$ and $20°$, although integration for a set of different azimuthal ranges can yield additional information about the texturing of the sample. The center of the rings was determined with an additional image, for which the detector was shifted downwards in the plane by a known distance, so that the primary beam was visible. To allow the calculation of the angle, under which the diffraction rings occur on the detector, the detector–sample distance was measured. The distance was then refined by comparison of characteristic peak positions with known positions from reference patterns.

Figure 6-3 shows the integrated patterns before and after the degradation, which were extracted from the 2D-images in Figure 6-2. The reference patterns, which were used for the angular calibration and were taken at the synchrotron as described in Section 3.3, are shown as well. For easier comparison of the patterns acquired with this setup to patterns reported above, the diffraction angle was translated into the diffraction angles as they would occur at the Cu K-α-energy (see Section 2.2). However, both patterns are strongly affected by the non-monochromatic spectrum of the metal-jet X-ray source as shown in Figure 2-5. This manifests in "shadow" peaks at lower angles, which are marked with an asterisk in the patterns.

Comparison of the measurement before and after the degradation with the reference measurements yields clear evidence, that the degradation is a phase transition from the
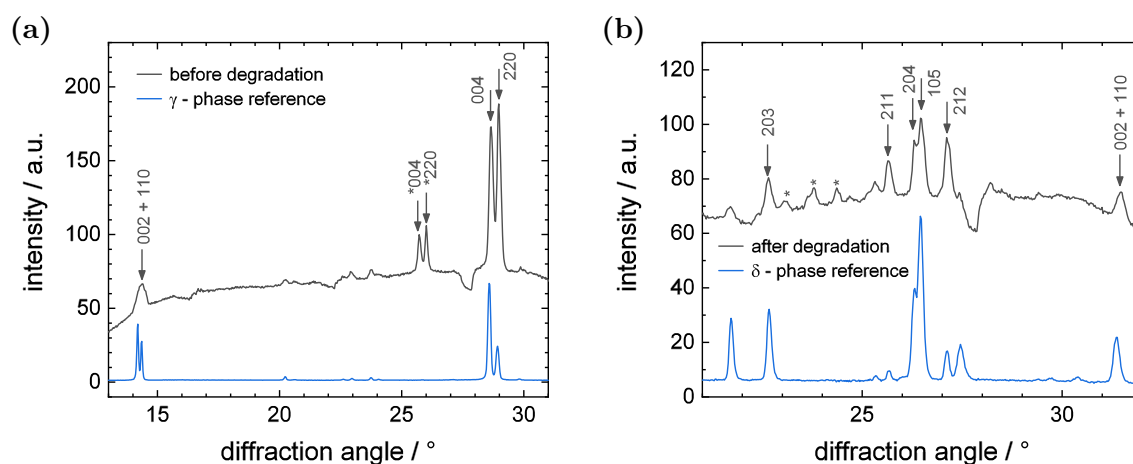
Figure 6-3: Diffraction patterns for (a) before and (b) after the degradation as obtained from circular integration of the 2D-diffraction (black). Peaks marked with the asterisk (*) result from a non-monochromatic incident radiation. The peaks with assigned hkl-indices were used for quantification of the phase. The dips in the patterns at around $16°$, $22°$ and $28°$ stem from artifacts due to the gaps between the detector panels. For comparison, reference measurements of the brown γ-phase and yellow δ-phase of $CsPbI_3$ are plotted (blue), which were taken at the synchrotron and were reported in Section 3.3. These references confirm, that the crystal phase before and after the degradation are the brown γ-phase and the yellow δ-phase, respectively.

brown γ-phase to yellow δ-phase. For both measurements all visible peaks can be assigned to diffraction reflexes from the respective CsPbI$_3$ phase. However, due to the limited signal-to-noise ratio and the peak broadening at angles, which do not fulfill the Θ-2Θ-condition for the constant incident angle, the presence of secondary phases cannot be excluded.

With these static measurements, the crystal structure of the films before and after the degradation can be identified, while the actual process during the degradation remains unknown. Evaluation of the time series, which was recorded during the degradation, illuminates this process. Degradation experiments were performed in different atmospheric conditions to investigate the influence of moisture and oxygen. Therefore, the continuous measurement was started, while the sample was still in dry nitrogen atmosphere. At a specific time, the flow of the humidified gas was started by the electrical valve. This time is referred to as t = 0 s.

Two examples for the time resolved XRD-patterns at different atmospheric conditions are shown in Figure 6-4. Both measurements show the transition from the brown γ-phase to the yellow δ-phase without any visible intermediate stage. The transition occurs on different time scales for the two processes with different relative humidity. The transition in air with ~(60 ± 10) %rh shows a slow transition over more than one minute, during which the two phases partially coexist within the interaction volume of the X-rays. In contrast, the degradation in (95 ± 10) %rh nitrogen proceeds within a few seconds. For both transitions, the degradation starts with an angular shift of all diffraction peaks towards lower
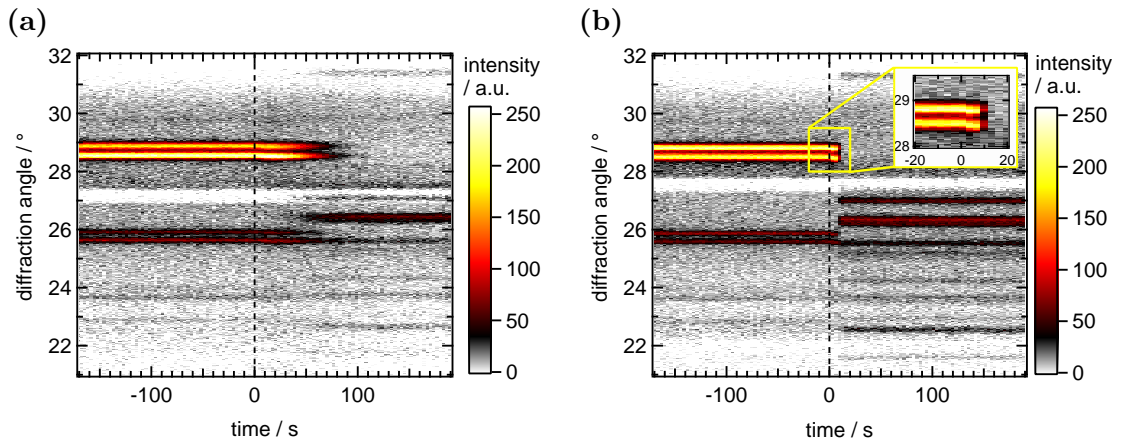
Figure 6-4: Time series of circular integrated diffraction images recorded continuously with $3\,\mathrm{s}$ integration time. (a) shows the degradation of the thin-film in air with ~(60 ± 10) %rh, (b) shows the degradation in nitrogen with ~(95 ± 10) %rh. A single phase transition without intermediate stage is visible in the patterns. While the degradation takes over one minute in (a), the process is completed within a few seconds in (b). In both cases an angular shift is visible in all peaks before the transition, which is magnified in the inset in (b).

angles, before the decay in intensity of the peaks is observed. Without further analysis, these measurements prove, that the oxygen is not necessary for the degradation. While an influence of oxygen on the degradation kinetics cannot be excluded, it shows, that the presence of humidity alone is sufficient to trigger the degradation process.

For a more quantitative evaluation of the time series, the most distinct diffraction reflexes of both phases were fitted with Gaussian functions to track the integral intensity and position of each reflex over time. Since the integration time for the patterns of the time series was significantly shorter than for the reference measurements depicted in Figure 6-3, not all peaks visible in the references could be tracked in the time series. The peaks used for the tracking are labeled with the hkl-indices in Figure 6-3.

The integral intensity for all tracked reflexes of the respective phase were summed up and normalized to quantify the phase transition. The phase transitions for the two degradation processes described above are shown in Figure 6-5 along with two more degradation processes at different atmospheric conditions. All four processes show an exponential transition between the two phases, which starts after a short delay. The transition time as well as the delay before the transition depend on the relative humidity of the gas. As already observed above, no significant difference between processes with humidified nitrogen and humidified air can be observed. For all samples the time τ after opening the valve was determined, for which the intensity of the brown γ-phase peaks had decayed to $1/e$. Comparing these numbers the dependence of the degradation time on the humidity seems to be exponential, although the process in nitrogen with $(35 \pm 10)\,\%$rh deviates from that trend. A more detailed study of the causes and kinetics of the degradation was performed with in-situ optical reflection measurements and will be presented in Section 6.2.

For the investigation of the angular shift, the position of the reflex is averaged in the measurements before the start of the process and subtracted from the current reflex position for each time step. This results in an absolute angular shift for each reflex. The angular shifts during the four degradation processes are depicted in Figure 6-6. For all four processes the expected angular shift is visible after switching the gas flow on. Since the shift does not differ for the individual reflexes of a measurement within the level of noise, an averaged peak shift is calculated for an improved signal-to-noise ratio. This exhibits, that the peaks show a rapid shift towards lower angles immediately after the start of the gas flow, which is followed by a slower shift towards higher angles again. The comparison of the peak shifts for the four processes reveals, that the magnitude of the peak shift weakly depends on the relative humidity. However, the shift occurs significantly faster for increased relative humidity values.

(a)

(b)

(c)

(d)
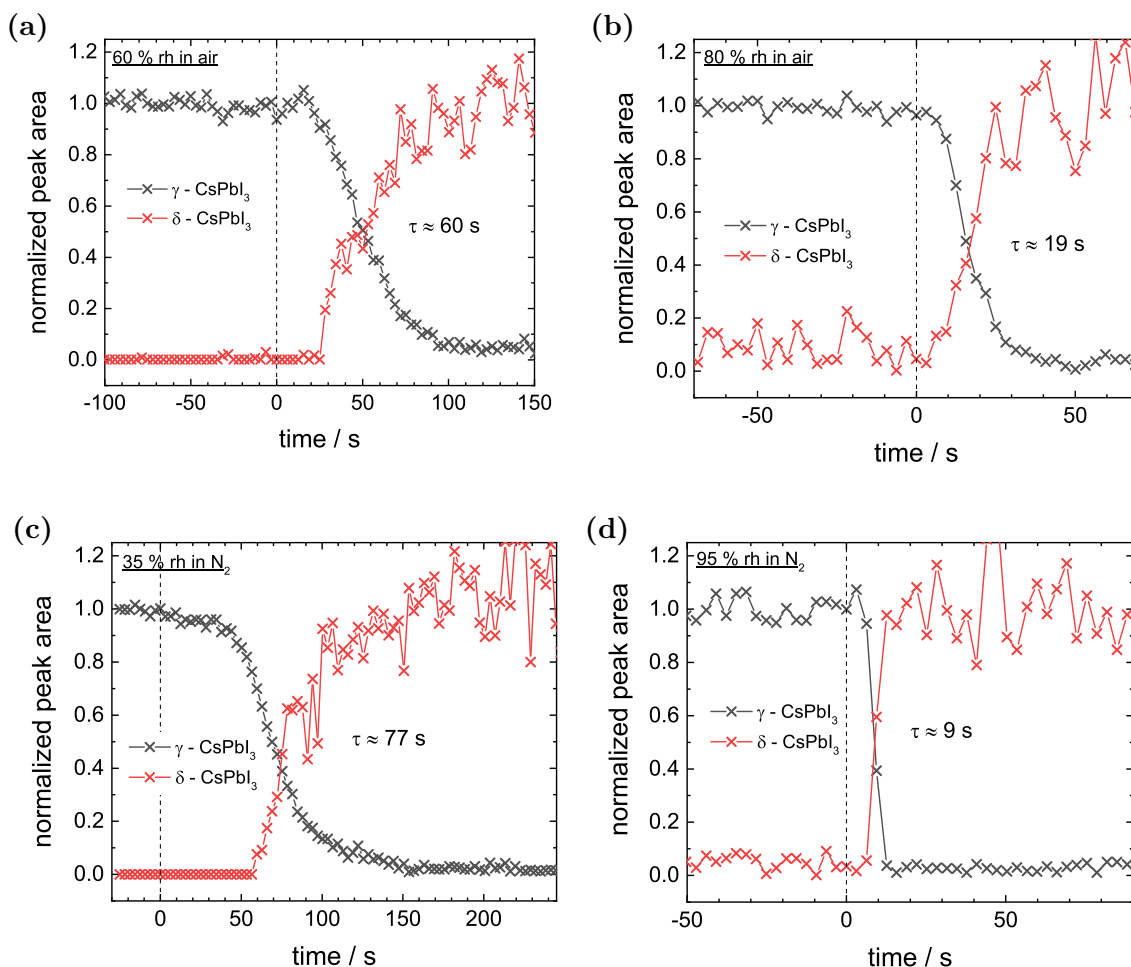
Figure 6-5: *Normalized integral peak intensity for the brown γ-phase and yellow δ-phase, respectively, extracted from the XRD-time series. The samples remain in dry nitrogen atmosphere until $t = 0$ and are exposed to different humidified atmospheres, respectively. After a short delay, an exponential phase transition can be observed for all four processes. The delay time as well as the transition time depend on the humidity. τ is defined as the time after the start of the gas flow, at which the intensity of the brown γ-phase has decayed to $1/e$.*

In general, an angular shift could either originate from a very slight tilting of the sample, which might be cause by the commencing gas flow, or from an expansion of the crystal lattice, which might be caused by the interaction with water molecules. A tilting of the sample, however, should not depend on the humidity. The dependence of the dynamic and magnitude of the peak shift on the humidity rather suggest a lattice expansion as origin for the peak shift.

(a)

(b)

(c)

(d)
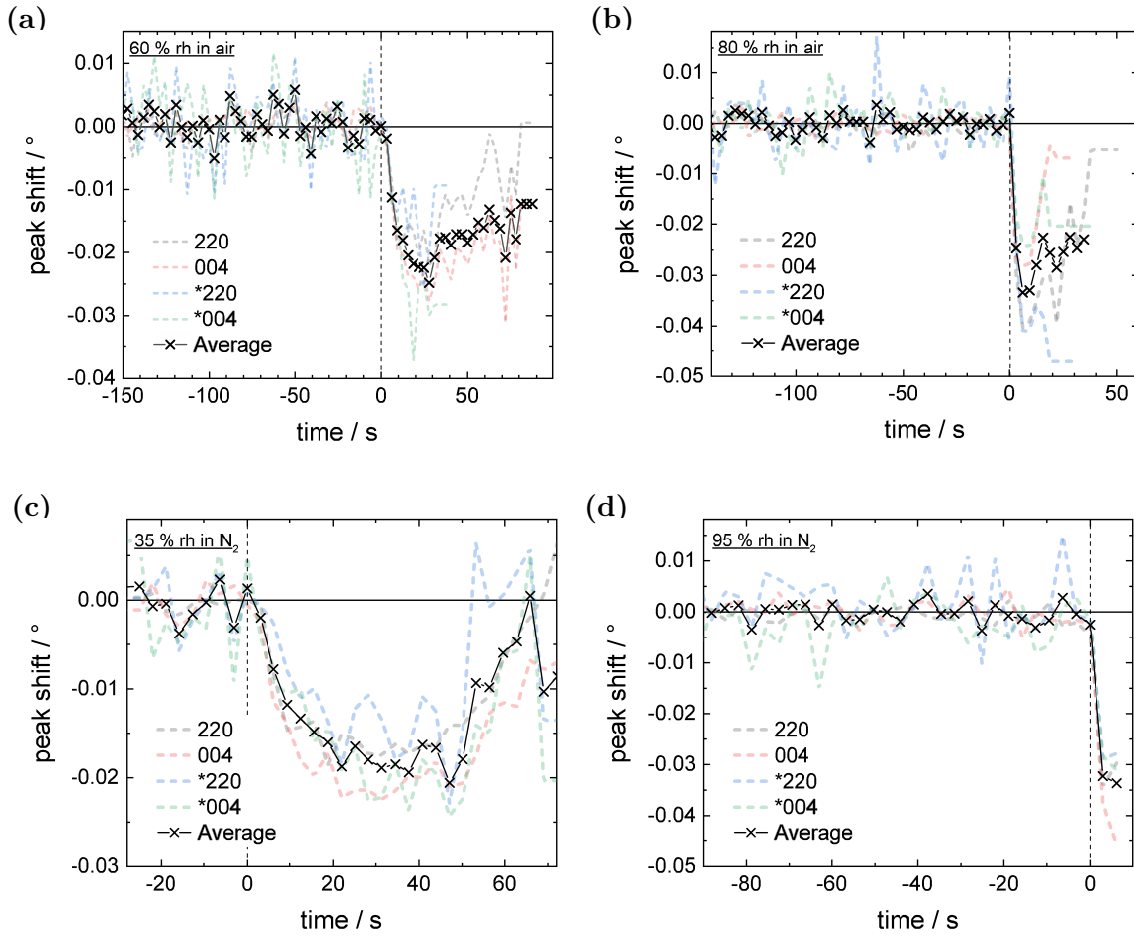
Figure 6-6: *Angular peak shift of different diffraction reflexes (hkl) of the brown γ-phase during the degradation in different atmospheric conditions. An averaged shift of the four peaks is given to improve the signal-to-noise ratio. The magnitude of the peak shift seem to depend weakly on the relative humidity and is between $0.02°$ and $0.03°$ for all four processes. The dynamics of the peak shift vary drastically for the different humidities. Note the different scales of the time axis.*

6.2 In-Situ Reflection Imaging during Degradation

For a more comprehensive study of the influence of the atmospheric conditions, T_{sub} and the chemical composition on the degradation dynamics, in-situ reflection imaging was recorded time resolved. A humidity chamber (*electro-tech systems Inc.*) was used to generate an atmosphere with defined temperature and relative humidity. For a precise measurement of the atmospheric condition, a temperature and humidity logger (*testo 175 H1*) was used. For the experiments reported here the temperature was kept constant at ~25 °C, while the relative humidity was varied. For each degradation process, the samples were placed in the humidity chamber within an airtight box. After preconditioning of the atmosphere in the humidity chamber, the continuous acquisition of reflection images was

started and the lid of the airtight box was removed rapidly to initiate the degradation process. The reflection images were recorded with a CCD-camera (*The Imaging Source DBK 41AU02.AS*) while the samples were illuminated with a white LED light source.

The samples used in this section are fabricated in the same way as the samples used in the previous sections and were evaporated at substrate temperatures of $T_{sub} = 35\,°C$, $50\,°C$, $65\,°C$ and $80\,°C$, respectively, with a compositional gradient of $[CsI]/[PbI_2]$ between ~0.9 and 1.1. Each degradation run was performed on four samples at the same time, containing one sample of every T_{sub}, to minimize the influence of fluctuations and uncertainties in the relative humidity on the degradation kinetics of each sample.

To investigate the influence of oxygen on the degradation behavior, four samples with the different T_{sub} were exposed to dry artificial air over the course of several hours. Although the artificial air contains $20\,\%$ oxygen, no change in the appearance of the samples could be observed. This indicates, that oxygen does not influence the degradation process as already suggested by the in-situ XRD measurements.

To study the influence of the relative humidity on the degradation kinetics in more detail, a series of degradation processes was conducted, in which the samples were exposed to atmospheres with $20\,\%$rh, $30\,\%$rh and $40\,\%$rh, respectively. Figure 6-7 shows single images extracted from the time series of the degradation of a $T_{sub} = 65\,°C$ sample in air with $40\,\%$ relative humidity as an example. The degradation starts at the stoichiometric boundary in the center of the sample and takes longer, as the chemical composition becomes more CsI-rich. The transition occurs in two steps. In the first step, the majority of the material
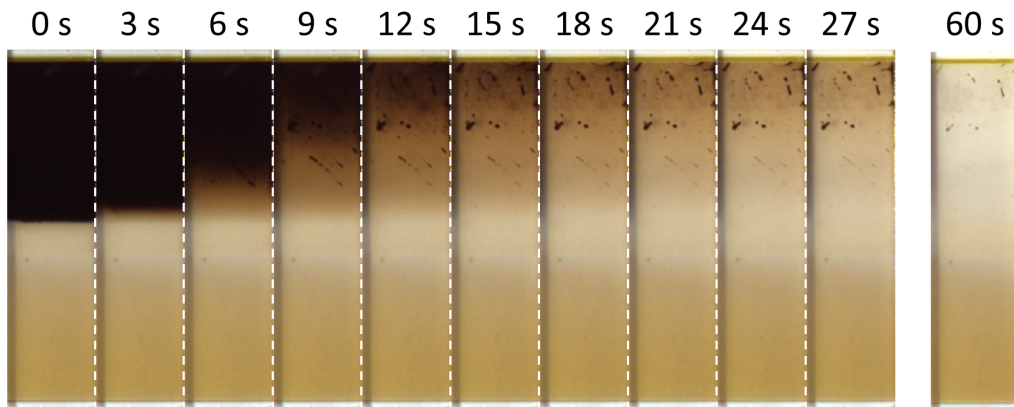
Figure 6-7: *Images extracted from a continuous reflection imaging series during the degradation of a $T_{sub} = 65\,°C$ sample in air with $40\,\%$rh. The degradation starts at the stoichiometric boundary in the center first and occurs at later times for the more CsI-rich composition in the top of the sample. The degradation occurs in two stages, where the first stage is completed after ~15 s and leaves a brown shimmer, which transforms on a significantly longer timescale.*

changes its color from the brown γ-phase towards the yellow δ-phase. However, a brownish shimmer remains in that parts of the sample, which vanishes only after a significantly longer time. The dark stains, that remain on the sample, partially even after $60\,\text{s}$, are attributed to compositional impurities.

Figure 6-8 shows two images for each T_{sub} sample during the degradation in air with $40\,\%\text{rh}$. The first is recorded at the beginning of the degradation and the second shows the sample after the first step of the degradation is completed, as described above. For all samples the degradation occurs at the stoichiometric boundary first and starts later, as the composition becomes more CsI-rich. The two steps of degradation, as described above for the $T_{\text{sub}} = 65\,^{\circ}\text{C}$ sample, can be seen for all samples. However, the shape and intensity of the remaining brown shimmer after the first step differs from sample to sample. While the shimmer in the $65\,^{\circ}\text{C}$ sample looks smooth and even, the $35\,^{\circ}\text{C}$ and $50\,^{\circ}\text{C}$ samples show a rougher and more grainy structure. The shimmer in the $80\,^{\circ}\text{C}$ sample exhibits a stripy texture. No clear trend in the apparent grain size of the shimmer could be found. Due to the limited number of investigated samples and since all samples for a given T_{sub} were evaporated in the same evaporation process, it cannot be resolved, if the different appearance of the shimmer stems from random differences in the fabrication process or actually correlates with T_{sub}.
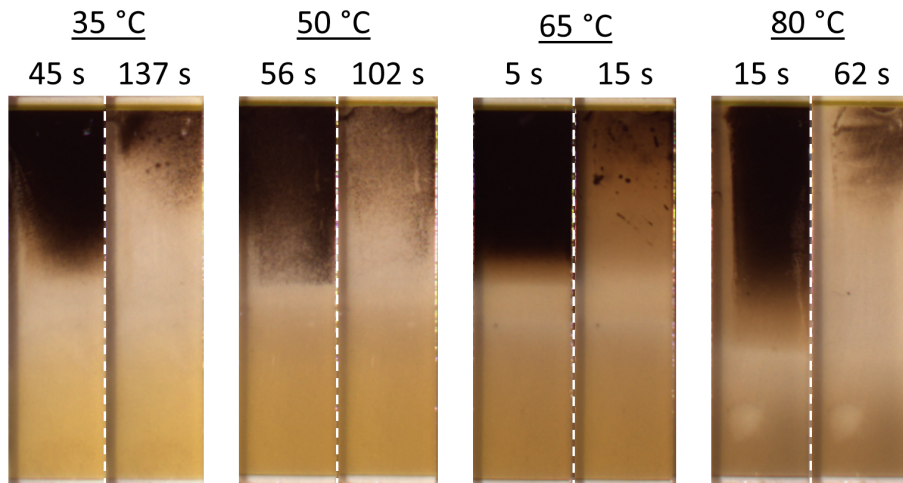
Figure 6-8: *Images extracted from the reflection imaging series during the degradation of samples with different T_{sub} in air with $40\,\%\text{rh}$. The first images for each T_{sub} show the sample at the beginning of the degradation, the second images show the sample after the first step in degradation is completed. While for all samples the degradation starts at the stoichiometric boundary in the center of the samples, the remaining brown shimmer is different in shape and intensity for all samples.*

For a more quantitative evaluation of the reflection imaging, the time of the degradation for all compositions on each of the substrates was determined. Similar to the evaluation of the in-situ imaging of the annealing process, the brightness of each pixel within the reflection images was tracked over time. For an improved signal-to-noise ratio, the brightness of each composition in each image was calculated by averaging over horizontally neighboring pixels, which represent material of the same chemical composition. The evolution of the brightness was then calculated from these averaged values and is shown in Figure 6-9(a) for one spot on the $50\,°C$ sample in $30\,\%$rh atmosphere as an example. The inflection point in the evolution is defined as the time of the degradation. After the derivative of the temporal evolution of the brightness was calculated, it was smoothed with a floating average and the local maximum was determined. This results in a degradation time for each composition on each of the four samples. Due to the aforementioned two steps in the degradation, the precision of this method is very limited, but sufficient for the comparison within this experiment. For easier analysis the resulting degradation times for the different compositions were smoothed again by a floating average along the compositional gradient.

Influence of T_{sub} on the Degradation Time

The results of the extracted lines along the chemical gradient for the four samples in $20\,\%$rh, $30\,\%$rh and $40\,\%$rh, respectively, are depicted in Figure 6-9. Unfortunately the light conditions in the laboratory changed drastically during the experiment with $20\,\%$rh after ~$120\,$min so that the experiment had to be canceled and thus does not show the full transition of the $35\,°C$ and $50\,°C$ samples. However, for all atmospheric conditions and all reported samples the degradation occurs fastest at the stoichiometric boundary in the center of the samples and slowest in the CsI-rich part of the sample, which is represented by high values of the relative position. The degradation time depends almost linearly on the chemical composition for most of the samples.

Although no consistent correlation of the degradation time on T_{sub} can be seen in all three experiments, a general tendency seems to be, that samples deposited at higher T_{sub} degrade faster than samples with lower T_{sub}. Despite some exceptions from this trend, a clear dependence of the degradation time on T_{sub} can be seen. Thus, the degradation times of the samples with lower T_{sub} of $35\,°C$ or $50\,°C$ is by a factor or 10 or even 20 higher than for the samples with higher T_{sub} of $65\,°C$ or $80\,°C$. As an example, the $80\,°C$ sample in $30\,\%$ relative humidity was completely degraded after $1.5\,$min, while the $35\,°C$ partially remained in the brown γ-phase even after $40\,$min.

Influence of the Relative Humidity on the Degradation Time

To outline the influence of the relative humidity on the degradation time, the transition times reported above are shown in Figure 6-10 sorted by T_{sub} for the different relative humidities. As stated above, the degradation process at 20 %rh was affected by changing
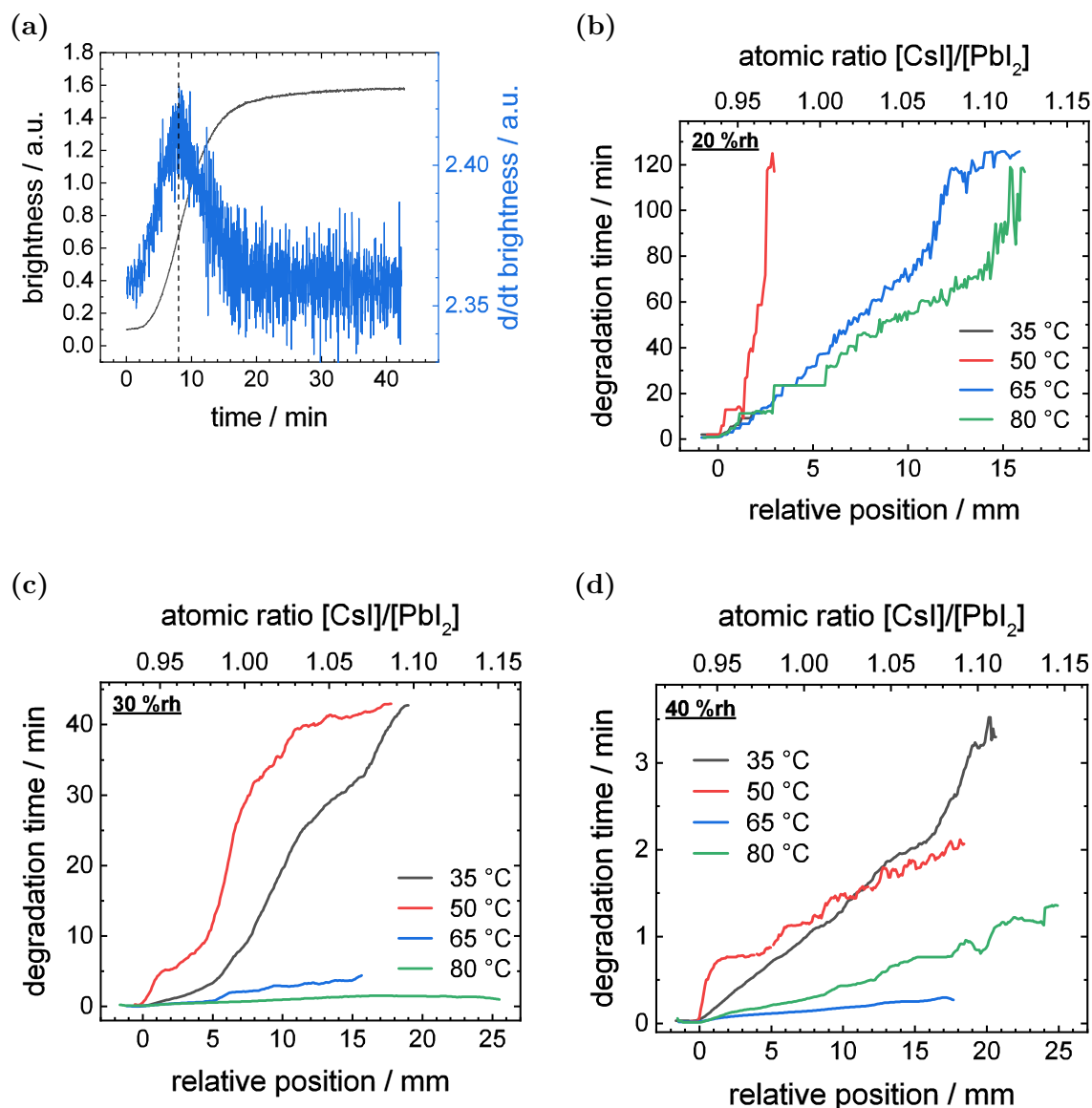
Figure 6-9: *(a) Example for the determination of the degradation time on the $50\,°C$ sample at a relative position of $4.5\,mm$ in $30\,\%rh.$(b),(c),(d) Degradation times over relative position, and therefore composition, for the four samples with different T_{sub} in air with $20\,\%rh$, $30\,\%rh$ and $40\,\%rh$, respectively. For all samples and in all atmospheres the transition begins at the stoichiometric boundary and occurs at the most CsI-rich part last. With few exceptions the degradation occurs faster for samples with higher T_{sub} for a given relative humidity.*

(a)

(b)

(c)

(d)
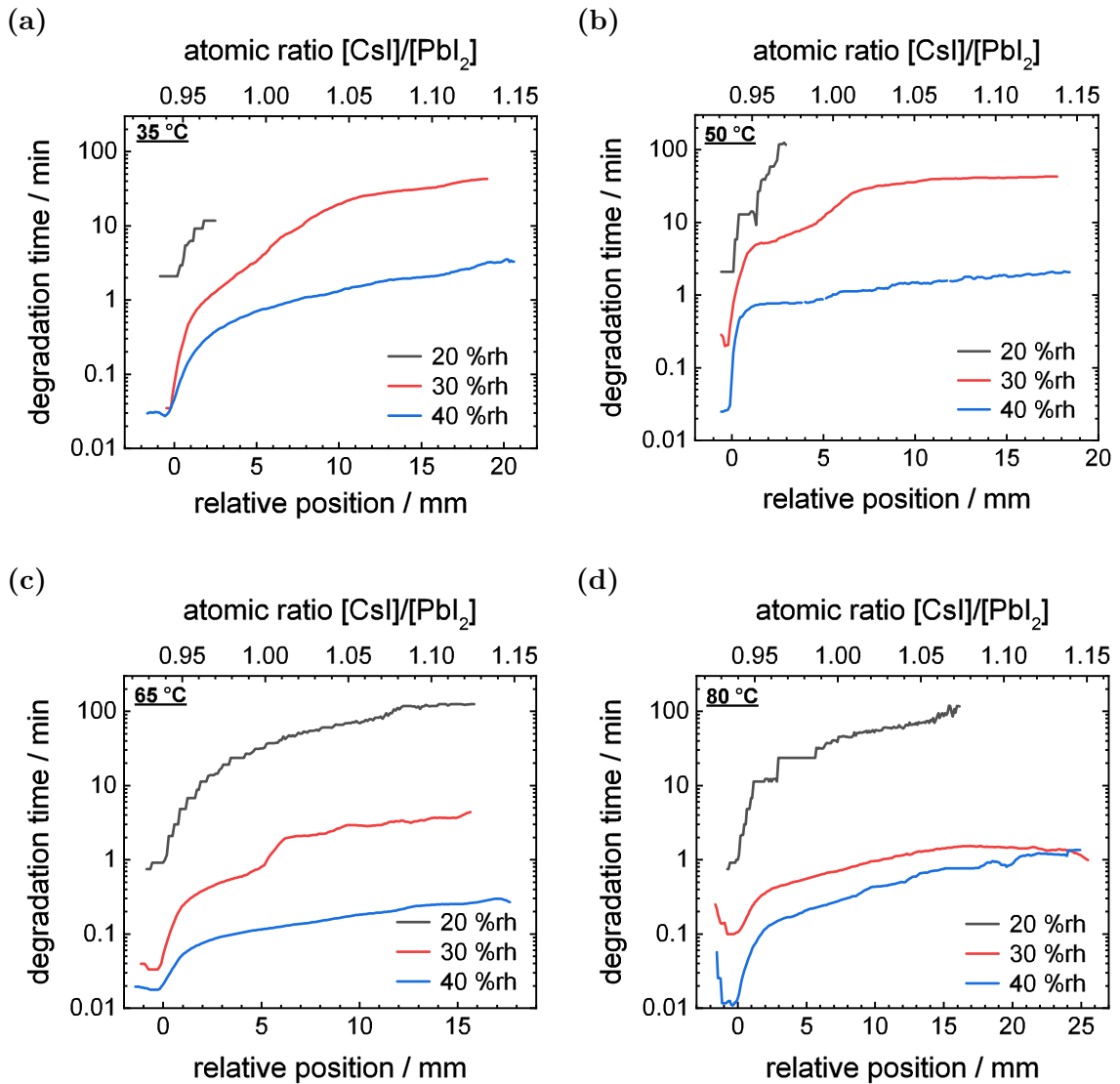
Figure 6-10: *Degradation times over the relative position, and therefore composition, for different relative humidities and for the four samples with T_{sub} of (a) $35\,°C$, (b) $50\,°C$, (c) $65\,°C$ and (d) $80\,°C$. The different offsets at the stoichiometric boundary are suspected to be an artifact of the calculation of the transition times. Within the limited statistics of this experiment, the curves for different relative humidities for a each sample seem to be equidistant on the logarithmic time scale, indicating an exponential dependence of the transition time on the humidity.*

illumination conditions in the laboratory and had to be stopped after ~120 min. Therefore, for the $35\,°C$ and $50\,°C$ samples the degradation times can not be reported over the entire compositional range of the sample, which limits the expressiveness of the correlation between relative humidity and degradation time. Within the statistics of this experiments, however, the curves for the different relative humidities for a given T_{sub} seem to be

equidistant on the logarithmic time scale. This indicates an exponential relation between the degradation time and the relative humidity in the atmosphere.

Comparison of the degradation time for the 50 °C sample determined here with the degradation times from the in-situ XRD-monitoring reveals a slight disagreement. The degradation times of the 30 %rh and 40 %rh processes as determined from the optical reflection differ by about one order of magnitude. In contrast, the degradation times as determined from the XRD-measurements with 35 %rh and 60 %rh only differ by a factor of ~1.2, while being in the same order of magnitude as the degradation time of the measurement at 40 %rh in the optical measurement. The origin of this disagreement might be based on the different environmental temperature during the experiment, thus changing the kinetics of the degradation. As reported in the respective sections, the temperature during the XRD-measurements was around 20 °C, while the optically monitored degradation processes were were conducted at 25 °C.

6.3 Causes and Model of the Degradation Process

Concluding the results from the in-situ XRD and optical reflection measurements it is found, that the degradation is caused by humidity, while oxygen does not lead to degradation in dry atmosphere on the timescales investigated here. The kinetics of the degradation are influenced by the relative humidity in the atmosphere, the chemical composition of the film as well as on T_{sub} during deposition.

When correlating the timings from the XRD results for the phase transition with the timings of the shift of the brown γ-phase diffraction reflexes it shows, that the decrease in intensity of the brown γ-phase starts only after the maximal angular shift of the peaks is reached. This and the different dynamics of the peak shift for different humidities hint towards an interaction of water molecules with the crystal lattice.

As stated above it has been calculated,[71] that the brown γ-phase has a lower surface free energy than the yellow δ-phase, while having a larger bulk free energy. This makes the brown phase stable at room temperature for small crystallites, in which the surface free energy dominates over the bulk free energy.[140, 141] The hypothesis is formed, that water molecules attach to the surface of the $CsPbI_3$ crystallites, thus altering their surface free energy. This change in surface free energy could diminish its domination over the bulk free energy and thus make the brown γ-phase unstable and initiate the phase transition.

This hypothesis could also explain the different degradation times for samples with different T_{sub} and different chemical compositions. Due to the different texturing of the samples as seen in the high resolution XRD measurements, the impact of the molecules

on the surface free energy is likely to be different. In addition, SEM-images and XRD-refinements show, that the grain size decreases slightly with increasing $[CsI]/[PbI_2]$ ratio and decreasing T_{sub} (see Section 3.4 and 3.3), thus increasing the surface-to-volume ratio. Therefore, more drastic changes to the surface free energy are necessary, to overcome its domination over the bulk free energy, thus making it more stable in humid atmosphere. The decrease in texturing with decreasing T_{sub} might also play a role, since the impact of the attaching water on the surface free energy is likely to depend on the orientation of the crystallites.

As seen in the SEM images as well, the surface of the films with excess CsI in the integral chemical composition shows a segregated secondary phase, which is speculated to be CsI. The amount of this secondary phase on the surface increases with increasing integral CsI-content of the film. Since CsI is known to readily incorporate water into its crystal lattice,[114, 132] the segregation on the surface could provide a protection of the underlying $CsPbI_3$ crystallites. This would explain the brown shimmer that remains after the first stage of the degradation and transforms only significantly later. The seemingly linear trend in the degradation time depending on the composition fits to this hypothesis as well. To test this hypothesis, however, more precise measurements and a larger number of processes are required.

6.4 Optical Properties after Degradation

The XRD measurements reveal, that the degradation transforms the former brown γ-phase part into a yellow δ-phase, leaving the sample entirely in the yellow δ-phase. However, the in-situ reflection images in Figure 6-7 show a difference in color even after the degradation is completed after 60 s. Secondary phases cannot be completely excluded by XRD measurements since small grained or amorphous segregations are below the detection limit of this method. To understand the differences in the optical appearance of the two parts, UV-Vis measurements were performed in both areas for each of the four samples. The results are shown in Figure 6-11. Comparison of the reflection measurements in the two parts of the samples show, that the magnitude of the reflection as well as the amplitude and frequency of the interference fringes are very similar to each other. This indicates, that the material in the two parts of the sample has a very similar thickness and surface roughness. The most pronounced differences in the reflections are visible above ~540 nm, which is around the band gap of PbI_2 (see Table 2-1). This hints towards segregation of PbI_2 in the compositionally PbI_2-rich region.

The transition and absorption spectra show a much steeper absorption edge in the degraded, former brown part of the sample than in the former yellow part. The slight

(a)

(b)

(c)

(d)
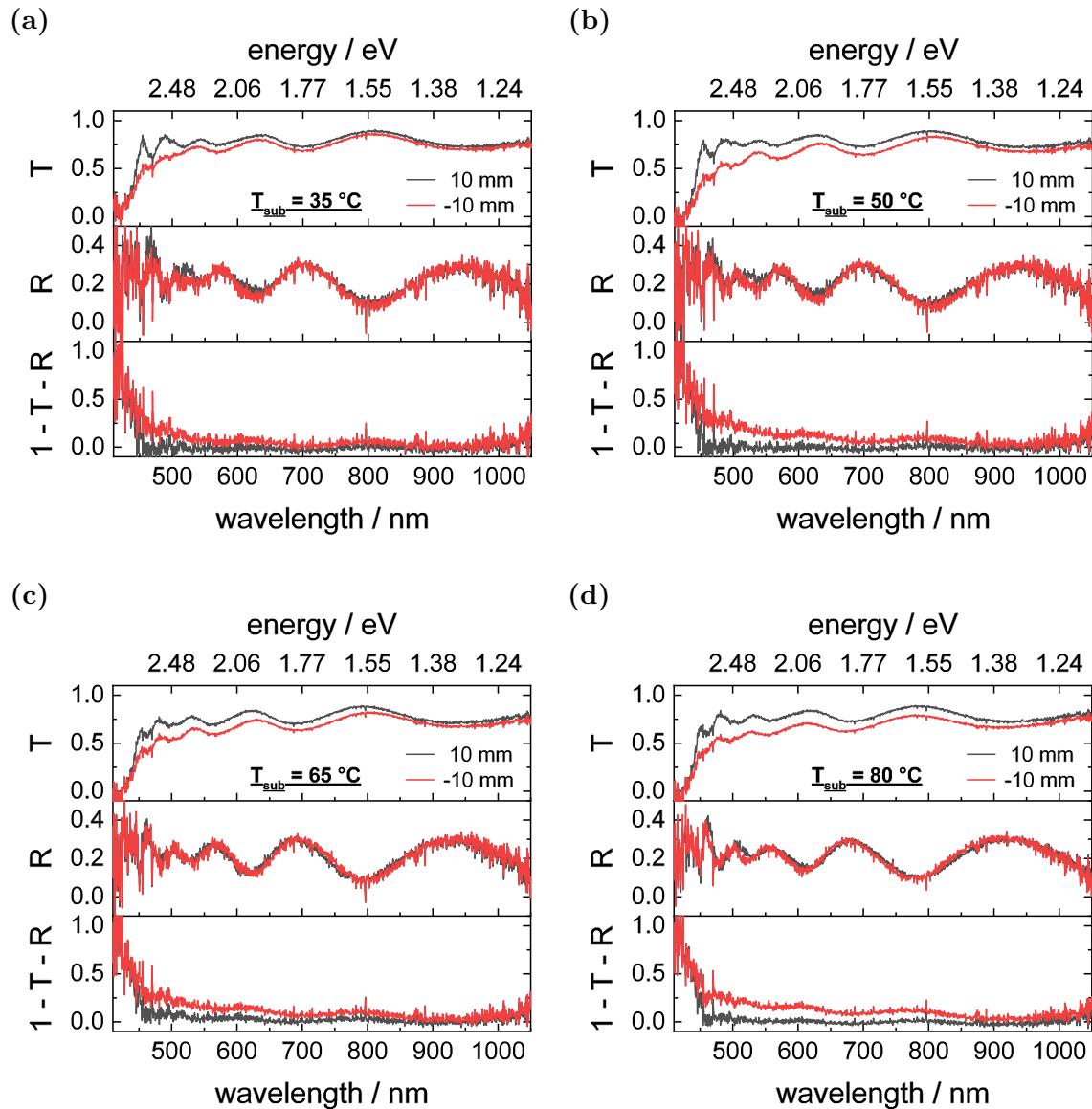
Figure 6-11: *Transmission (T), reflection (R) and absorption (1-T-R) from UV-Vis measurements after the degradation on the samples with different T_{sub}. For each sample one measurement was performed in the former brown part of the sample at a relative position of $10\,\mathrm{mm}$ (black line) and one in the former yellow part at $-10\,\mathrm{mm}$ (red line). The reflection in both parts of the samples is very similar, indicating a similar roughness and thickness of the material. However, the transmission and absorption show a steeper absorption edge in the degraded, formerly brown part as compared to the formerly yellow part.*

differences in the amplitude of the interference fringes close the the absorption edge mostly cancel out with the interference fringes in the reflection, resulting in absorption spectra with no visible fringes above the noise level.

Comparison of the absorption edges of different direct and indirect band gap semiconductors shows, that direct semiconductors show a much steeper absorption edge than indirect semiconductors.[142] This shows, that the electronic structure of the material has a large influence on the shape of the absorption edge. Although in this case the bulk material in both parts of the sample was identified by XRD to be the same δ-phase, the differences in the absorption edge reveal, that the electronic structure is different in the two regions. This differences might stem from the different compositions in the two regions, leading to the formation of specific secondary phases or defects, which alter the band structure in the grains or on the grain boundaries.

For a certain identification of the origin of the different band structures, more measurement, possibly with focus on electronic defects or secondary phases, are required.

7

Conclusions

CsPbI$_3$ thin-film samples were prepared by co-evaporation of CsI and PbI$_2$ at substrate temperatures of T$_{sub}$ = 35 °C, 50 °C, 65 °C and 80 °C with a lateral gradient in the chemical composition of [CsI]/[PbI$_2$]. For the fabrication of these layers, a vacuum setup was developed and installed, which allows precise control of the deposition parameters as well as in-situ process monitoring. The structural and optoelectronic properties of the resulting films as well as the phase transitions, that occur upon annealing at high temperatures and during exposure to ambient atmosphere, were investigated compositional and T$_{sub}$ dependent.

XRF measurements on the as-deposited samples reveal, that the [CsI]/[PbI$_2$] atomic ratio has an almost linear dependency on the lateral position on the sample, independent of T$_{sub}$, thus allowing compositional studies of the properties of the material by spatially resolved measurements. Despite this linear gradient, the as-deposited samples reveal two clearly distinct regions with a sharp boundary between them. By synchrotron based, spatially resolved XRD mapping, these regions were shown to be the brown γ-phase and the yellow δ-phase, respectively. By LeBail-fitting of the patterns from these measurements, it could be demonstrated, that the brown γ-phase is the metastable perovskite phase of CsPbI$_3$ at room temperature. This is in contradiction to literature reports, which claim, that the brown/black phase at room temperature is the cubic α-CsPbI$_3$.[44, 64, 75, 80, 82, 115] However, it is in agreement with most recent literature, which also names the brown γ-phase as the room temperature metastable phase.[69, 113, 133]

Composition dependent SEM images show the segregation of a secondary phase, as soon as the composition becomes off-stoichiometric by excess CsI in the integral composition.

This is in contrast to XRD-measurements, in which no secondary phases could be detected within the precision of the technique for compositions of $[CsI]/[PbI_2]$ between 0.96 and 1.17 ± 0.10. Therefore, the stoichiometry cannot be determined by XRD on the basis of absence of peaks for secondary phases.

By automated grain analysis, which was performed on the SEM images, it was found, that the grain sizes in the brown γ-phase and the yellow δ-phase are very different. While the size of the grains in the γ-phase are in the order of 100 nm, the grain sizes in the yellow phase are in the order of 1 μm. These dimensions are in agreement with the domain sizes, that were extracted from the size-and-strain analysis, which was conducted on the LeBail-refined XRD patterns. T_{sub} showed to have only little impact on the grain size, with only slightly increasing grain sizes for increasing T_{sub}. However, laboratory measurements in Bragg-Brentano-geometry reveal a significant decrease in texturing as T_{sub} increases.

Concluding from these results, a hypothesis for the compositional dependent formation of the two phases was formed. Excess CsI in the composition of the $CsPbI_3$ films can not be incorporated into the film and thus forms a secondary phase. At the same time, any excess CsI hampers the grain growth, resulting in the vastly different grain sizes. Due to a lower surface free energy and a higher bulk free energy of the brown γ-phase as compared to the yellow δ-phase, the γ-phase is thermodynamically favored over the δ-phase for small grains. Thus, the brown γ-phase forms in the small grained CsI-rich part of the sample.

In-situ reflection measurements during the deposition reveal, that in the beginning of the deposition the brown γ-phase also forms in PbI_2-rich areas with larger grain sizes. However, after a certain time the PbI_2-rich part of the sample transitions into the yellow δ-phase. The T_{sub} dependent nature of the transition time reveals, that the transition is a thermally activated process, with an activation energy of $(4.0 \pm 0.2) \cdot 10^4$ J/mol.

The study of the optoelectronic properties of the material reveals a great suitability for application as absorber material in solar cells. The estimated absorption onset of $\sim(1.770 \pm 0.005)$ eV and energy of the PL maximum of $\sim(1.755 \pm 0.010)$ eV in the brown γ-phase part of the sample are slightly higher than the band gap reported in literature of 1.73 eV.[44, 49, 143, 144] No significant dependence of the band gap on the integral composition of the sample nor on T_{sub} could be found. This band gap is in the optimal range for application as a top-cell in a tandem device with a low band gap material bottom-cell such as silicon or kesterite.[64–68]

The charge carrier dynamics reveal a TRPL decay time of $\tau_{SRH} > 60$ ns and an OPTP mobility of $\mu_{THz} > 40$ cm^{2}V^{-1}s^{-1} over the entire investigated compositional range. Combination of both yields an estimated diffusion lengths of above 2 μm, which is four times

larger than the layer thickness of ~500 nm, thus indicating sufficient capabilities for charge extraction. The very weak dependence of the charge carrier dynamics on the integral composition of the material supports the theory, that no CsI can be incorporated into the CsPbI$_3$-lattice, thus leaving the bulk absorber material mostly unchanged upon increasing integral CsI content.

Solely the photoluminescence quantum efficiency showed a significant dependence on the integral composition. While the external PL quantum efficiency close to the stoichiometry was around $5 \cdot 10^{-6}$ the quantum efficiency at $[CsI]/[PbI_2] = 1.07$ was as high as $3 \cdot 10^{-5}$. This reveals a decrease of non-radiative recombination with increasing CsI-content in the chemical composition.

Solar cells, which were fabricated with $[CsI]/[PbI_2] = 1.2 \pm 0.1$ at $T_{sub} = 50\,°C$, exhibit respectable stabilized power conversion efficiencies of up to $11\,\%$ and high current densities of up to $18\,mA/cm^2$. However, they suffer from severe voltage deficits with open-circuit voltages of around $0.9\,V$.

EQE measurements on these cells suggest an energetic barrier at the interfaces between the absorber and the charge extraction layers. These barriers might rise from the CsI-segregation on top of the absorber, as seen in the SEM images. In addition, the in-situ reflection measurements suggest the formation of a $(10 \pm 5)\,nm$ thin yellow δ-phase layer between substrate and actual brown γ-phase absorber layer, which could be confirmed in ex-situ UV-Vis measurements. These barriers are also suggested to be the origin of the strong hysteresis effect, seen in the JV-scan on the cells.

For a more pertinent comparison of the properties of samples reported in this work with samples reported in literature, which are usually obtained after an annealing step at high temperatures, this annealing step was also applied to the as-deposited samples. For this, samples from evaporation with $T_{sub} = 35\,°C$, $50\,°C$, $65\,°C$ and $80\,°C$ were annealed at $320\,°C$ on a hotplate. The optical reflection of the samples was recorded spatially resolved as in-situ monitoring of the phase transitions. By combination of the transition dynamics from these reflection measurements with time and spatially resolved IR-measurements it was found, that the transition temperature from the yellow δ-phase to the black α-phase is $(292 \pm 10)\,°C$ and almost independent of chemical composition and T_{sub}.

XRF measurements of the annealed samples demonstrated, that the composition was altered by the annealing step only within the margin of error of this method. Likewise, the crystal-structure after the annealing step was the same brown γ-phase as in the as-deposited films. However, in contrast to the observed strong texturing especially in the

samples with low T_{sub}, the annealed samples did not reveal a significant texturing, independent of T_{sub}.

This effect of the recrystallization during the annealing process also showed up in the SEM images, which revealed, that the grain sizes in both regions of the samples increased. While grains in the CsI-rich had grown by a factor of ~5 and are in the order of 500 nm, in the PbI_2-rich region of the samples, grain sizes of several µm are visible.

Investigation of the optoelectronic properties showed, that the band gap, as estimated from the absorption coefficient, was (1.775 ± 0.005) eV and therefore unchanged as compared to the as-deposited samples. The maximum of the photoluminescence was slightly lowered to (1.76 ± 0.01) eV, while the quantum yield had significantly increased and was $(2 \pm 1) \cdot 10^{-4}$ over the entire compositional range. Thus, solar cells fabricated with annealed $CsPbI_3$ layers might yield a higher open-circuit voltage as compared to as-deposited absorbers, if limitations by the interfaces can be overcome.

During the conduction of the measurements on the as-deposited sample a sensitivity to ambient atmosphere was realized, which lead to a degradation of the samples. In-situ XRD and optical reflection measurements were performed during the degradation of the samples in different atmospheres to investigate this degradation process.

The XRD measurements revealed, that the degradation is a phase transition from the brown γ-phase to the yellow δ-phase, rather than a change in chemical composition, which is in agreement with previous reports in the literature.[49, 74] It was found, that the transition occurs without any detectable intermediate step. However, the phase transition started only after a short delay, during which a shift in the diffraction angle was observed, where the duration of the delay as well as the magnitude of the shift seemed to be dependent on the relative humidity of the atmosphere. In contrast, the measurements suggested, that the presence of oxygen does not influence the degradation dynamics.

Systematic studies on the influence of humidity and T_{sub} on the degradation dynamics were performed with optical reflection measurements. Thin-films, which were evaporated at substrate temperatures of $T_{sub} = 35\,°C$, $50\,°C$, $65\,°C$ and $80\,°C$ were exposed to oxygen containing atmospheres. After an initial experiment in dry artificial air, which did not lead to degradation over the course of hours, the samples were exposed to atmospheres with relative humidities of $20\,\%$, $30\,\%$ and $40\,\%$. It was found, that the time, after which the degradation occurs, depends on the humidity, the composition and T_{sub}. Higher humidities, less CsI-rich compositions and higher T_{sub} values, respectively, lead to faster degradation.

With the results of these experiments, a model of the degradation process was developed. The correlation of the timings of peak shift and beginning of the phase transition hint towards changes in the crystal lattice before the transition. It is suggested, that these changes are caused by water molecules, that attach to the surface of the crystallites, thus altering the surface free energy and therefore the stress and strain in the crystallites, which can be seen by the peak shift. The altered surface free energy is not dominating over the bulk free energy any more, thus leading to the phase transition. Larger relative humidity values lead to a faster aggregation of water molecules at the surface of the crystallites, thus leading to shorter transition times. The influence of T_{sub} on the transition time might result from a combination of grain size and texturing. Since a lower T_{sub} leads to slightly smaller grains, the dominance of the surface over the bulk free energy is larger for these films, thus requiring a larger change in the surface free energy to initiate the phase transition. In addition, the impact of water aggregation on the surface free energy might depend on the orientation of the crystallites, which could lead to faster degradation time for less textured films. In this model the influence of the composition on the degradation time is based on the slightly lower grain size with increasing CsI content in the integral composition as well as on the suspected segregation of CsI on the surface of the sample. In addition to the aforementioned effect of the grain size, the segregated CsI might act as a protective layer, since CsI is known to readily incorporate H_2O into its crystal lattice. [114, 132] Therefore, the underlying $CsPbI_3$ crystallites might be shielded from the water molecules as long as the CsI segregates efficiently absorb water from the atmosphere.

This work presents an overview about $CsPbI_3$ thin-films from co-evaporation, covering fabrication, crystallographic and optoelectronic properties, high temperature phase transition and degradation of the material. For the first time, these aspects were studied on samples with a continuous gradient in composition. Models for the formation and the degradation of $CsPbI_3$ films were developed with respect to the different room temperature crystal phases of brown γ-$CsPbI_3$ and yellow δ-$CsPbI_3$.

8
Outlook

This work presents a broad overview of the properties of CsPbI$_3$ thin-films. Based on the insights from the evaluation reported in this work, different follow-up experiments are desirable to support and extend the models presented in this work. To utilize the full potential of the evaporation setup, minor updates and the fabrication of different materials are suggested.

For the transfer of the knowledge gained on the compositional film to the fabrication of homogeneous samples, the absolute composition of the samples presented in this work is required. Due to the lack of a standard with precisely known composition, the determination of the composition based on XRF, as reported in this work, comprises a large error of around 10 %. The characterization of a reference sample could for example be performed by the evaluation of the edge-step in X-ray absorption experiments.

Additional measurements are also recommended to confirm the nature of the segregation of a secondary phase, which was seen in SEM images. Based on XRD measurements, which showed a secondary phase of CsI, it was suggested, that this is the phase, that is visible in the SEM images. X-ray photoemission spectroscopy, Raman measurements or energy-dispersive X-ray spectroscopy could contribute valuable data to confirm this suggestion.

In this work, the charge carrier dynamics were investigated depending on the chemical composition, however, only for the $T_{sub} = 50\,°C$ sample. To further investigate the influence of T_{sub} on the charge carrier dynamics, additional measurements on samples with different T_{sub} are required.

These extended investigations are also suggested for the application of the evaporated CsPbI$_3$ films in solar cells. Promising results were achieved without optimization of the

employed cell architecture in a narrow compositional region and $T_{sub} = 50\,°C$. Adjustment of the contact layers as well as utilization of $CsPbI_3$ films with different T_{sub} and compositions closer to the stoichiometry might improve the performance of the cells significantly. The fabrication of more cells would help to improve the statistics for the dependence of the cell performance on the fabrication parameters of the $CsPbI_3$ layers and therefore enhance the understanding of the cell performance.

An improvement of the cell performance could also result from optimization of the surface of the $CsPbI_3$-layer. For this, the suspected CsI segregation could be washed off by solvent dipping.

For continuation of the annealing experiments, a more homogeneous heating source with a larger thermal capacity is highly recommended. This can be achieved for example by placing a thick block of copper or graphite on top of the hotplate, which was used in this work. These modifications would enable the conduction of compositional and T_{sub} dependent nucleation and crystallization studies, since annealing experiments reported in this work showed a vastly different nucleation in the CsI-rich and the PbI_2-rich region, respectively.

Extended annealing experiments could also focus on compositional changes well as improved recrystallization dependent on the annealing time, which could be determined by subsequent XRF and XRD measurements.

With the promising insights into the degradation process, as presented in this work, a confirmation of the suggested model is desirable. This could be supplied by additional measurements during the degradation in different atmospheres. To clarify the origin of the peak shift, measurements with a more rigid sample holder as well as very slow degradation dynamics by low humidity are suggested.
Preliminary measurements of optical transmission microscopy reveal, that the dynamics of the degradation could be resolved on a grain to grain level. Continuation of these efforts are highly suggested for an improved understanding of the degradation mechanism.

The evaporation setup, which was developed for the work presented here, opens unique opportunities for the screening of materials due to its flexibility in deposition of samples with compositional gradients and in-situ investigation capabilities, which are far from being exhausted at this point of development.

The installation of a substrate holder, which enables extended heating and cooling, is suggested. This would allow the fabrication of γ-phase samples with large grain sizes, as seen in the PbI_2-rich part of the sample. Investigation of such samples would improve

the general understanding of structural and optoelectronic properties of the bare $CsPbI_3$ material.

Furthermore, the evaporation setup allows the fabrication of materials with other compositions. This includes the more CsI-rich materials, that revealed excellent stability properties and high photoluminescence, as seen in areas at the edges of the samples presented here, which were affected by unintentional shading of the substrate holder during deposition. Literature suggests, that the partial substitution of iodide by bromide has a stabilizing effect.[46, 145–149] The simultaneous deposition of CsI, PbI_2 and $PbBr_2$ (or CsBr) from three sources would generate samples with a two-dimensional lateral gradient, which would open up a variety of compositional investigations.

On a long-term perspective, the fabrication of tandem-devices is suggested, featuring a low band gap material such as crystalline silicon as bottom cell and the evaporated $CsPbI_3$ thin-films as top cell. The tolerance of the materials optoelectronic properties upon wide variations of the composition, as described in this work, provide a good basis for the large scale industrial fabrication of $CsPbI_3$ thin films. Therefore, inorganic $CsPbI_3$ perovskite presents a promising option for highly performing tandem cells with low production costs.

9

References

[1]   World Energy Outlook 2017, https://www.oecd-ilibrary.org/energy/world-energy-outlook-2017_weo-2017-en.

[2]   K. P. Shine, *Climatic Change* **2009**, *96*, 467–472, DOI `10.1007/s10584-009-9647-6`.

[3]   Fraunhofer ISE, Photovoltaics Report, **2019**.

[4]   K. Kim, J. Kim, M. G. Gang, S.-H. Kim, S. Song, Y. Cho, D. Shin, Y.-J. Eo, I. Jeong, S. K. Ahn, A. Cho, J. Kim, S. Yoon, P.-P. Choi, W. Jo, J. H. Kim, J. Gwak, J. H. Yun, *Solar Energy Materials and Solar Cells* **2019**, *195*, 280–290, DOI `10.1016/j.solmat.2019.03.008`.

[5]   C. L. Perkins, D. L. McGott, M. O. Reese, W. K. Metzger, *ACS Appl. Mater. Interfaces* **2019**, DOI `10.1021/acsami.9b00835`.

[6]   S. L. Patel, Himanshu, S. Chander, M. D. Kannan, M. S. Dhaka, *Physics Letters A* **2019**, DOI `10.1016/j.physleta.2019.03.001`.

[7]   N. Guirdjebaye, S. Ouédraogo, A. Teyou Ngoupo, G. L. Mbopda Tcheum, J. M. B. Ndjaka, *Opto-Electronics Review* **2019**, *27*, 70–78, DOI `10.1016/j.opelre.2019.02.001`.

[8]   B. Schubert, B. Marsen, S. Cinque, T. Unold, R. Klenk, S. Schorr, H.-W. Schock, *Prog. Photovolt. Res. Appl.* **2011**, *19*, 93–96, DOI `10.1002/pip.976`.

[9]   S. van Duren, S. Levcenco, S. Kretzschmar, J. Just, T. Unold, *Journal of Alloys and Compounds* **2019**, *779*, 870–878, DOI `10.1016/j.jallcom.2018.11.337`.

[10]   M. Grätzel, *Journal of Photochemistry and Photobiology C: Photochemistry Reviews* **2003**, *4*, 145–153, DOI `10.1016/S1389-5567(03)00026-1`.

[11] Y. Chiba, A. Islam, Y. Watanabe, R. Komiya, N. Koide, L. Han, *Jpn. J. Appl. Phys.* **2006**, *45*, L638, DOI `10.1143/JJAP.45.L638`.

[12] A. Kojima, K. Teshima, Y. Shirai, T. Miyasaka, *J. Am. Chem. Soc.* **2009**, *131*, 6050–6051, DOI `10.1021/ja809598r`.

[13] G. Rose, *J. Für Prakt. Chem.* **1840**, *19*, 459–468, DOI `10.1002/prac.18400190179`.

[14] V. M. Goldschmidt, *Naturwissenschaften* **1926**, *14*, 477–485, DOI `10.1007/BF01507527`.

[15] G. Ferraris, E. Makovicky, S. Merlino, *Crystallography of Modular Materials*, OUP Oxford, **2004**.

[16] J.-H. Im, C.-R. Lee, J.-W. Lee, S.-W. Park, N.-G. Park, *Nanoscale* **2011**, *3*, 4088–4093, DOI `10.1039/C1NR10867K`.

[17] I. Chung, B. Lee, J. He, R. P. H. Chang, M. G. Kanatzidis, *Nature* **2012**, *485*, 486–489, DOI `10.1038/nature11067`.

[18] H.-S. Kim, C.-R. Lee, J.-H. Im, K.-B. Lee, T. Moehl, A. Marchioro, S.-J. Moon, R. Humphry-Baker, J.-H. Yum, J. E. Moser, M. Grätzel, N.-G. Park, *Sci. Rep.* **2012**, *2*, 591, DOI `10.1038/srep00591`.

[19] NREL, Best Research-Cell Efficiency Chart | Photovoltaic Research, https://www.nrel.gov/pv/cell-efficiency.html, **2019**.

[20] D. Prochowicz, M. Franckevičius, A. M. Cieślak, S. M. Zakeeruddin, M. Grätzel, J. Lewiński, *J. Mater. Chem. A* **2015**, *3*, 20772–20777, DOI `10.1039/C5TA04904K`.

[21] A. M. Elseman, M. M. Rashad, A. M. Hassan, *ACS Sustainable Chem. Eng.* **2016**, *4*, 4875–4886, DOI `10.1021/acssuschemeng.6b01183`.

[22] Q. Chen, H. Zhou, Z. Hong, S. Luo, H.-S. Duan, H.-H. Wang, Y. Liu, G. Li, Y. Yang, *J. Am. Chem. Soc.* **2014**, *136*, 622–625, DOI `10.1021/ja411509g`.

[23] X. Li, D. Bi, C. Yi, J.-D. Décoppet, J. Luo, S. M. Zakeeruddin, A. Hagfeldt, M. Grätzel, *Science* **2016**, *353*, 58–62, DOI `10.1126/science.aaf8060`.

[24] W. S. Yang, J. H. Noh, N. J. Jeon, Y. C. Kim, S. Ryu, J. Seo, S. I. Seok, *Science* **2015**, *348*, 1234–1237, DOI `10.1126/science.aaa9272`.

[25] N. J. Jeon, J. H. Noh, Y. C. Kim, W. S. Yang, S. Ryu, S. I. Seok, *Nat. Mater.* **2014**, *13*, 897–903, DOI `10.1038/nmat4014`.

[26] F. Wang, H. Yu, H. Xu, N. Zhao, *Adv. Funct. Mater.* **2015**, *25*, 1120–1126, DOI `10.1002/adfm.201404007`.

[27] K. Hwang, Y.-S. Jung, Y.-J. Heo, F. H. Scholes, S. E. Watkins, J. Subbiah, D. J. Jones, D.-Y. Kim, D. Vak, *Adv. Mater.* **2015**, *27*, 1241–1247, DOI 10.1002/adma.201404598.

[28] G. Longo, L. Gil-Escrig, M. J. Degen, M. Sessolo, H. J. Bolink, *Chem. Commun.* **2015**, *51*, 7376–7378, DOI 10.1039/C5CC01103E.

[29] D. Zhao, W. Ke, C. R. Grice, A. J. Cimaroli, X. Tan, M. Yang, R. W. Collins, H. Zhang, K. Zhu, Y. Yan, *Nano Energy* **2016**, *19*, 88–97, DOI 10.1016/j.nanoen.2015.11.008.

[30] M. Liu, M. B. Johnston, H. J. Snaith, *Nature* **2013**, *501*, 395–398, DOI 10.1038/nature12509.

[31] P. Fan, D. Gu, G.-X. Liang, J.-T. Luo, J.-L. Chen, Z.-H. Zheng, D.-P. Zhang, *Sci. Rep.* **2016**, *6*, 29910, DOI 10.1038/srep29910.

[32] C.-W. Chen, H.-W. Kang, S.-Y. Hsiao, P.-F. Yang, K.-M. Chiang, H.-W. Lin, *Adv. Mater.* **2014**, *26*, 6647–6652, DOI 10.1002/adma.201402461.

[33] M. Saliba, J.-P. Correa-Baena, C. M. Wolff, M. Stolterfoht, N. Phung, S. Albrecht, D. Neher, A. Abate, *Chem. Mater.* **2018**, *30*, 4193–4201, DOI 10.1021/acs.chemmater.8b00136.

[34] G. Yang, H. Tao, P. Qin, W. Ke, G. Fang, *J. Mater. Chem. A* **2016**, *4*, 3970–3990, DOI 10.1039/C5TA09011C.

[35] D. Bi, L. Yang, G. Boschloo, A. Hagfeldt, E. M. J. Johansson, *J. Phys. Chem. Lett.* **2013**, *4*, 1532–1536, DOI 10.1021/jz400638x.

[36] O. Malinkiewicz, C. Roldán-Carmona, A. Soriano, E. Bandiello, L. Camacho, M. K. Nazeeruddin, H. J. Bolink, *Adv. Energy Mater.* **2014**, *4*, 1400345, DOI 10.1002/aenm.201400345.

[37] W. Ke, G. Fang, J. Wan, H. Tao, Q. Liu, L. Xiong, P. Qin, J. Wang, H. Lei, G. Yang, M. Qin, X. Zhao, Y. Yan, *Nat. Commun.* **2015**, *6*, 6700, DOI 10.1038/ncomms7700.

[38] D. Liu, J. Yang, T. L. Kelly, *J. Am. Chem. Soc.* **2014**, *136*, 17116–17122, DOI 10.1021/ja508758k.

[39] Q. Ma, S. Huang, X. Wen, M. A. Green, A. W. Y. Ho-Baillie, *Adv. Energy Mater.* **2016**, *6*, 1502202, DOI 10.1002/aenm.201502202.

[40] W. S. Yang, B.-W. Park, E. H. Jung, N. J. Jeon, Y. C. Kim, D. U. Lee, S. S. Shin, J. Seo, E. K. Kim, J. H. Noh, S. I. Seok, *Science* **2017**, *356*, 1376–1379, DOI 10.1126/science.aan2301.

[41] T. Ming Koh, T. Krishnamoorthy, N. Yantara, C. Shi, W. Lin Leong, P. P. Boix, A. C. Grimsdale, S. G. Mhaisalkar, N. Mathews, *J. Mater. Chem. A* **2015**, *3*, 14996–15000, DOI `10.1039/C5TA00190K`.

[42] N. De Marco, H. Zhou, Q. Chen, P. Sun, Z. Liu, L. Meng, E.-P. Yao, Y. Liu, A. Schiffer, Y. Yang, *Nano Lett.* **2016**, *16*, 1009–1016, DOI `10.1021/acs.nanolett.5b04060`.

[43] G. Giorgi, J.-I. Fujisawa, H. Segawa, K. Yamashita, *J. Phys. Chem. C* **2015**, *119*, 4694–4701, DOI `10.1021/acs.jpcc.5b00051`.

[44] G. E. Eperon, G. M. Paternò, R. J. Sutton, A. Zampetti, A. A. Haghighirad, F. Cacialli, H. J. Snaith, *J. Mater. Chem. A* **2015**, *3*, 19688–19695, DOI `10.1039/C5TA06398A`.

[45] Z. Chen, J. J. Wang, Y. Ren, C. Yu, K. Shum, *Appl. Phys. Lett.* **2012**, *101*, 093901, DOI `10.1063/1.4748888`.

[46] T. Burwig, W. Fränzel, P. Pistor, *J. Phys. Chem. Lett.* **2018**, *9*, 4808–4813, DOI `10.1021/acs.jpclett.8b02059`.

[47] M. Saliba, T. Matsui, K. Domanski, J.-Y. Seo, A. Ummadisingu, S. M. Zakeeruddin, J.-P. Correa-Baena, W. R. Tress, A. Abate, A. Hagfeldt, M. Grätzel, *Science* **2016**, *354*, 206–209, DOI `10.1126/science.aah5557`.

[48] P. Yadav, M. I. Dar, N. Arora, E. A. Alharbi, F. Giordano, S. M. Zakeeruddin, M. Grätzel, *Adv. Mater.* **2017**, *29*, 1701077, DOI `10.1002/adma.201701077`.

[49] Y. Hu, F. Bai, X. Liu, Q. Ji, X. Miao, T. Qiu, S. Zhang, *ACS Energy Lett.* **2017**, *2*, 2219–2227, DOI `10.1021/acsenergylett.7b00508`.

[50] P. Caprioglio, F. Zu, C. M. Wolff, J. A. M. Prieto, M. Stolterfoht, P. Becker, N. Koch, T. Unold, B. Rech, S. Albrecht, D. Neher, *Sustain. Energy Fuels* **2019**, *3*, 550–563, DOI `10.1039/C8SE00509E`.

[51] E. L. Unger, A. R. Bowring, C. J. Tassone, V. L. Pool, A. Gold-Parker, R. Cheacharoen, K. H. Stone, E. T. Hoke, M. F. Toney, M. D. McGehee, *Chem. Mater.* **2014**, *26*, 7158–7165, DOI `10.1021/cm503828b`.

[52] S. Colella, E. Mosconi, P. Fedeli, A. Listorti, F. Gazza, F. Orlandi, P. Ferro, T. Besagni, A. Rizzo, G. Calestani, G. Gigli, F. De Angelis, R. Mosca, *Chem. Mater.* **2013**, *25*, 4613–4618, DOI `10.1021/cm402919x`.

[53] M. Saliba, T. Matsui, J.-Y. Seo, K. Domanski, J.-P. Correa-Baena, M. Khaja Nazeeruddin, S. M. Zakeeruddin, W. Tress, A. Abate, A. Hagfeldt, M. Grätzel, *Energy Environ. Sci.* **2016**, *9*, 1989–1997, DOI `10.1039/C5EE03874J`.

[54]   M. Stolterfoht, C. M. Wolff, Y. Amir, A. Paulke, L. Perdigón-Toro, P. Caprioglio, D. Neher, *Energy Environ. Sci.* **2017**, *10*, 1530–1539, DOI `10.1039/C7EE00899F`.

[55]   T. Bu, X. Liu, Y. Zhou, J. Yi, X. Huang, L. Luo, J. Xiao, Z. Ku, Y. Peng, F. Huang, Y.-B. Cheng, J. Zhong, *Energy Environ. Sci.* **2017**, *10*, 2509–2515, DOI `10.1039/C7EE02634J`.

[56]   G. Niu, X. Guo, L. Wang, *J. Mater. Chem. A* **2015**, *3*, 8970–8980, DOI `10.1039/C4TA04994B`.

[57]   G. Niu, W. Li, F. Meng, L. Wang, H. Dong, Y. Qiu, *J. Mater. Chem. A* **2013**, *2*, 705–710, DOI `10.1039/C3TA13606J`.

[58]   W. Li, W. Zhang, S. V. Reenen, R. J. Sutton, J. Fan, A. A. Haghighirad, M. B. Johnston, L. Wang, H. J. Snaith, *Energy Environ. Sci.* **2016**, *9*, 490–498, DOI `10.1039/C5EE03522H`.

[59]   B. Conings, J. Drijkoningen, N. Gauquelin, A. Babayigit, J. D'Haen, L. D'Olieslaeger, A. Ethirajan, J. Verbeeck, J. Manca, E. Mosconi, F. D. Angelis, H.-G. Boyen, *Adv. Energy Mater.* **2015**, *5*, 1500477, DOI `10.1002/aenm.201500477`.

[60]   M. H. Kumar, S. Dharani, W. L. Leong, P. P. Boix, R. R. Prabhakar, T. Baikie, C. Shi, H. Ding, R. Ramesh, M. Asta, M. Graetzel, S. G. Mhaisalkar, N. Mathews, *Advanced Materials* **2014**, *26*, 7122–7127, DOI `10.1002/adma.201401991`.

[61]   N. K. Noel, S. D. Stranks, A. Abate, C. Wehrenfennig, S. Guarnera, A.-A. Haghighirad, A. Sadhanala, G. E. Eperon, S. K. Pathak, M. B. Johnston, A. Petrozza, L. M. Herz, H. J. Snaith, *Energy Environ. Sci.* **2014**, *7*, 3061–3068, DOI `10.1039/C4EE01076K`.

[62]   H. L. Wells, *Am. J. Sci.* **1893**, *s3-45*, 121–134, DOI `10.2475/ajs.s3-45.266.121`.

[63]   C. K. Møller, *Nature* **1958**, *182*, 1436, DOI `10.1038/1821436a0`.

[64]   W. Ahmad, J. Khan, G. Niu, J. Tang, *Sol. RRL* **2017**, *1*, 1700048, DOI `10.1002/solr.201700048`.

[65]   K. Hamada, K. Yonezawa, K. Yamamoto, T. Taima, S. Hayase, N. Ooyagi, Y. Yamamoto, K. Ohdaira, *Jpn. J. Appl. Phys.* **2019**, *58*, SBBF06, DOI `10.7567/1347-4065/aafb56`.

[66]   R. J. Stoddard, A. Rajagopal, R. L. Palmer, I. L. Braly, A. K.-Y. Jen, H. W. Hillhouse, *ACS Energy Lett.* **2018**, *3*, 1261–1268, DOI `10.1021/acsenergylett.8b00576`.

[67]   Z. Yu, M. Leilaeioun, Z. Holman, *Nat. Energy* **2016**, *1*, 16137, DOI `10.1038/nenergy.2016.137`.

[68] Y. Li, H. Hu, B. Chen, T. Salim, Y. M. Lam, N. Yuan, J. Ding, *Solar Energy* **2017**, *155*, 35–38, DOI 10.1016/j.solener.2017.06.026.

[69] A. Marronnier, G. Roma, S. Boyer-Richard, L. Pedesseau, J.-M. Jancu, Y. Bonnassieux, C. Katan, C. C. Stoumpos, M. G. Kanatzidis, J. Even, *ACS Nano* **2018**, *12*, 3477–3486, DOI 10.1021/acsnano.8b00267.

[70] C. C. Stoumpos, M. G. Kanatzidis, *Acc. Chem. Res.* **2015**, *48*, 2791–2802, DOI 10.1021/acs.accounts.5b00229.

[71] B. Zhao, S.-F. Jin, S. Huang, N. Liu, J.-Y. Ma, D.-J. Xue, Q. Han, J. Ding, Q.-Q. Ge, Y. Feng, J.-S. Hu, *J. Am. Chem. Soc.* **2018**, *140*, 11716–11725, DOI 10.1021/jacs.8b06050.

[72] Y. Fu, M. T. Rea, J. Chen, D. J. Morrow, M. P. Hautzinger, Y. Zhao, D. Pan, L. H. Manger, J. C. Wright, R. H. Goldsmith, S. Jin, *Chem. Mater.* **2017**, *29*, 8385–8394, DOI 10.1021/acs.chemmater.7b02948.

[73] Y. Wang, T. Zhang, M. Kan, Y. Li, T. Wang, Y. Zhao, *Joule* **2018**, *2*, 2065–2075, DOI 10.1016/j.joule.2018.06.013.

[74] T. Zhang, M. I. Dar, G. Li, F. Xu, N. Guo, M. Grätzel, Y. Zhao, *Sci. Adv.* **2017**, *3*, e1700841, DOI 10.1126/sciadv.1700841.

[75] R. J. Sutton, G. E. Eperon, L. Miranda, E. S. Parrott, B. A. Kamino, J. B. Patel, M. T. Hörantner, M. B. Johnston, A. A. Haghighirad, D. T. Moore, H. J. Snaith, *Adv. Energy Mater.* **2016**, *6*, 1502458, DOI 10.1002/aenm.201502458.

[76] R. E. Beal, D. J. Slotcavage, T. Leijtens, A. R. Bowring, R. A. Belisle, W. H. Nguyen, G. F. Burkhard, E. T. Hoke, M. D. McGehee, *J. Phys. Chem. Lett.* **2016**, *7*, 746–751, DOI 10.1021/acs.jpclett.6b00002.

[77] L. Protesescu, S. Yakunin, M. I. Bodnarchuk, F. Krieg, R. Caputo, C. H. Hendon, R. X. Yang, A. Walsh, M. V. Kovalenko, *Nano Lett.* **2015**, *15*, 3692–3696, DOI 10.1021/nl5048779.

[78] Y. Wang, T. Zhang, M. Kan, Y. Zhao, *J. Am. Chem. Soc.* **2018**, *140*, 12345–12348, DOI 10.1021/jacs.8b07927.

[79] A. Shpatz Dayan, B.-E. Cohen, S. Aharon, C. Tenailleau, M. Wierzbowska, L. Etgar, *Chem. Mater.* **2018**, *30*, 8017–8024, DOI 10.1021/acs.chemmater.8b03709.

[80] P. Luo, W. Xia, S. Zhou, L. Sun, J. Cheng, C. Xu, Y. Lu, *J. Phys. Chem. Lett.* **2016**, *7*, 3603–3608, DOI 10.1021/acs.jpclett.6b01576.

[81] M. Lai, Q. Kong, C. G. Bischak, Y. Yu, L. Dou, S. W. Eaton, N. S. Ginsberg, P. Yang, *Nano Res.* **2017**, *10*, 1107–1114, DOI 10.1007/s12274-016-1415-0.

[82] S. Dastidar, C. J. Hawley, A. D. Dillon, A. D. Gutierrez-Perez, J. E. Spanier, A. T. Fafarman, *J. Phys. Chem. Lett.* **2017**, *8*, 1278–1282, DOI 10.1021/acs.jpclett.7b00134.

[83] L. A. Frolova, D. V. Anokhin, A. A. Piryazev, S. Y. Luchkin, N. N. Dremova, K. J. Stevenson, P. A. Troshin, *J. Phys. Chem. Lett.* **2017**, *8*, 67–72, DOI 10.1021/acs.jpclett.6b02594.

[84] C. Qin, T. Matsushima, A. S. D. Sandanayaka, Y. Tsuchiya, C. Adachi, *J. Phys. Chem. Lett.* **2017**, *8*, 5415–5421, DOI 10.1021/acs.jpclett.7b02371.

[85] C. K. Møller, Kongelige Danske videnskabernes selskab, *On the Structure of Cæsium Hexahalogeno-Plumbates (II)*, OCLC: 9198591, Munksgaard, København, **1960**.

[86] T.-L. Huang, A. L. Ruoff, *Phys. Rev. B* **1984**, *29*, 1112–1114, DOI 10.1103/PhysRevB.29.1112.

[87] W. M. Sears, M. L. Klein, J. A. Morrison, *Phys. Rev. B* **1979**, *19*, 2305–2313, DOI 10.1103/PhysRevB.19.2305.

[88] M. Chand, G. C. Trigunayat, *Acta Cryst B* **1975**, *31*, 1222–1223, DOI 10.1107/S0567740875004918.

[89] M. Chand, G. C. Trigunayat, *Journal of Crystal Growth* **1976**, *35*, 307–310, DOI 10.1016/0022-0248(76)90189-5.

[90] R. Kottokkaran, H. A. Gaonkar, B. Bagheri, V. L. Dalal, *Journal of Vacuum Science & Technology A* **2018**, *36*, 041201, DOI 10.1116/1.5029253.

[91] Q. A. Akkerman, S. Park, E. Radicchi, F. Nunzi, E. Mosconi, F. De Angelis, R. Brescia, P. Rastogi, M. Prato, L. Manna, *Nano Lett.* **2017**, *17*, 1924–1930, DOI 10.1021/acs.nanolett.6b05262.

[92] Triloki, R. Rai, B. K. Singh, *Nuclear Instruments and Methods in Physics Research Section A: Accelerators Spectrometers Detectors and Associated Equipment* **2015**, *785*, 70–76, DOI 10.1016/j.nima.2015.02.059.

[93] V. Mehrotra, S. Lombardo, M. O. Thompson, E. P. Giannelis, *Phys. Rev. B* **1991**, *44*, 5786–5790, DOI 10.1103/PhysRevB.44.5786.

[94] K. Miandal, K. A. Mohamad, A. Alias, *J. Adv. Res. Mater. Sci.* **2016**, *26*, 7–12.

[95] X. Chen, Z. Wang, *Micron* **2019**, *116*, 73–79, DOI 10.1016/j.micron.2018.09.010.

[96] W. L. Bragg, *Proc. Camb. Philos. Soc.* **1913**, *1*, 43–57.

[97]   M. Wansleben, C. Zech, C. Streeck, J. Weser, C. Genzel, B. Beckhoff, R. Mainz, *J. Anal. At. Spectrom.* **2019**, *34*, 1497–1502, DOI `10.1039/C9JA00127A`.

[98]   B. B. He, *Two-Dimensional X-Ray Diffraction*, John Wiley & Sons, **2011**.

[99]   B. B. He, U. Preckwinkel, K. L. Smith, *Adv. X-Ray Anal.* **2003**, *46*, 37–42.

[100]   W. Kraus, G. Nolze, *J Appl Cryst* **1996**, *29*, 301–303, DOI `10 . 1107 / S0021889895014920`.

[101]   A. Le Bail, H. Duroy, J. L. Fourquet, *Materials Research Bulletin* **1988**, *23*, 447– 452, DOI `10.1016/0025-5408(88)90019-0`.

[102]   H.-H. Perkampus, *UV-VIS Spectroscopy and Its Applications*, Springer Science & Business Media, **2013**.

[103]   W. Lu, Y. Fu in *Spectroscopy of Semiconductors: Numerical Analysis Bridging Quantum Mechanics and Experiments*, (Eds.: W. Lu, Y. Fu), Springer Series in Optical Sciences, Springer International Publishing, Cham, **2018**, pp. 23–71, DOI `10.1007/978-3-319-94953-6_2`.

[104]   T. Unold, L. Gütay in *Advanced Characterization Techniques for Thin Film Solar Cells*, John Wiley & Sons, Ltd, **2011**, pp. 151–175, DOI `10.1002/9783527636280.ch7`.

[105]   H. Hempel, T. Unold, R. Eichberger, *Opt. Express OE* **2017**, *25*, 17227–17236, DOI `10.1364/OE.25.017227`.

[106]   H. Hempel, C. J. Hages, R. Eichberger, I. Repins, T. Unold, *Sci. Rep.* **2018**, *8*, 14476, DOI `10.1038/s41598-018-32695-6`.

[107]   P. Becker, J. A. Márquez, J. Just, A. Al-Ashouri, C. Hages, H. Hempel, M. Jošt, S. Albrecht, R. Frahm, T. Unold, *Adv. Energy Mater.* **2019**, *0*, 1900555, DOI `10.1002/aenm.201900555`.

[108]   M. D. Heinemann, R. Mainz, F. Österle, H. Rodriguez-Alvarez, D. Greiner, C. A. Kaufmann, T. Unold, *Sci. Rep.* **2017**, *7*, 45463, DOI `10.1038/srep45463`.

[109]   A. Guerrero, E. J. Juarez-Perez, J. Bisquert, I. Mora-Sero, G. Garcia-Belmonte, *Appl. Phys. Lett.* **2014**, *105*, 133902, DOI `10.1063/1.4896779`.

[110]   A. Dutta, R. K. Behera, N. Pradhan, *ACS Energy Lett.* **2019**, 926–932, DOI `10.1021/acsenergylett.9b00443`.

[111]   Y. Chen, H. Jing, F. Ling, W. Kang, T. Zhou, X. Liu, W. Zeng, Y. Zhang, L. Qi, L. Fang, M. Zhou, *Chemical Physics Letters* **2019**, *722*, 90–95, DOI `10.1016/j.cplett.2019.02.050`.

[112] B. Jeong, H. Han, Y. J. Choi, S. H. Cho, E. H. Kim, S. W. Lee, J. S. Kim, C. Park, D. Kim, C. Park, *Adv. Funct. Mater.* **2018**, *28*, 1706401, DOI `10.1002/adfm.201706401`.

[113] F. Bertolotti, L. Protesescu, M. V. Kovalenko, S. Yakunin, A. Cervellino, S. J. L. Billinge, M. W. Terban, J. S. Pedersen, N. Masciocchi, A. Guagliardi, *ACS Nano* **2017**, *11*, 3819–3831, DOI `10.1021/acsnano.7b00017`.

[114] N. Jammal, R. Rai, Triloki, B. K. Singh, *Physica B: Condensed Matter* **2018**, *546*, 21–27, DOI `10.1016/j.physb.2018.07.017`.

[115] A. K. Jena, A. Kulkarni, Y. Sanehira, M. Ikegami, T. Miyasaka, *Chem. Mater.* **2018**, *30*, 6668–6674, DOI `10.1021/acs.chemmater.8b01808`.

[116] E. M. Hutter, R. J. Sutton, S. Chandrashekar, M. Abdi-Jalebi, S. D. Stranks, H. J. Snaith, T. J. Savenije, *ACS Energy Lett.* **2017**, *2*, 1901–1908, DOI `10.1021/acsenergylett.7b00591`.

[117] B. Warren, *X-Ray Diffraction*, Addison-Wesley Publishing Co., **1969**.

[118] Y. Li, Y. Zhang, Z. Zhao, L. Zhi, X. Cao, Y. Jia, F. Lin, L. Zhang, X. Cui, J. Wei, *Crystal Growth & Design* **2018**, *18*, 3458–3464, DOI `10.1021/acs.cgd.8b00181`.

[119] Y. Dang, Y. Liu, Y. Sun, D. Yuan, X. Liu, W. Lu, G. Liu, H. Xia, X. Tao, *CrystEngComm* **2015**, *17*, 665–670, DOI `10.1039/C4CE02106A`.

[120] G. E. Eperon, C. E. Beck, H. J. Snaith, *Mater. Horiz.* **2016**, *3*, 63–71, DOI `10.1039/C5MH00170F`.

[121] C. J. Hages, A. Redinger, S. Levcenko, H. Hempel, M. J. Koeper, R. Agrawal, D. Greiner, C. A. Kaufmann, T. Unold, *Adv. Energy Mater.* **2017**, *7*, 1700167, DOI `10.1002/aenm.201700167`.

[122] P. Wang, X. Zhang, Y. Zhou, Q. Jiang, Q. Ye, Z. Chu, X. Li, X. Yang, Z. Yin, J. You, *Nat. Commun.* **2018**, *9*, 2225, DOI `10.1038/s41467-018-04636-4`.

[123] M. Afsari, A. Boochani, M. Hantezadeh, *Optik* **2016**, *127*, 11433–11443, DOI `10.1016/j.ijleo.2016.09.013`.

[124] Y. Jiang, J. Yuan, Y. Ni, J. Yang, Y. Wang, T. Jiu, M. Yuan, J. Chen, *Joule* **2018**, *2*, 1356–1368, DOI `10.1016/j.joule.2018.05.004`.

[125] E. M. Sanehira, A. R. Marshall, J. A. Christians, S. P. Harvey, P. N. Ciesielski, L. M. Wheeler, P. Schulz, L. Y. Lin, M. C. Beard, J. M. Luther, *Sci. Adv.* **2017**, *3*, eaao4204, DOI `10.1126/sciadv.aao4204`.

[126] W. Shockley, H. J. Queisser, *Journal of Applied Physics* **1961**, *32*, 510–519, DOI `10.1063/1.1736034`.

[127] S. Rühle, *Solar Energy* **2016**, *130*, 139–147, DOI `10.1016/j.solener.2016.02.015`.

[128] D. A. Jacobs, Y. Wu, H. Shen, C. Barugkin, F. J. Beck, T. P. White, K. Weber, K. R. Catchpole, *Phys. Chem. Chem. Phys.* **2017**, *19*, 3094–3103, DOI `10.1039/C6CP06989D`.

[129] S. Ravishankar, S. Gharibzadeh, C. Roldán-Carmona, G. Grancini, Y. Lee, M. Ralaiarisoa, A. M. Asiri, N. Koch, J. Bisquert, M. K. Nazeeruddin, *Joule* **2018**, *2*, 788–798, DOI `10.1016/j.joule.2018.02.013`.

[130] S. A. Weber, I. M. Hermes, S.-H. Turren-Cruz, C. Gort, V. W. Bergmann, L. Gilson, A. Hagfeldt, M. Graetzel, W. Tress, R. Berger, *Energy Environ. Sci.* **2018**, *11*, 2404–2413, DOI `10.1039/C8EE01447G`.

[131] I. M. Hermes, Y. Hou, V. W. Bergmann, C. J. Brabec, S. A. L. Weber, *J. Phys. Chem. Lett.* **2018**, *9*, 6249–6256, DOI `10.1021/acs.jpclett.8b02824`.

[132] C.-Y. Chen, H.-Y. Lin, K.-M. Chiang, W.-L. Tsai, Y.-C. Huang, C.-S. Tsao, H.-W. Lin, *Adv. Mater.* **2017**, *29*, 1605290, DOI `10.1002/adma.201605290`.

[133] R. J. Sutton, M. R. Filip, A. A. Haghighirad, N. Sakai, B. Wenger, F. Giustino, H. J. Snaith, *ACS Energy Lett.* **2018**, *3*, 1787–1794, DOI `10.1021/acsenergylett.8b00672`.

[134] K. Wang, Z. Jin, L. Liang, H. Bian, H. Wang, J. Feng, Q. Wang, S. (Liu, *Nano Energy* **2019**, *58*, 175–182, DOI `10.1016/j.nanoen.2019.01.034`.

[135] F. Staub, T. Kirchartz, K. Bittkau, U. Rau, *J. Phys. Chem. Lett.* **2017**, *8*, 5084–5090, DOI `10.1021/acs.jpclett.7b02224`.

[136] N. Aristidou, I. Sanchez-Molina, T. Chotchuangchutchaval, M. Brown, L. Martinez, T. Rath, S. A. Haque, *Angew. Chem. Int. Ed.* **2015**, *54*, 8208–8212, DOI `10.1002/anie.201503153`.

[137] J. Yang, B. D. Siempelkamp, D. Liu, T. L. Kelly, *ACS Nano* **2015**, *9*, 1955–1963, DOI `10.1021/nn506864k`.

[138] J.-F. Liao, H.-S. Rao, B.-X. Chen, D.-B. Kuang, C.-Y. Su, *J. Mater. Chem. A* **2017**, *5*, 2066–2072, DOI `10.1039/C6TA09582H`.

[139] C. C. Stoumpos, C. D. Malliakas, M. G. Kanatzidis, *Inorg. Chem.* **2013**, *52*, 9019–9038, DOI `10.1021/ic401215x`.

[140] J. M. McHale, A. Auroux, A. J. Perrotta, A. Navrotsky, *Science* **1997**, *277*, 788–791, DOI `10.1126/science.277.5327.788`.

[141]   F. Wang, Y. Han, C. S. Lim, Y. Lu, J. Wang, J. Xu, H. Chen, C. Zhang, M. Hong, X. Liu, *Nature* **2010**, *463*, 1061–1065, DOI `10.1038/nature08777`.

[142]   G. E. Stillman, V. M. Robbins, N. Tabatabaie, *IEEE Trans. Electron Devices* **1984**, *31*, 1643–1655, DOI `10.1109/T-ED.1984.21765`.

[143]   Y. G. Kim, T.-Y. Kim, J. H. Oh, K. S. Choi, Y.-J. Kim, S. Y. Kim, *Phys. Chem. Chem. Phys.* **2017**, *19*, 6257–6263, DOI `10.1039/C6CP08177K`.

[144]   M. R. Filip, G. E. Eperon, H. J. Snaith, F. Giustino, *Nat. Commun.* **2014**, *5*, 5757, DOI `10.1038/ncomms6757`.

[145]   Q. A. Akkerman, V. D'Innocenzo, S. Accornero, A. Scarpellini, A. Petrozza, M. Prato, L. Manna, *J. Am. Chem. Soc.* **2015**, *137*, 10276–10281, DOI `10.1021/jacs.5b05602`.

[146]   Z. Guo, S. Teo, Z. Xu, C. Zhang, Y. Kamata, S. Hayase, T. Ma, *J. Mater. Chem. A* **2019**, *7*, 1227–1232, DOI `10.1039/C8TA09838G`.

[147]   C. F. J. Lau, X. Deng, Q. Ma, J. Zheng, J. S. Yun, M. A. Green, S. Huang, A. W. Y. Ho-Baillie, *ACS Energy Lett.* **2016**, *1*, 573–577, DOI `10.1021/acsenergylett.6b00341`.

[148]   H. Bian, D. Bai, Z. Jin, K. Wang, L. Liang, H. Wang, J. Zhang, Q. Wang, S. (Liu, *Joule* **2018**, *2*, 1500–1510, DOI `10.1016/j.joule.2018.04.012`.

[149]   B. Yang, M. Wang, X. Hu, T. Zhou, Z. Zang, *Nano Energy* **2019**, *57*, 718–727, DOI `10.1016/j.nanoen.2018.12.097`.

A

Appendix

Drift in the spectrometer

During the measurements with the UV-Vis setup described in Section 2.2, a drift of the intensity of the spectra over time was observed. To demonstrate this drift, the spectrum of the lamp was recorded in transmission geometry without any sample in place. The lamp was pre-heated for 2 h, but not connected to the setup. Subsequently, a continuous measurement with integration time of 2 s was started and the lamp was connected. Averaged single spectra from this scan are depicted in Figure A-1. The entire spectra drift towards lower counts, even in the wavelength range below 400 nm, where no intensity from the halogen lamp is expected. This reveals, that the observed drift is most likely not caused by the light source, but by the spectrometer itself. The drift could be observed when using the software of the manufacturer, as well as the custom made software for the UV-Vis setup, thus excluding a software error. However, it could not be concluded, if the error is caused by a hardware effect, such as heating of the grid by the illumination, or by a read-out error of the memory, which is built into the spectrometer.

To investigate the drift further, the counts at specific wavelengths were extracted from all spectra of the continuous acquisition. The wavelengths, which were used for this tracking are displayed in Figure A-1 with vertical lines. The temporal evolution of the extracted values are shown in Figure A-2. For all extracted wavelengths, the drift shows an exponential decay in the beginning. After ~80 min, however, a slight increase can be seen. This demonstrates, that even a "pre-heating" of the spectrometer will not completely eradicate this error.
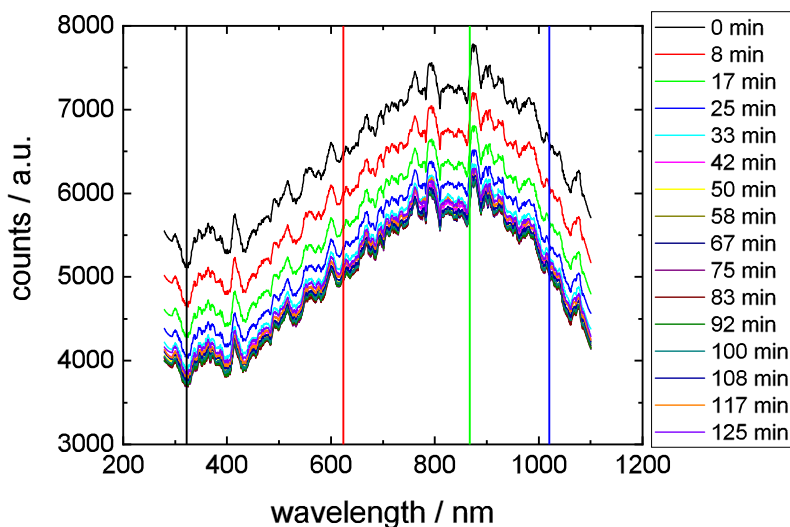
Figure A-1: *Averaged single spectra extracted from a continuous scan with* $2\,\text{s}$ *integration time. The spectra were recorded in transmission geometry without any sample in place. A decelerating drift towards lower counts can be seen.*

To overcome this error and allow measurements with the setup, a correction mechanism was found. Comparison of the individual spectra from the continuous scan revealed, that the drift does not solely consist of a additive shift to lower energy but also a slight multiplicative scaling of the spectra. However, subtractive correction of the spectra reduce
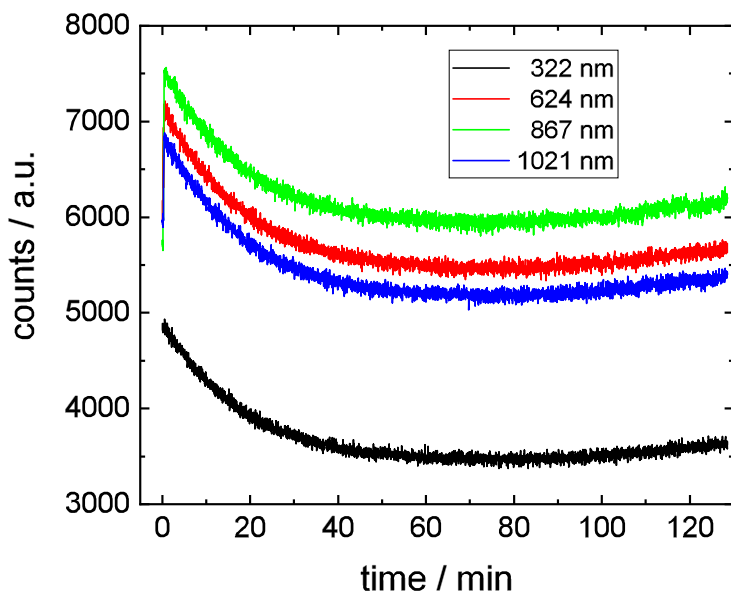
Figure A-2: *Counts extracted for specific wavelengths, as extracted from a continuous scan, over time. The counts show an exponential decay in the beginning. However, after ~$80\,\text{min}$ the intensity starts to slightly increase again.*

the magnitude of the error significantly. For this, the counts between 280 nm and 340 nm were averaged to improve the signal-to-noise ratio for the correction. This range of wavelengths was chosen, since no intensity of the lamp is expected in this range, making it a suitable measure for both, low and high intensity measurements. The difference between these averaged values was defined as the shift of spectra. All spectra, including the reference measurements, were corrected by subtraction of this shift in respect to one reference spectrum (e.g. the first spectrum of the measurement).

To demonstrate this correction, the spectra shown in Figure A-1 were corrected as described above. The resulting corrected spectra are shown in Figure A-3. While the subtractive correction removes the majority of the error, which is caused by the drift, it does not completely eliminate it. Especially the spectra, which were recorded in the first minutes after the start of the experiment, still show deviations from the spectra, which were recorded later.

To minimize the influence of the drift during the measurement, which are reported in this work, the spectrometer was "pre-heated" for >1 h before the measurement. The acquired spectra were corrected with the subtractive shift, as described above, before they were used for further calculations. While increased uncertainties remain for the measurements performed with this setup, these measures result in transmission and reflection measurements with suitable quality for the evaluations performed in this work.
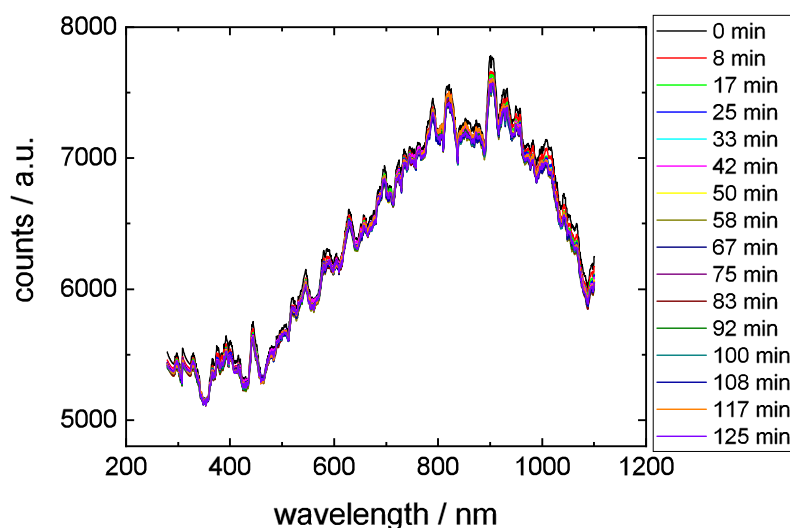
Figure A-3: Averaged single spectra extracted from a continuous scan after applying a subtractive correction to the spectra depicted in Figure A-1. The error is not completely eliminated, but significantly reduced in magnitude.

B

Appendix

List of XRD-reflexes for quantification of the phase transition

Table B-3: List of hkl-indices of the peaks, that were used to model the lateral transition from brown γ-phase to yellow δ-phase as well as the phase segregation.

brown γ-CsPbI$_3$	yellow δ-CsPbI$_3$	PbI$_2$	CsI
112	002	030	110
200	102		
120	200		
210	103		
121	204		
211	105		
002	212		
110	302		

Acknowledgements

I would like to thank Prof. Ronald Frahm for giving me the opportunity to work in his group at the University of Wuppertal and for his support throughout this project.

I would also like to thank Thomas Unold for his supervision within the past five years. The work in his group at the Helmholtz-Zentrum Berlin expanded my scientific horizon.

Special thanks to Prof. Dirk Lützenkirchen-Hecht, who was like a "physics-father" to me from my first scientific steps on. I am very grateful for the countless discussions, his guidance and humorous hours during beam times.

I am especially thankful for the support of Justus Just, without whom the design and construction of the evaporation chamber would have been impossible. His revolutionary ideas and ambitious precision paved the way for the results presented in this work.

My deepest thanks to Pepe Márquez for being a virtually infinite source of motivation. His capacity of enthusiasm and support in all aspects of the thesis have a great share on the finalization of this work.

Many thanks to all the members and former members of the groups at the Helmholtz-Zentrum Berlin and at the University of Wuppertal, who answered myriads of questions and with whom a had many cheerful hours.

I would also like to thank my friends and family, who supported me no matter what. Their backing was the foundation for this work.

Finally, I would like to thank Sabrina Beblo, who had to endure physics jabbering and worse exertions over the past months and encouraged me to keep going, nonetheless. I am very grateful for your unconditional support.

Many thanks to everyone, who supported me scientifically or elsewhere.

Declaration of Authorship

I hereby confirm that this thesis with the title "Structural and Optoelectronic Properties, Phase Transitions, and Degradation of Semiconducting $CsPbI_3$-Perovskite Thin-Films for Photovoltaics" and the work presented in it are my own and the result of my own original research. All sources and resources of other authors are marked as such and listed in the bibliography.

_____

Pascal Becker